RICE UNIVERSITY

Modulation of the Osteoblastic Differentiation of Marrow Stromal Cells for Bone Tissue Engineering

by

Quynh P. Pham

A THESIS SUBMITTED
IN PARTIAL FULFILLMENT OF THE
REQUIREMENTS FOR THE DEGREE
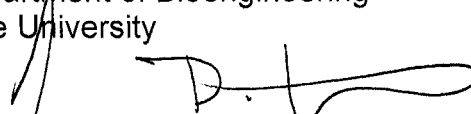
Doctor of Philosophy
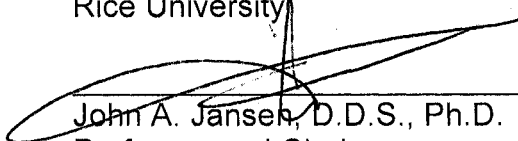
APPROVED, THESIS COMMITTEE:

Antonios G. Mikos, Ph.D. (Committee Chair)
John W. Cox Professor
Departments of Bioengineering and Chemical
and Biomolecular Engineering
Rice University

K. Jane Grande-Allen, Ph.D.
Assistant Professor
Department of Bioengineering
Rice University

Jeffrey D. Hartgerink, Ph.D.
Assistant Professor
Department of Chemistry
Rice University

John A. Jansen, D.D.S., Ph.D.
Professor and Chairman
Department of Periodontology and Biomaterials,
University Medical Center
Nijmegen, The Netherlands

HOUSTON, TEXAS
DECEMBER 2007

UMI Number: 3309943

INFORMATION TO USERS

The quality of this reproduction is dependent upon the quality of the copy submitted. Broken or indistinct print, colored or poor quality illustrations and photographs, print bleed-through, substandard margins, and improper alignment can adversely affect reproduction.

In the unlikely event that the author did not send a complete manuscript and there are missing pages, these will be noted. Also, if unauthorized copyright material had to be removed, a note will indicate the deletion.

Abstract

Modulation of the Osteoblastic Differentiation
of Marrow Stromal Cells

by

Quynh P. Pham

The clinical need for bone graft substitutes has led tissue engineering strategies to investigate strategies to create osteoconductive, osteoinductive, and osteogenic constructs for bone repair and regeneration. The strategy in this research work is to use a cell-secreted extracellular matrix (ECM) to influence the osteoblastic differentiation of marrow stromal cells (MSCs).

The effects of an *in vitro* generated ECM on MSC osteoblastic gene expression under static culture indicated that MSCs differentiated down the osteoblastic lineage evidenced by significant increases in expression of the osteoblastic markers, such as collagen type I and osteocalcin. When cultured on an ECM, osteoblastic differentiation was accelerated and enhanced through (1) earlier upregulation of osteopontin and osteocalcin and (2) maintenance of a high level of expression of these and other osteoblast-specific genes. The upregulation in osteoblastic gene expression leading to significant increases in calcium deposition is likely mediated through the interactions between the growth factors and other matrix molecules found in the *in vitro* generated ECM since the expression of insulin-like growth

factor, vascular endothelial growth factor, fibromodulin, and dentin matrix protein was found to display significant peaks in expression level.

To further modulate MSC differentiation, the cellular constructs were cultured in the presence of fluid shear stresses. The effects of fluid shear stress and the bioactivity of the *in vitro* generated ECM acted synergistically to enhance mineralized matrix deposition. However, this synergy occurred only when the constructs were cultured in the presence of dexamethasone. The spatial distribution of cells and ECM was markedly improved compared to static culture.

The osteoinductive and angiogenic potential of ECM constructs generated in a flow perfusion bioreactor for different peroids of time were tested in an ectopic site in a rodent model. No osteoinduction was observed although an increase in the number of blood vessels within the implants with increasing ECM was noted. This study emphasized the challenges in creating ideal conditions for *de novo* bone formation and underscored the need for optimization of this strategy for *in vivo* applications.

These studies led to the transition from titanium to polymeric fiber scaffolds generated via electrospinning. The system was used to fabricate scaffolds with varying fiber diameters and pore sizes as well as multi-layered scaffolds. It was demonstrated that nanofibers could inhibit the spatial distribution of cells and ECM, despite culture in the bioreactor. These scaffolds hold tremendous potential as

tissue engineering scaffolds and will be investigated further as part of the cell-secreted ECM-based scaffold strategy.

ACKNOWLEDGEMENTS

"It was the best of times, it was the worst of times; it was the age of wisdom, it was the age of foolishness; it was the epoch of belief, it was the epoch of incredulity; it was the season of Light, it was the season of Darkness; it was the spring of hope, it was the winter of despair; we had everything before us, we had nothing before us; we were all going directly to Heaven, we were all going the other way."

That, I suppose, can sum up the life of many a graduate student. And so it is now, at the culmination of four and a half years of dedicated work, that I submit, with great humbleness, my heartfelt thanks to those who, without their assistance, advice, and camaraderie, would have made this arduous journey, with its many pitfalls and challenges, less fruitful and enjoyable, and certainly one of disquieting solitude.

To my advisor, Antonios G. Mikos, and thesis committee members, Drs. John A. Jansen, K. Jane-Grande Allen, and Jeffrey G. Hartgerink,

> Thank you for your support, patience, guidance, and encouragement throughout the success and failures. The time and counsel freely and abundantly given to me added considerably to my graduate experience.

To Dr. Alan W. Yasko, Dr. Rena S. D'Souza, and Adriana Cavender,

> Thank you for giving me the opportunity to explore the world outside of Rice. I have learned much from each of you during our collaborative efforts.

To Upma Sharma,

> Special thanks are awarded to you for sharing in the tribulations and frustrations that accompanied the bioreactor. Special thanks are awarded to you for persevering in the tribulations and frustrations that accompanied me. You have made a profound and tremendous impact on my life. Seriously.

To the Mikos Research Group,

> Thanks for the good times and memories. You guys were like a second family to me (at least the downstairs). Thank you Rudolf Meszlenyi for instilling within me the Swiss standards of cell culture. It proved and will continue to be invaluable. Jan Brunn, thank you for all the support that you did with the organization of the lab. Xinfeng, you proved a worthy comrade and companion when all others had abandoned the fort. Thank you Xinfeng, Amit, and Hansoo for your guidance and advice throughout the years. Sue Anne, Jiehong, and Xuan, thank you for the luncheons and your kindness. To you Richard, I wish you the best of luck on the continuation of the project.

Despite the bitter and long-lasting rivalry between the upstairs and downstairs labs, I would like to also extend thanks to everyone who resides upstairs for being like a third family and providing a friendly and supportive atmosphere to work in. Simon, thanks for all the stimulating discussions and for helping me perfect my tennis technique. Sheila and Zarana, Wednesday nights were a beacon of light in what were sometimes dark days. Thank you Anita for all the help with RT-PCR. Thanks to Leda for her organization of the lab environment and duties. Thank you Jim and Matt for lightening the atmosphere with your sarcastic humor; it provided a welcome relief from the daily grind. Thanks Andrea for your optimism and words of encouragement.

To the post-docs, you chose poorly in siding with the upstairs, but your gracious dispensation of knowledge to everyone in the lab makes amends. Michael, Elizabeth, and Balu, you provided a model to which I should strive towards. Thank you Kurt for editing and proof-reading my work.

To the Athanasiou Research Group,
For making me an honorary member and providing a refuge of sanity during desperate times, I am truly grateful. Jerry, your advice and stories were invaluable and are gratefully received. Thanks for teaching me the ways of the cryostat. Thanks Eugene and Chris for your companionship and conversation. Najumiddin, RGA and Immunobiology would not have been the same without you.

To the Rice Bioengineering Department,
I would like to thank Mauricio, Rosa, Arnez, Araceli, Cheryl, Valda, and Cindy for all the work and support that they provided and for reducing the number of speed bumps that one may encounter along the way.

To my friends,
David, Albert, and Wai. Thanks for making the visit to Houston and keeping an old friend company. Your friendship all these years means the world to me. Rikhav, Muk, and Kelly, thanks for regularly checking up on me and keeping my virtual company.

To my family,
Thanks for enduring this long time without your favorite son and brother. I love you.

Table of Contents

List of Tables

List of Figures

Chapter 3

Chapter 4

CHAPTER 1

THESIS OVERVIEW

Approximately 1 million orthopedic surgeries requiring the use of bone graft substitutes are performed annually in the United States alone. Traditional treatment strategies use bone grafts obtained either from allogeneic, autogeneic, or even xenogeneic sources. While these materials are osteoconductive, osteoinductive, and osteogenic, there are disadvantages with their use, such as limited availability, risk of disease transmission, or poor integration with the host tissue. Other strategies include using metals or ceramics, but concerns with osseous integration and immune responses need to still be addressed. Clearly, there is a need for alternatives to existing treatment of bone defects caused by trauma, tumor resection, pathological degeneration, or abnormal development. The field of tissue engineering seeks to recreate the structural and functional aspects of native tissue by integrating elements from the paradigm of cells, scaffolds, and bioactive molecules.

The interactions between cells, scaffolds, and bioactive molecules are inherently complex. This research work is designed to better understand the factors that affect marrow stromal cell (MSC) osteoblastic differentiation in an effort to create osteoconductive and osteoinductive tissue engineered constructs that will promote bone regeneration and repair. *In vivo*, the differentiation of MSCs is dependent on a number of parameters including extracellular matrix proteins and signaling

molecules as well as mechanical forces exerted upon the cells. Therefore, from a biological perspective, the goal is to modulate the differentiation of MSCs down the osteoblastic lineage when seeded onto three-dimensional porous scaffolds. The central hypothesis of this research is that marrow stromal cell function and differentiation are influenced by scaffold properties and culture environment (i.e., static versus dynamic). In order to investigate these objectives, the following specific aims were proposed and investigated:

1. *Evaluate the osteoblastic gene expression of marrow stromal cells cultured on an in vitro generated extracellular matrix deposited by cells*

2. *Determine the osteoinductive capacity of an in vitro generated extracellular matrix on the proliferation and osteogenic differentiation of marrow stromal cells cultured in a flow perfusion bioreactor*

3. *Develop and build an electrospinning system and use it to fabricate and characterize electrospun polymeric scaffolds with various fiber diameter sizes and to characterize marrow stromal cell function on these scaffolds*

This thesis begins with an introduction emphasizing aspects of bone tissue engineering pertinent to this thesis work, including osteogenesis, biomaterial scaffolds, and flow perfusion bioreactors. Chapter 3 establishes the concept of using an ECM secreted by MSCs as a means to influence gene expression and osteoblastic differentiation. Expanding on this idea, the theme of Chapter 4 is flow perfusion bioreactors and how they can be used to generate ECM scaffolds and further enhance MSC osteoblast differentiation. The osteoinductive potential of

ECM-based constructs generated in a bioreactor in an *in vivo* rodent model is investigated in Chapter 5. The subsequent chapters of this thesis then represent a shift in focus with regards to the scaffold type, transitioning from non-biodegradable titanium scaffolds (which allowed experimentation without the need to factor in the effects of degradation) to degradable polymer-based scaffolds generated via an electrospinning process. Chapter 6 presents a review of the electrospinning technique and its application in tissue engineering followed by chapter 7, which provides a description of the electrospinning apparatus developed to fabricate unique polymeric fiber scaffolds along with an analysis of their potential use as tissue engineering scaffolds. Chapter 8 presents the conclusions of this thesis and future directions of the research.

CHAPTER 2

BONE TISSUE ENGINEERING

Abstract

Bone is a structural tissue that is composed of both organic and inorganic phases. Despite its rigid form, bone is very much "alive" and continually in a state of active bone deposition by osteoblasts and resorption by osteoclasts, which allows for self-healing potential. Repair and regeneration of osseous defects requires the recruitment and differentiation of osteoprogenitor cells into mature osteoblasts, a process that is affected by bioactive signaling molecules and extracellular matrix proteins. In situations where the natural ability of bone to repair itself is insufficient, bone graft substitutes are required to obtain functional repair. The field of bone tissue engineering has emerged in an effort to address the need for bone graft substitutes by combining cells, scaffolds, and bioactive factors to create graft materials that replace or encourage osseous restoration. Scaffolds, such as those that are fabricated via electrospinning, act as a physical support for cell attachment and provide a three-dimensional template for cell development and tissue regeneration. To encourage cellular and extracellular matrix distribution inside a tissue engineering scaffold, bioreactors are often employed to provide a dynamic culture environment. Flow perfusion bioreactors, specifically, force fluids through the interconnected porosity of the scaffold, which mitigates mass transport limitations, provides mechanical stimulation, and enhances cell and matrix distribution in a

controlled manner. Successful bone tissue engineering strategies will rely on an understanding of both bone biology and engineering concepts.

Bone Anatomy

Bone is a dynamic tissue that continually remodels itself in response to aging, hormonal changes, cytokine signaling, and physiological and physical stimuli [1]. Specifically, osteoblasts and osteocytes are responsible for deposition and maturation of the osteoid while osteoclasts account for bone resorption [2]. A dynamic equilibrium exists between these cells that allows for continual remodeling of bone throughout life. The exact mechanism by which this occurs is complex and remains to be elucidated.

Mature bone consists of two main components: an inorganic phase composed of mainly hydroxyapatite (~70%) and an organic phase (~25%) composed of various proteins and extracellular matrix [3]. Bone ECM consists of 90% collagen type I with noncollagenous proteins comprising the remaining 10% [4]. The ECM plays an important role in bone regulation as it contains various adhesion proteins, such as fibronectin, fibrillin, vitronectin and that can modulate bone activity by mediating signals to bone cells through these interactions [5].

Characteristic of bone is its natural ability to heal as illustrated by the processes observed during fracture healing. First, osteprogenitor cells migrate to the wound area, attach, proliferate, and differentiate into osteoblasts, which secrete bone-like matrix. This osteogenic developmental progression has been defined as stages of proliferation, ECM maturation, and matrix mineralization [6]. The transition of a cell from the first to the second stage requires a commitment to the osteoblast

phenotype. The second transition requires signals for matrix mineralization, which promote the end of osteoblast differentiation and the beginning of an osteocyte phenotype [7]. However, sometimes the defect may be too large and bone repair does not occur due to insufficient self-generation potential. Thus, external intervention is required.

Osteodifferentiation

The use of pluripotent stem cells for tissue repair is a viable alternative to the problem of organ shortage. Although there are ethical concerns with the use of embryonic stem cells, there are no such worries concerning adult stem cells, which can be easily harvested from the patient. An easily accessible source of adult stem cells comes from bone marrow [8, 9]. Marrow stromal cells (mesenchymal cells, MSCs) are pluripotent cells found predominantly within the bone marrow that are undifferentiated but, when given the proper environmental stimuli, can potentially differentiate into various tissue types including but not limited to bone, cartilage, and adipose [8]. Recently, MSCs have become a popular cell source for tissue engineering strategies because they can be easily isolated and rapidly amplified *ex vivo* without losing their pluripotency [10].

The sequential stages of osteoblast differentiation are marked by changes in phenotypic expression [11, 12]. During the proliferative stage, there is upregulation of histone, collagen, and transforming growth factor beta (TGF-β) production [7]. As proliferation decreases and ECM maturation begins, alkaline phosphatase (ALP)

activity increases [7]. ALP is an enzyme that is primarily secreted by the liver and bone; the bone-specific isoform of ALP occurs as a tetrameric glycoprotein found in the plasma membrane of osteoblasts and is believed to play a role in preparing the ECM for mineralization [13]. Its expression has been found to peak following the proliferative stage of osteoblast differentiation during matrix maturation [14]. As mineralization begins, ALP activity declines accompanied by increases in osteopontin (OPN), osteonectin (OCN), and osteocalcin (OC) production [7, 15]. OPN secretion typically increases before the onset of matrix mineralization. It binds to Ca^{2+} and contains an RGD-sequence for cell attachment [16]. OCN is also a calcium-binding protein with the ability to nucleate hydroxyapatite deposition and was thought to be a bone-specific protein; however, it is expressed by other connective tissues and cells associated with mineralization [5, 17]. OC is also a calcium-binding protein that interacts directly with hydroxyapatite and is considered a bone-specific product of osteoblasts [15, 18].

Osteoblasts are of mesenchymal origin, arising primarily from stromal cells found in bone marrow. Their development may be regulated by transcriptional factors, hormones, growth factors, cytokines, and combinations thereof [5]. *In vitro,* the differentiation path of MSCs depends on the culture conditions [8, 19]. For example, culturing MSCs at high densities in the presence of TGF-β induces the chondrocytic lineage [20], while for osteodifferentiation, the culture media is often supplemented with dexamethasone, β-glycerophosphate, and ascorbic acid [21]. Specially, the glucocorticoid dexamethasone (dex) has been found *in vitro* to be a powerful

promoter for the recruitment and differentiation of osteoprogenitor cells by acting as a paracrine or autocrine factor [4, 22]; exposure of MSCs to dex leads to enhanced phenotypic expressions typical of bone cells [23]. Although its exact inductive mechanisms are unknown, it is believed to involve activation of core binding factor (Cbfa1) and osterix, two osteoblast-specific transcription factors implicated in the development of mature osteoblast phenotypes [5, 7, 10]. The gene for Cbfa1 is believed to be a master controller for osteoblast differentiation and function [7].

Osteogenic Bioactive Molecules

In vitro, the differentiation of osteoprogenitor cells into osteoblasts can be modulated by various bioactive molecules, which may be loosely categorized as growth factors, cytokines, and hormones. The numerous factors involved in in vivo bone formation and maintenance indicate that for ideal osteoblast differentiation to occur in vitro, a complex set of spatial and temporal environmental cues need to be met [7].

Bone growth and development are regulated in part by growth factors that include TGF-β [24], insulin-like growth factors (IGFs) [25], bone morphogenetic proteins (BMPs) [26], vascular endothelial growth factor (VEGF), fibroblast growth factors, and platelet-derived growth factors [27]. The delivery of these bioactive molecules is of particular interest in tissue engineering. The use of these bioactive molecules has been primarily to increase bone formation in fractures and to promote osseous integration with bone implants [28].

The effect of TGF-β on bone cells remains ambiguous as it has been shown to both increase and decrease osteoblast proliferation and differentiation *in vitro* [28, 29]. For example, therapeutic delivery of this growth factor in a controlled fashion by polymeric carriers, such as gelatin microparticles [30], has yielded an enhancement in osteoblast activity [31]. Additionally, there is substantial bone formation *in vivo* after local injections of TGF-β [32]. In contrast, TGF-β was shown to inhibit osteoblast differentiation and nodule bone formation by neonatal rat osteoblasts [33]. It is possible that TGF-β acts indirectly to promote bone formation by regulating the expression of bone matrix macromolecules such as OPN, OCN, OC, ALP, and BMPs [28, 33]. BMPs are a subset of the TGF-β family of proteins that have been shown to stimulate bone formation *in vitro* and *in vivo* [34]. They are often incorporated into different types of scaffolds for controlled release and induction of bone formation [35-37].

IGFs are often found in bone matrix and are thought to influence osteoblastic expression of type I collagen and may also act as an autocrine factor to increase osteoclast formation [28]. A study revealed a synergistic link between IGF-1 release and fluid shear stress on the proliferation of osteoblast-like cells [38].

VEGF is a particularly interesting growth factor because of its critical role in bone formation via its involvement in angiogenesis [39]. Whether VEGF itself has stimulatory effects on osteoblastic differentiation remains unclear, although its expression has been shown to increase with the onset of mineralization during

osteoblastogenesis [40]. *In vivo,* endochondral bone formation is inhibited by inactivation of VEGF [41, 42].

Other bioactive molecules that affect phenotypic and genotypic expression of osteoblast-like cells include the previously discussed glucocorticoid dexamethasone, retinoic acid, vitamin D, and parathyroid hormone (PTH) [36, 43, 44]. These molecules often work together to regulate bone deposition and resorption. Although retinoic acid does not directly influence osteoblast differentiation, it may have a role in regulating the expression levels of IGFs [45, 46]. 1,25-dihydroxyvitamin D3 has been shown to act synergistically with BMP-2 to increase ALP activity in bone MSC cultures [47]. PTH is involved in both bone formation and resorption with prolonged, continuous exposure leading to bone loss while periodic exposure promotes bone formation [48].

Bone Tissue Engineering Scaffolds

There has been a substantial amount of research on developing biodegradable polymeric scaffolds for use in tissue engineering applications. Scaffolds can have a random structure (such as those produced from particulate leaching, fiber bonding, and electrospinning (see Chapter 6) [49-51] or possess a more precise and controlled framework (such as those produced from fused deposition modeling and other rapid prototyping techniques [52, 53]. In addition to different geometries, scaffolds can be fabricated from both biological and synthetic polymers. This

diversity in scaffold fabrication technology and biomaterials has generated an immense library of scaffolds with which to investigate and explore.

Typical bone tissue engineering scaffolds include ceramics, metals, and polymeric biomaterials. Calcium phosphate ceramics, such as commercially available hydroxyapatites, β-tricalcium phosphates, and biphasic calcium phosphates, resemble the mineral content of bone, are bioactive, and are osteoconductive [54]. It has been shown that coating metals with a layer of calcium-phoshpate changes the chemical composition of the scaffold, making it more suitable for differentiation of osteoblast-like cells [55]. Rodrigues et al. incorporated both the organic and inorganic components of bone by fabricating a composite scaffold consisting of collagen and hydroxyapatite; human osteoblasts attached and spread well on those scaffolds [56]. The effectiveness of a bone tissue engineering scaffold will therefore depend on its ability to allow and induce bone formation by osteoblasts.

Polymeric Scaffolds in Tissue Engineering

Poly(glycolic acid) and Poly(lactic acid)

Poly(glycolic acid) (PGA) and poly(lactic acid) (PLA) are two poly(α-hydroxy esters) that are often incorporated into tissue engineering strategies and have been used in the medical industry as FDA-approved sutures [57, 58]. Both polymers undergo degradation by bulk hydrolysis of ester linkages [59]. By forming copolymers of PLGA and PLA at different ratios, the mechanical and degradation properties can be controlled; thus, their uses can accommodate different bioengineering strategies.

Both types of scaffolds are conducive to cell attachment and proliferation for a variety of cell types, such as chondrocytes, osteoblasts, and MSCs. However, the acidic by-products of degradation can lead to inflammatory responses and an unsuitable environment for cells [60].

Polycaprolactone

Polycaprolactone (PCL) is an aliphatic polyester and also an FDA-approved material; it is semi-crystalline, biodegradable, and bioresorbable. With regards to bone tissue engineering, there are several groups that are investigating PCL as a scaffold for various types of osteoblast-like cells. A study done by Rohner et al. showed the efficacy of using MSCs seeded on a PCL scaffold in the reconstruction of craniofacial defects [61]. Other groups have shown that incorporation of hydroxyapatite crystals, which mimic the mineral phase of bone, helps to promote osteoblast differentiation. Additionally, the compliancy of PCL allows it to be formed into shapes, which can be potentially advantageous concerning irregular defects. PCL is currently regarded as a material capable of both soft and hard tissue engineering [52].

Poly(propylene fumarate)

Poly(propylene fumarate) (PPF) is an unsaturated linear polyester synthesized in our laboratory that has been well characterized. The polymer is designed as an injectable, *in situ* crosslinkable, degradable polymer that can fill irregular bone defects [62]. Its crosslinkable nature results in enhanced mechanical properties that

make it suitable for orthopedic applications [63, 64]. A PPF/β-tricalcium phosphate composite scaffold was shown to be an osteoconductive material for MSCs [65].

Electrospinning

Techniques such as fiber bonding, solvent casting, fused deposition modeling, and 3D printing have been employed to produce tissue engineering scaffolds [52, 66]. While the results using these scaffolds are promising, the scaffolds lack nanoscale elements. Nanofibrous scaffolds are produced in one of three techniques: phase separation, self assembly, and electrospinning [67]. Of these methods, electrospinning is the most simple and versatile technique in creating continuous fibers of nanoscale dimensions. The technique was initially studied by Zeleny in 1917 and patented in the early 1930s by Formhals for use in the textile manufacturing industry [68]. The principle behind the technique is the application of an electric field to draw a charged polymer solution from a syringe tip towards a grounded collector; as the jet of solution travels through the air, the solvent evaporates, forming a fine fiber [69]. The process requires little polymer and is a cost-effective means of producing scaffolds.

The resulting fiber diameters of electrospun scaffolds depend on a variety of factors including but not limited to the viscosity of the polymer solution, the applied voltage, distance to collecting mat, syringe diameter, and/or rate of syringe pump [70-72]. An estimation by Baumgartern shows a dependence of fiber diameter and solution viscosity such that $d \approx \eta^{0.5}$ [68]. The addition of surfactants can result in smaller and

more uniform fiber diameters [73]. Although the technique has been known for a while, modeling of the jet fiber is still under investigation. By treating the fluid jet as a slender viscous object, the fiber diameter size has been predicted by

$$h = \left(\gamma \bar{\varepsilon} \frac{Q^2}{I^2} \frac{2}{\pi(2\ln\chi - 3)} \right)^{1/3}$$

where h is the fiber diameter, γ is the surface tension, $\bar{\varepsilon}$ is the dielectric constant, Q is flow rate, I is electric current, , and χ is a dimensionless number representing the wavelength of the instabilities responsible for the whipping jet [71]. However, because each polymer possesses unique properties (i.e., conductivity) equations such as this serve only to present an overall representation of the process.

Over one hundred natural and synthetic polymers, including collagen, elastin, PGA, PLA, PCL, and copolymers thereof, have been successfully spun, each under different conditions. In general, electrospun scaffolds exhibit a wide range of pore diameters, high porosity, high surface to volume ratio, and are morphologically similar to collagen fibrils [74]. Recently, the biomedical and biotechnology industries have begun investigating electrospun scaffolds for use in drug delivery, wound healing, and tissue engineering strategies [75].

A more in depth review of the electrospinning process and its applications for tissue engineering can be found in Chapter 6.

Flow Perfusion Bioreactor

There are many studies showing the effectiveness of various types of scaffolds (including electrospun nanofibrous meshes) as suitable tissue engineering constructs. However, a significant limitation in these studies is that they were performed in static culture; the results suggest that the diffusional limitations of nutrients and waste may limit the amount of tissue in-growth [76-78]. To overcome this challenge, various dynamic culture systems or bioreactors have been designed in order to mitigate this mass transport diffusional limitation [77, 79]. For example, spinner flasks, rotating-wall bioreactor, concentric cylinder, and perfusion culture systems have been designed and have shown various improvements in uniform cell attachment and cellular responses [80-83].

A comparison between spinner flask and rotating-wall bioreactor culture with the flow perfusion bioreactor developed in our laboratory showed that flow perfusion resulted in more favorable cellular responses [84]. Flow perfusion cultures have previously been shown to increase MSC viability and proliferation in the center of constructs [85] and also allow for extended culture periods [86]. In addition to mitigating the problem of mass transport, the cells inside the flow perfusion bioreactor experience mechanical stimulation in the form of fluid shear forces. Another advantage to the flow perfusion bioreactor is the increased distribution of cells and ECM throughout the thickness of the scaffold. This is particularly important with regards to nanofibrous scaffolds; although many studies have shown favorable cell attachment

and growth, it is most often as a monolayer [87]. In other words, there is very little migration of cells into the depths of the scaffold, which is possibly due to the characteristic small pore size of nanofibrous scaffold. Exposure to fluid flow could influence attached cells to migrate into the depths of the scaffold as has been observed with microfibrous scaffolds [76].

Characteristic of bone is that it undergoes mechanical, shear, and hydrostatic forces *in vivo*. Several studies looking at the effects of short and long term fluid shear have been conducted. There is evidence suggesting that fluid shear stress alone (as opposed to mechanical strain) enhances osteoblastic differentiation [88] and has a greater impact on bone stimulation than hydrostatic compression [89]. *In vivo,* bone cells experience interstitial fluid shear stress upon mechanical loading of bone through fluid flow inside the canalicular-lacunar and trabecular spaces within bone tissue [90]. Fluid flow shear stresses have been shown to increase 3D marrow stromal osteoblast mineralized matrix deposition in a dose dependent manner [91]. Although the exact signal transduction mechanisms are not understood, fluid shear has been shown to upregulate osteoblast-related genes, transcription factors, and secondary messengers [92-94]. Furthermore, studies done in our lab have shown that exposure to fluid shear for periods of days can increase alkaline phosphatase activity and calcium deposition of marrow stromal osteoblasts cultured on titanium fiber mesh [14].

A flow perfusion bioreactor has been developed in our laboratory that provides fluid shear stress during *in vitro* culture of MSCs seeded onto a porous scaffold for extended periods of time [83]. Because of the lack of vasculature in *in vitro* culture, cells must rely on diffusion for nutrients. This becomes a problem as the scaffolds become larger and thicker; cells in the center of the scaffold will not have sufficient nutrient/waste exchange and therefore will be less active or even necrotic [78]. The perfusive flow of the bioreactor mitigates the mass transport diffusional limitations of static culture. It has been shown that tissue culture systems that are dynamic can enhance nutrient exchange and cell growth *in vitro* [77, 84, 95].

The bioreactor consists of block made of poly(methyl methacrylate) (PMMA, Plexiglas®) that contains six hollow chambers. Each chamber can house a cassette and each cassette contains a scaffold. Screw caps can be tightened over the chambers for a tight seal preventing leakage of culture media during operation. Six individual flow loops are created by silicon tubing connected to the top and bottom of each chamber. The bottom tubing connects to a collecting reservoir, which drains into a second, collecting reservoir. Media is drawn and run through the closed circuit by means of a peristaltic pump [83].

Although the shear forces experienced by the cells in the flow perfusion bioreactor cannot be precisely modeled, it is presumed that the shear forces generated are directly related to the fluid flow rate of the culture media being perfused.

Furthermore, by approximating the fiber mesh sizes as cylindrical pores, estimates of the shear forces, τ_w, at the fiber surface can be determined by

$$\tau_w = \left(\frac{\mu Q (\Delta P / L)^3}{2\pi} \right)^{1/4}$$

where μ is the fluid viscosity, Q is the flow rate, ΔP is the fluid pressure drop and L is the scaffold length. Estimates of the initial shear forces experienced by these cells in the flow perfusion have been on the order of 0.3 to 1 dyne/cm^2 to [91, 96]. Because attached cells will secrete and deposit ECM, the porosity and pore size of the construct will decrease, exposing the cells to increasingly higher fluid shear stresses as the culture period continues [91].

Summary

Bone tissue engineering strategies are diverse and interdisciplinary. The approach taken in this thesis work is distinguished by employing a combination of porous scaffolds and a flow perfusion bioreactor to modulate the osteodifferentiation of MSCs towards generation of a construct capable of inducing bone regeneration and repair. Scaffolds with an interconnected porous network provide an osteoconductive platform for the 3D culture of MSCs. The flow perfusion bioreactor provides a dynamic culture environment whereby cells are exposed to mechanical stimulation in the form of fluid shear stresses.

CHAPTER 3[*]

AN *IN VITRO* GENERATED BONE-LIKE EXTRACELLULAR MATRIX ENHANCES THE OSTEOBLASTIC GENE EXPRESSION OF MARROW STROMAL CELLS

Abstract

The function and development of cells rely heavily on the signaling interactions with the surrounding extracellular matrix (ECM). Therefore, a tissue engineering scaffold should mimic native ECM to recreate the *in vivo* environment. Previously, we have shown that an *in vitro* generated ECM secreted by cultured cells enhances the mineralized matrix deposition of marrow stromal cells (MSCs). In this study, MSC expression of 45 bone-related genes using real-time reverse transcriptase polymerase chain reaction (RT-PCR) was determined. Upregulation of osteoblastic markers such as collagen type I, matrix extracellular phosphoglycoprotein with ASARM motif, parathyroid hormone receptor, and osteocalcin, indicated that the MSCs on plain titanium scaffolds differentiated down the osteoblastic lineage and deposited a mineralized matrix on day 12. Significant mineralized matrix deposition was observed as early as day 4 on ECM-containing scaffolds and was associated with the enhancement in expression of a subset of osteoblast-specific genes that included a 2-fold increase in osteopontin expression at day 1 and a 6.5-fold increase in osteocalcin expression at day 4 as well as downregulation of chondrogenic gene markers. These results were attributed to the cellular interactions with growth factors and matrix molecules that are likely present in the *in vitro* generated ECM

---

[*] This chapter was prepared as presented for submission to Biomaterials

since the genes for insulin-like growth factor 1, insulin-like growth factor 2, vascular endothelial growth factor, dentin matrix protein, collagen type IV, cartilage oligomeric protein, and matrix metalloproteinase-13 were significantly upregulated during ECM construct generation. Overall, the data demonstrate that modulation of MSC differentiation occurs at the transcriptional level and gene expression of bone-related proteins is differentially regulated by the ECM. This study presents enormous implications for tissue engineering strategies, as it demonstrates that modification of a biomaterial with an *in vitro* generated ECM containing cell-generated bioactive signaling molecules can effectively direct gene expression and differentiation of seeded progenitor cell populations.

Introduction

A common theme among tissue engineering strategies is to combine cells and biomaterial scaffolds for the purpose of generating engineered hybrid constructs for tissue repair. Because of their ability to be manipulated to form different tissue types, marrow stromal cells (MSCs) isolated from the bone marrow are regarded as a viable source of cells for regeneration of tissues. This heterogeneous cell population contains progenitor cells that can be coaxed to differentiate into a gamut of cell types (both *in vitro* and *in vivo* under various different mechanisms) that include adipocytes, chondrocytes, osteoblasts [1], and more recently, myocytes, hepatocytes, and glial cells [2-4]. Furthermore, they are easily isolated from the bone marrow and can be expanded *ex vivo* to large numbers without losing their multipotency. Therefore, it is not surprising that the therapeutic potential of marrow stromal cells has been investigated *in vivo* by transplanting them (either alone or in conjunction with carrier scaffolds) into defective tissue sites that require healing [5, 6].

Differentiation of MSCs into bone-forming cells is critical for the regeneration of bone defects. An approach that is widely investigated is to seed progenitor cells on a biomaterial scaffold and to subsequently modulate cell development. The purpose of a scaffold is not only to serve as a three-dimensional structural framework for cell attachment and growth, but also to promote or enhance a specific cellular response from attached cells. However, a scaffold alone is frequently insufficient to elicit a specific or desired response from cells due to a lack of cell-recognition signals, leading to the design of complementary strategies to augment the efficacy of the

scaffold. For example, biological elements such as collagen or hydroxyapatite can be integrated into a scaffold to make it more closely mimic bone extracellular matrix (ECM) [7, 8], or exogenous growth factors can be incorporated into a scaffold to create a controlled drug delivery system that models the release of ECM-sequestered growth factors *in vivo* [9].

In vivo, transcriptional factors, cytokines, growth factors, and ECM proteins act as autocrine and paracrine effectors to regulate the commitment and differentiation of MSCs into mature osteoblasts [10]. Among its various roles, the ECM can act as a storage reservoir for growth factors and release them when necessary [11, 12]. Realizing the tremendous significance of the ECM milieu on cell differentiation, we have exploited the natural ability of osteoblasts to secrete ECM proteins and growth factors to generate ECM-containing scaffolds as a means to enhance the osteoblastic differentiation of MSCs [13, 14]. Previously, we have demonstrated that *in vitro* generated bone-like ECM produced by MSCs contains bioactive factors including transforming growth factor-b1 (TGF-β1), fibroblastic growth factor-2 (FGF-2), vascular endothelial growth factor (VEGF), and bone morphogenetic protein-2 (BMP-2) [15]. We have also shown that cells seeded onto scaffolds containing bone-like ECM deposit significantly higher amounts of mineralized matrix compared to those on plain scaffolds [13, 14]. The focus of this study, therefore, was to investigate the effects of a bone-like, pregenerated ECM on MSCs at a molecular level, by evaluating their temporal gene expression as they differentiate down the osteoblastic pathway. A total of 45 different bone-related genes were investigated

through real-time reverse transcriptase polymerase chain reaction (RT-PCR) using Taqman® Low Density Arrays (LDAs), allowing for a comprehensive analysis of the genes expressed by MSCs as they undergo culture. The genes were chosen based on evidence from the literature suggesting that they are bone-related and they were broadly categorized into three groups as markers for: (1) osteoblastic/chondrogenic differentiation including transcriptional factors, (2) growth factor expression, and (3) ECM-related proteins. Specifically, the aims of this study were to determine (1) the particular set of bone-related genes expressed by MSCs cultured on titanium (Ti) scaffolds as they undergo osteoblastic differentiation and (2) how a cell-secreted bone-like ECM alters the osteoblastic gene expression profile of MSCs when compared to plain Ti scaffolds.

Methods

Scaffold Preparation

Ti fiber meshes (Bekaert N.V., Zwevegem, Belgium) with porosity of 86% and fiber diameter of 20 μm were die-punched into 8 mm diameter discs (thickness = 0.8 mm). Plain scaffolds were sterilized by autoclaving before use [16].

Extracellular Matrix Scaffold Generation

MSCs were harvested and pooled together from 4 male Wistar rats (Charles River, Wilmington, MA) weighing 150-175 g, according to established protocols [13]. Cells were cultured in the presence of 10^{-8} M dexamethasone for 6 days in complete osteogenic media containing minimum essential media (alpha modification), 10 mM β-glycerophosphate, 50 mg/ml ascorbic acid, (all from Sigma, St. Louis, MO), and

10% (vol) fetal bovine serum (FBS) (Cambrex Biosciences, Walkersville, MD). Cells were trypsinized on day 6, resuspended in a known volume of complete media to obtain a cell solution of 1.25×10^6 cells/ml. A 0.2 ml solution was then added drop wise to each Ti scaffold that had been previously press-fit into seeding cassettes (the scaffolds were also pre-wet with phosphate buffered saline for 1 h prior to seeding). The cells were allowed to attach for 2 h, after which the scaffolds were carefully removed from the cassettes and placed individually into a 12-well tissue culture plate containing 2 ml of complete osteogenic media per well. The constructs were cultured for a total of 12 days with media changes performed every 2 days. At the end of 12 days, the constructs were rinsed with PBS, placed into 1.5 ml of ddH$_2$O and frozen until use.

Rat Marrow Stromal Cell Seeding

The ECM scaffolds were prepared for seeding after they underwent a decellularization process involving three freeze/thaw cycles in liquid nitrogen and a 37°C water bath (10 min each), respectively. The scaffolds were then allowed to air dry in a biosafety laminar flow cabinet overnight prior to seeding. MSCs used for cell seeding of the experimental phase were harvested from another set of 4 male Wistar rats (Charles River, Wilmington, MA) also weighing between 150-175 g. Cell culture and seeding was performed as described above for ECM scaffold generation. Constructs were cultured for 1, 4, 8, 12, and 16 days with media changes occurring every 2 days. At each time point, one sample was harvested for confocal and

scanning electron microscopy and four samples were taken for RNA isolation and subsequent RT-PCR analysis.

Confocal Microscopy

At each timepoint, samples were retrieved from the well plates, rinsed with phosphate buffered saline (Gibco Invitrogen, Carslbad, CA), and stained for live cells by incubating in a calcein solution (2 µM in PBS, Invitrogen, Carlsbad, CA) for 5 minutes and then transferred to a well plate containing PBS. Images were collected using a laser scanning confocal microscope (Zeiss LSM 510 META, Carl Zeiss, Germany) under excitation from an Argon laser (488 nm). Fluorescence emission was detected using the META detector (515 nm, 20 nm virtual bandpass). An NFT515 filter was using to block the autofluorescence of the Ti scaffolds.

Scanning Electron Microscopy Analysis

The same samples used for confocal microscopy were then fixed in 2.5% (vol) glutaraldehyde for 2 h for scanning electron microscopy. The samples were cut in half for analysis of both the top and bottom; additionally, a cross-section was cut. After fixation, the scaffolds underwent an increasing ethanol gradient series to 100%. Samples were then dried under a laminar flow hood, mounted on aluminium stages, sputter coated with gold, and examined with an FEI Quanta 400 Environmental Scanning Electron Microscope (Hillsboro, OR).

RNA Isolation and cDNA Synthesis

Total RNA from cellular constructs was isolated using the RNeasy® Mini Kit (Qiagen, Valencia, CA). Briefly, constructs were rinsed in sterile PBS and placed in 600 µl of lysis buffer provided with the kit. After mixing by pipetting, the lysate was transferred to a Qiashredder column (Qiagen, Valencia, CA) for homogenization as detailed by the manufacturer. An equal volume of 70% ethanol was then added to the collected lysate and mixed by pipetting. RNA cleanup was performed with the RNeasy mini-column following the animal cell protocol provided by the manufacturer with a few modifications to improve the purity of RNA. These included two 350 µl washes of buffer RW1 (provided by kit) prior to the 700 µl wash of buffer RW1 and a final 70% ethanol wash after the second buffer RPE wash (provided by kit) and before the optional drying step. Quality control of the RNA was determined using a 2100 Agilent Bioanalyzer (Agilent Technologies, Inc., Santa Clara, CA), which determines the concentration of a sample and also provides an RNA integrity number (RIN), a quantitative estimate of the quality of RNA. The RIN number varies from 1 (degraded RNA) to 10 (completely intact); the RIN values obtained in this study ranged from 7.4 to 9.8 (average of 8.7 ± 0.6), indicating high quality RNA suitable for downstream reactions (i.e., cDNA synthesis and Taqman® LDAs). Synthesis of cDNA from 200 ng of total RNA was carried out using the High-Capacity cDNA Archive Kit (Applied Biosystems, Foster City, CA) following the instructions provided by the manufacturer.

TaqMan® Low Density Arrays

The TaqMan® LDA (Applied Biosystems, Foster City, CA) is a microfluidic card capable of performing 384 simultaneous real-time PCR reactions. The design of the card allowed for analysis of 48 different genes on one card for one group (n=4) in duplicate. The card comes equipped with 8 loading ports to which 100 µl of a solution containing 50 µl of a cDNA solution (100 ng of cDNA in 50 µl of RNase-free water) and 50 µl TaqMan ® Universal PCR Mastermix (2X) is loaded. Each sample was loaded into two separate ports (i.e., samples were run in duplicate). The cards were then placed in Sorvall/Heraeus buckets designed specifically for the TaqMan® array cards and centrifuged 2 times, each for 1 min at 1200 RPM, in order to distribute the solution equally into the individual wells of the plate. PCR was carried out in an Applied Biosystems 7900HT thermal cycler at the following cycling conditions: an incubation at 50°C for 2 min, then 10 min of denaturation at 95°C, followed by 40 cycles of 97°C for 30 sec and 60°C for 1 min. Fold differences were calculated using the delta-delta C_t method as described in [17] with GAPDH as the endongenous housekeeping gene and results were normalized to day 1 Ti samples to obtain fold differences. Consequently, a value of 1 is considered the baseline expression. Table 1 provides a summary of the investigated genes.

Statistical Analysis

Biochemical and gene expression data were analyzed for statistical differences with a two-way ANOVA for scaffold type and time. If a significant difference was determined, multiple pairwise comparisons were performed using the Tukey procedure at a 95% significance level. Categorization of gene expression on Ti

scaffolds as upregulated, expressed, or downregulated, was determined using fold difference cutoffs applied with microarray data to determine specific genes to validate via RT-PCR [18-21]. A gene was considered to be upregulated if there was at least one timepoint with a 1.5 or higher fold difference in expression and if it was statistically higher compared to day 1; a gene was considered to be downregulated if the expression profile exhibited a downward trend with the last three timepoints exhibiting a 0.67 (1/1.5) or lower fold difference in expression and if they were all statistically lower compared to day 1; otherwise, the gene was considered to be expressed (Table 2). The main effects of the ECM (scaffold type) collapsed across time on the overall expression of each gene at 95% and 99% significance levels are provided in Table 3.

Results and Discussion

The purposes of this study were (1) to investigate the temporal expression of bone-related genes by MSCs as they differentiate down the osteoblastic lineage when seeded onto Ti fiber mesh and cultured in standard osteogenic media and (2) to determine how this expression is modulated when the Ti scaffolds contain a bone-like ECM deposited by cells. The number of genes that can be evaluated via traditional RT-PCR methods is typically limited by the amount of RNA isolated from a sample in a particular experiment. Comparisons of gene expression between different experiments, therefore, can be limited due to variability between the different experiments. The design of the present study (i.e., using the Taqman® LDAs) negated the need for more than one experiment, while still allowing for the

simultaneous analysis of 48 different bone-related genes, including multiple endogenous housekeeping genes.

Overall, the gene expression data from the Taqman® LDAs indicated that the MSCs underwent osteoblastic differentiation when seeded onto Ti fiber mesh scaffolds and that their differentiation was enhanced when they were seeded onto the Ti/ECM scaffolds. Tables 2 provides a brief summary of the various genes that were upregulated, expressed, or downregulated by the MSCs on Ti scaffolds, while Table 3 shows the effect of the ECM on the expression profiles of each gene. In general, expression of osteoblast-specific genes was significantly increased when cultured on ECM scaffolds (Table 3). Of the investigated genes, only collagen type II, dentin sialophosphoprotein, vitronectin, and bone morphogenetic protein-7 (BMP-7) were not appreciably detected over the course of culture. Osteocrin was observed for both groups early during the culture but its expression fell to undetectable levels after day 8 (data not shown). The present work illustrates that an *in vitro* generated ECM secreted by MSCs can modulate the temporal gene expression profile of bone-related proteins and ECM molecules.

Osteoblastic Differentiation

The differentiation of MSCs *in vitro* starts with a period of cellular proliferation, followed by ECM deposition, and ultimately mineralization of the matrix [22]. In this study, the amount of calcium deposition was measured as a biochemical marker of osteoblastic differentiation (Figure 1) and confirmed the results of a previous study performed in our laboratory [13]. For both groups, a significant amount of calcium

deposition occurred by day 16 relative to day 1. However, there was approximately a 3-fold difference in mineralized matrix between Ti and Ti/ECM constructs at this timepoint, indicating that the ECM significantly enhanced the mineralized matrix deposition of MSCs. Moreover, calcium deposition for Ti/ECM constructs was already significantly greater (relative to day 1) by day 4 as opposed to day 12 for plain Ti constructs, indicating not only enhanced, but accelerated MSC osteoblastic differentiation.

The process of osteoblastic differentiation is associated with temporal changes in gene expression, although different cell culture models can lead to different expression patterns [23]. In the present study, analysis of the osteoblast-specific gene expression of the MSCs supplemented the calcium data. With the exception of osteocrin, mRNA transcript levels were detected for all the genes considered specific or related to ostebolastic differentiation; Figure 2 shows the temporal expression of these genes for the Ti and Ti/ECM constructs. For the Ti group, a peak in expression of osteoblast-related proteins occurred at day 8 for osteocalcin (OC), parathyroid hormone receptor 1 (PTHR1), collagen type I (COL1), and matrix extracellular phosphoglycoprotein with ASARM motif (MEPE) (Figures 2B, 2F, 2G, and 2H). COL1 is the predominant collagen found in bone and provides a template for mineralization [24] while both OC and MEPE are associated with osteoblast-mediated matrix deposition and mineralization [25, 26]. PTHR1 is the receptor for parathyroid hormone, and its expression has been implicated as both an early and late marker of differentiation [27]. The upregulation of these genes, therefore,

indicates a progression towards an osteoblastic phenotype and can account for the significant increase in calcium deposition observed on day 12 for the Ti group. The expression pattern of osteomodulin (OMD) was unique among the osteoblast-related genes, exhibiting a dramatic decline in expression over the culture period (Figure 2E). OMD is a proteoglycan present in mineralized matrix with a high affinity for hydroxyapatite and was previously found to be upregulated in the culture of primary osteoblasts isolated from rodent calvaria [28, 29]. Although considered a marker of mature osteoblasts, previous studies showed that OMD may be dependent on osteoclasts as its expression was reduced in mice lacking osteoclast activity [28]. Since the MSCs are isolated from the bone marrow and the culture conditions lacked osteoclasts, this may account for the declining expression pattern.

The ECM appeared to have profound effects on alkaline phosphatase (ALP), OC, osteopontin (OPN), osteonectin (OCN), OMD, and PTHR1 by (1) significantly upregulating their expression and/or (2) sustaining their expression levels for a longer period when compared to the Ti group (Figure 2). The divergent expression of ALP, which is an early indicator of osteoblast differentiation [22], between Ti/ECM and Ti constructs beginning at day 4 suggests enhanced osteoblastic differentiation or the beginning differentiation of a greater number of cells (Figure 2A). Lending further credence to this interpretation was the expression profile of OPN, which was significantly upregulated by the ECM at day 1 (a 2-fold difference compared to Ti) and continued to maintain a higher expression compared to the Ti group throughout the culture period, peaking again at day 12. The exact role of OPN in bone is

unknown, although it is produced during the period just prior to matrix mineralization [30]. The trends with OC were consistent and complement these observations. OC on Ti/ECM constructs exhibited a rapid linear increase in expression from day 1 to day 8. Since OC is present only in mineralized ECM and is synthesized only by mature osteoblasts, it is considered the most specific marker of differentiated and active osteoblasts [31]. These results are consistent with a study in which human bone marrow cells seeded onto partially demineralized bone matrix expressed early and elevated levels of ALP and OC after 7 days of culture [32]. The enhancement in expression level of these bone-specific markers, especially OC and OPN, implies that the MSCs on Ti/ECM constructs proceeded through an accelerated differentiation mechanism activated by the ECM and provides a basis for the increased matrix mineralization observed at the earlier timepoints in the Ti/ECM constructs. Specifically, a significantly increased amount of calcium relative to day 1 was detected at day 4 in the Ti/ECM group, following the upregulation of OPN at day 1 and occurring with the enhanced expression of OC at day 4.

The second effect that the ECM appeared to have on MSC gene expression was a prolongation of elevated transcript levels of the genes. For example, the peak expression occurring at day 8 for OC on Ti/ECM was similar to that of the Ti group, but was maintained at a significantly high level for a longer duration, evidenced by a 5-fold difference in expression between the two groups at day 12 (Figure 2B). Similar trends were observed for ALP, OCN, and PTHR1 (4-, 5-, and 4-fold difference, respectively, at day 12 between Ti/ECM and Ti) (Figures 2A, 2D, 2F).

These results likely account for the continual differentiation and deposition of significant amounts of calcium in the Ti/ECM group throughout the duration of culture.

The effect of the ECM on COL1 and the transcriptional factors, RUNX2 and DLX5, were not as pronounced as the other investigated genes, as their expression profiles generally paralleled those of the Ti group. A common trend noted with these genes (and all genes in this group) was that by the end of the culture period, expression was higher (although not significantly) on Ti/ECM scaffolds. For example, RUNX2 expression on Ti/ECM constructs, which initially had lower expression, rose significantly by day 4 and maintained a level greater than that on Ti constructs; by day 16, expression on Ti constructs had fallen significantly lower than the baseline, while the same was not true of the Ti/ECM group (Figure 2I). Although the temporal profiles of the two groups for RUNX2 was similar, isolating the main effect of scaffold type collapsed across time revealed that the ECM had an overall effect of increasing RUNX2 expression compared to expression on Ti (Table 3). These observations provide further support to the idea that the *in vitro* generated-ECM helps to maintain expression of osteoblast-specific genes. Furthermore, mRNA of collagen type II, which is secreted primarily by chondrocytes and thus served as a negative control, was not detected at any point during the culture period for the Ti/ECM group; however, for the Ti group, mRNA was detected at small levels beginning at day 8 (data not shown). The upregulation of the genes encoding osteoblast-specific

proteins investigated implies a critical role by these genes in regulating osteoblastic differentiation.

Taken together, the overall data suggests that the ECM contributed to increased osteogenic activity of MSCs by accelerating their osteoblastic differentiation and prolonging osteoblastic phenotypic expression when compared to MSCs on plain Ti scaffolds. The upregulation in osteoblastic gene expression led to significant increases in calcium deposition and is likely mediated through the cellular interactions with growth factors and other matrix molecules found in the *in vitro* generated ECM since a number of these proteins were shown to be expressed by cells on Ti scaffolds (see below). Indeed, we have previously verified the presence of several bone-related growth factors in bone-like ECM generated by MSCs *in vitro* including TGF-β1, BMP-2, VEGF, and FGF-2 [15].

Bioactive Growth Factor Expression

Growth factors are ubiquitous molecules found in the body that act as chemotractants to influence a wide array of biological processes [33]. Bone matrix contains a number of growth factors such as TGF-βs, BMPs, FGFs, VEGF, insulin-like growth factor (IGFs), and platelet derived growth factor (PDGF). The extrinsic addition of these various growth factors and their effects on osteoblast function and development *in vitro* have been well-documented [33-35] and therefore will not be discussed in detail. The results of the present study indicate that a majority of the investigated growth factors are transiently expressed at varying levels by the

differentiating MSCs on Ti scaffolds and thus may be secreted into the ECM. BMP-7 was the only growth factor that was not expressed in either group. BMP-7 was also not detected in MSCs harvested from 10-12 week old C57BL mice and it has been suggested that its source may be from cells other than osteoblasts [36].

For the Ti group, IGF-1, IGF-2, and VEGF exhibited a significant increase in expression compared to their respective day 1 levels (Figure 3A-C). IGF-2 exhibited two peaks in its expression pattern, a 2.5 fold increase at day 4 and a 2-fold increase at day 12. IGF-1 displayed a steadily increasing profile, with a 3- and 6-fold difference at day 12 and 16. The increase of the expression levels of IGF-1, and to a lesser extent for FGF-2 and TGF-β1, towards the end of the culture period suggests a role of these growth factors in the latter stages of osteoblastic differentiation, while IGF-2 plays an earlier role. Both FGF-2 and TGF-β1 mRNA levels initially decreased, but increased significantly in expression from day 8 to 12 and ultimately ended with a 1.4 fold increase in expression from day 1 (Figure 4B, 4F). VEGF demonstrated a sustained 4-fold increase in expression level between days 8 to 12. VEGF is a potent angiogenic factor and its secretion into a scaffold by cells can increase the effectiveness of a scaffold with regard to angiogenesis [9, 37].

In contrast to the increasing expression of the previous genes, the gene expression of TGF-β2 and BMP-6 on Ti scaffolds was significantly downregulated as early as day 4 and continued to be so until the last time point (Figures 3D, 3E). The ECM had no impact on the upregulation of these two genes and instead, seemed to

attenuate their expression level. However, the ECM did upregulate the mRNA levels of BMP-3 and FGF-2 compared to the Ti group (Figures 4A, 4B). BMP-3 expression, which steadily decreased on the Ti scaffolds, was significantly upregulated by the ECM, as evidenced by the 3 and 4.5-fold difference in expression level between the two groups at day 12 and 16, respectively. The ECM also enhanced the expression levels of FGF-2 in a similar fashion, by significantly upregulating its expression compared to the Ti group at days 4, 12, and 16. The ECM, therefore, appears to differentially regulate the gene expression for growth factors.

Other growth factor gene expression profiles by MSCs on Ti scaffolds were also detected and, in general, the mRNA levels tended to decline to a level below the baseline of day 1, although never to an undetectable level (Figures 4C-E, 4G, 4H). On Ti scaffolds, BMP-2, BMP-4, and TGF-β3 displayed a temporal expression pattern consisting of an initial downregulation in expression from day 1, followed by an increase during the middle of culture, and ending with a decrease in expression level (Figures 4C-E). Although the observed rise in expression did not increase significantly from the baseline value (it was significant with respect to the preceding timepoint), this type of profile suggests that a higher peak may exist at a timepoint other than the one measured. Interestingly, on the Ti/ECM scaffolds, the mRNA levels of these same genes (1) were significantly lower compared to the baseline and (2) remained at a relatively constant level. For example, BMP-2 expression on Ti/ECM scaffolds remained approximately one-third the level of the baseline

expression throughout the culture period (Figure 4C). Given the increase in mineralized matrix deposition in the present study, one may have expected to observe a significant upregulation of BMP-2 and other growth factors. It is possible that MSCs cultured on the ECM-containing scaffolds were already in a favorable microenvironment and thus did not require upregulation of these particular genes. Instead, expressing them at a sustained and constant level that, along with the concomitant increase in gene expression for bone-specific matrix proteins (i.e., ALP, OC, OPN, etc.), was sufficient to significantly stimulate mineralized matrix deposition by differentiated MSCs (similar observations were observed for ECM-related proteins, see discussion below and Figures 7H, 7N). Given the increase in osteoblastic gene expression and calcium deposition on Ti/ECM constructs, it appears that the MSCs have a positive interaction with the ECM. Overall, the data showed that the MSCs express the genes for growth factors at different levels and patterns and are regulated in a time-dependent fashion on plain Ti scaffolds.

Extracellular Matrix and Related Protein Expression

In bone, the matrix is composed of not only a mineralized phase, but also a significant organic phase of collagenous and other biological proteins including matrix metalloproteinases, glycosaminoglycans, and glycoproteins, as well as other non-collagenous proteins not specific to bone. This heterogeneous mix of proteins contributes to the mechanical properties of bone and its ability to mineralize collagen as well as osteoblastic differentiation of MSCs mediated through cell-matrix interactions [10, 38, 39]. Figures 5 and 6 show the laser scanning confocal and

scanning electron micrographs of the Ti and Ti/ECM constructs as a function of time and convey a qualitative assessment of cellular proliferation and matrix deposition over time.

In the present study, genes for a mix of ECM molecules including aggrecan (AGC), cartilage oligomeric matrix protein, dentin matrix protein (DMP1), collagen type IV (COL4), and matrix metalloproteinase-13 (MMP-13) were significantly upregulated during the culture period in the Ti group (Table 2, Figure 7B, 7E, 7H, 7K, 7N). This was especially true for DMP1, which experienced a 40-fold peak expression level. DMP1 is thought to regulate the expression of OC and promotes mineralization by nucleating hydroxyapatite crystals [40, 41]; the concomitant rise in expression of both of these genes on day 8 in the Ti group is in accord with this view. In contrast, on Ti/ECM constructs, DMP1 transcript levels remained relatively constant, at approximately a 10-fold difference from the baseline on Ti/ECM (Figure 7H). This is consistent with the trends observed with certain growth factors in the present study. MMP-13 expression exhibited the same tendencies (Figure 7N). A steady 2-fold difference in expression level from the baseline on Ti/ECM constructs replaced the 9-fold peak increase in MMP-13 expression occurring at day 12 on Ti scaffolds. This suggests a possible remodeling of the ECM by cells in both groups. The increasing expression of COL4 is also noteworthy as it is a collagen that is found in basal lamina as opposed to bone matrix (i.e., it is a collagen not produced by osteoblasts) [42]; its significant rise in expression points to the potential existence of a stromal component in the cell culture. This is not surprising as the cells used in this study

were harvested from the bone marrow and stromal cells are present in this heterogenous population of cells.

The effect of the *in vitro* generated ECM on the expression profiles of other ECM proteins was similar to that of the growth factors, where a majority of the genes were again either downregulated or not influenced by the ECM (Table 3). Of considerable note was the expression of AGC, which exhibited a peak in expression at day 8 on Ti scaffolds. Its expression could be attributed to a subset of MSCs not undergoing osteoblastic differentiation in the Ti group. When cultured on the Ti/ECM constructs, however, MSC expression of AGC was significantly downregulated to an almost undetectable level by day 16, providing further evidence that the ECM has an osteogenic effect on the MSCs by enhancing their osteoblastic potential while simultaneously subduing their chondrogenic capacity. One notable exception to the observation that there was decreased expression of matrix molecules on ECM constructs was fibromodulin (FMOD), which on Ti/ECM constructs had significant increases in expression level from day 8 to 16, exhibiting a 2.4-, 2.2-, and 5.0 fold difference, respectively, at these timepoints when compared to expression in the Ti group (Figure 7A). This result implies that the deposited extracellular matrix could be comprised of an organized network of collagen since FMOD binds to collagen and regulates fibrillogenesis, which may have an influence on mineralization [43-45].

This study reinforces the critical importance of cell-biomaterial interactions in scaffold-based tissue engineering strategies. Challenges in biomaterial scaffold

design arise in part due to the desire to control cell function via the scaffold. By providing a microenvironment that mimicked the *in vivo* setting, regulation of MSC osteoblastic gene expression was achieved leading to significant calcium deposition. Thus, a biomaterial scaffold can be effectively modified with an *in vitro* generated ECM to have improved surface characteristics that better govern cellular responses from attached cells, without the need for any chemical treatment or exogenous bioactive factor delivery. This represents a cogent and versatile strategy that can be applied to other tissue engineering biomaterial scaffolds under investigation.

Conclusion

This study revealed the temporal gene expression profiles of bone-related proteins by MSCs cultured in standard osteogenic media. Upregulation of genes encoding osteoblastic-specific proteins and ECM-related molecules and deposition of a mineralized matrix indicated MSC osteoblastic differentiation. Furthermore, the MSCs expressed and upregulated genes for numerous growth factors and extracellular matrix molecules found in native bone tissue. MSC interaction with a bone-like ECM can significantly increase osteoblastic gene expression of freshly seeded MSCs and differentially regulates the transcript levels of a wide array of bone matrix-related proteins, including growth factors. Significant enhancement in the expression level of a number of osteoblast-specific markers and concurrent downregulation of chondrogenic genes on Ti/ECM constructs indicated that the ECM has osteogenic properties that result in substantial increases in mineralized matrix deposition by cells. This study illustrates that modification of a biomaterial scaffold

with an *in vitro* generated ECM containing bioactive molecules produced by cells can be effectively applied to direct progenitor cell differentiation and gene expression, which could have a profound impact on the future development of tissue engineering scaffolds.

Acknowledgements

Table 1. List and description of bone-related genes.

Gene Description	Abbreviation	UniGene ID
Osteoblast-related Genes		
Alkaline phosphatase	ALP	Rn.82764
Bone-gamma carboxyglutamic acid (osteocalcin)	OC	Rn.9722
Collagen type I	COL1	Rn.2953
Distal-less homeobox-5	DLX5	Rn.11248
Matrix extracellular phosphoglycoprotein with ASARM motif	MEPE	Rn.160717
Osteomodulin (osteoadherin)	OMD	Rn.30124
Osteocrin	OSTN	Rn.29193
Parathryoid hormone receptor	PTHR1	Rn.48025
Runt-related transcription factor 2 (Core binding factor 1)	RUNX2	Rn.144216
Secreted acidic cysteine rich glycoprotein (osteonectin)	OCN	Rn.98989
Secreted phosphoportein 1 (osteopontin)	OPN	Rn.8871
Growth Factors		
Bone morphogenetic protein 2	BMP-2	Rn.90931
Bone morphogenetic protein 3	BMP-3	Rn.53974
Bone morphogenetic protein 4	BMP-4	Rn.10318
Bone morphogenetic protein 6	BMP-6	Rn.40476
Bone morphogenetic protein 7	BMP-7	Rn.18030
Fibroblast growth factor 1	FGF-1	Rn.88013
Fibroblast growth factor 2	FGF-2	Rn.31808
Insulin-like growth factor 1	IGF-1	Rn.36966
Insulin-like growth factor 2	IGF-2	Rn.118681
Platelet-derived growth factor	PDGF	Rn.10999
Transforming growth factor beta 1	TGF-β1	Rn.40136
Transforming growth factor beta 2	TGF-β2	Rn.24539
Transforming growth factor beta 3	TGF-β3	Rn.7018
Vascular endothelial growth factor	VEGF	Rn.1923
Extracellular Matrix Molecules		
Aggrecan	AGC	Rn.54503
Biglycan	BGN	Rn.783
Collagen type II	COL2	Rn.10124
Collagen type III	COL3	Rn.3247
Collagen type IV	COL4	Rn.22075
Collagen type V	COL5	Rn.117
Cartilage oligomeric protein	COMP	Rn.10343
Decorin	DCN	Rn.106103
Dentin matrix protein	DMP1	Rn.19340
Dentin sialophosphoprotein	DSPP	Rn.21392
Elastin	ELN	Rn.54384
Fibrillin	FBN	Rn.12759
Fibronectin	FN	Rn.1604
Fibromodulin	FMOD	Rn.8778
Matrix Gla protein	MGP	Rn.2379
Matrix metalloproteinase 3	MMP-3	Rn.32086
Matrix metalloproteinase 9	MMP-9	Rn.10209
Matrix metalloproteinase 13	MMP-13	Rn.10997
Vitronectin	VTN	Rn.87493

Table 2. Summary of the bone-related genes and their expression on Ti scaffolds.

	Upregulated	Expressed	Downregulated
Osteoblast-related Genes	COL1, MEPE, OC, PTHR1	ALP, DLX5, OCN, OPN, RUNX2	OMD
Growth Factors	IGF-1, IGF-2, VEGF	BMP-2, BMP-3, BMP-4, FGF-1, FGF-2, PDGF, TGF-β1, TGF-β3	BMP-6, TGF-β2
ECM Molecules	AGC, COL4, COMP, DMP1, MMP-13	BGN, COL5, DCN, ELN, FMOD, FN, MGP, MMP-3, MMP-9	COL3, FBN

Upregulated = a 1.5 fold difference in expression or higher that is significantly higher compared to day 1 occurs in the expression profile; Downregulated = a consistent downward trend exhibiting a 0.67 fold difference in expression or lower at day 8, 12, and 16 with all timepoints significantly lower compared to day 1. Expressed = genes that are not upregulated or downregulated. The expressions of BMP-7, COL2, DSPP, OSTN, and VTN were not detected.

Table 3. Main effects of the ECM on gene expression compared to Ti.

	Increased Expression	Attenuated Expression	No Difference
Osteoblast-related Genes	***ALP, OC***, OMD*, ***OPN, PTHR1***, RUNX2*		COL1, DLX5, ***MEPE, OCN***
Growth Factors	***BMP-3, FGF2***	BMP-2, BMP-4, BMP-6, TGF-β3, ***VEGF, IGF-1***, IGF2	FGF-1, PDGF, ***TGF-β1***, TGF-β2
ECM Molecules	***FMOD***, MGP	AGC, BGN*, ***COL4***, ELN, FBN, FN, MMP-9	COL3, COL5, ***COMP***, DCN, DMP1, MMP-13, MMP-3

The genes are categorized based on whether the main effect of scaffold type significantly changed the overall gene expression level between Ti and Ti/ECM. Differences between gene expression on Ti and Ti/ECM were found at a significance level $p < 0.01$, unless denoted with a * ($p < 0.05$). Listing of genes in bold-italics indicates that the expression profile exhibited a significant increase in expression from the Ti day 1 expression level (see expression profiles). The expressions of BMP-7, COL2, DSPP, OSTN, and VTN were not detected.
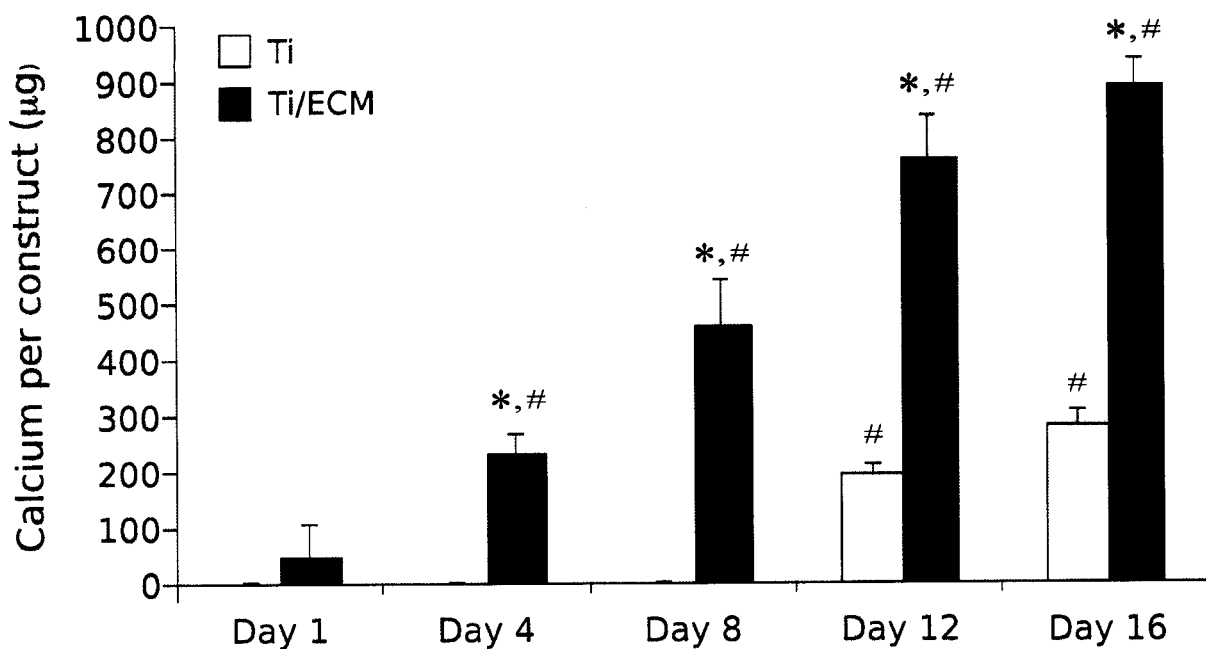
Figure 3-1

Calcium content of Ti and Ti/ECM constructs cultured over the course of 16 days. The data represents the mean of four samples, with the error bars representing standard deviation. Statistical differences ($p < 0.05$) between Ti/ECM and Ti at each timepoint is denoted by an asterisk (*); a # designates a statistical significance compared to day 1 samples within a group.

A.
ALP

B.
OC

C.
OPN

D.
OCN

E.
OMD

F.
PTHR1

G.
COL1

H.
MEPE

I.
RUNX2

J.
DLX5
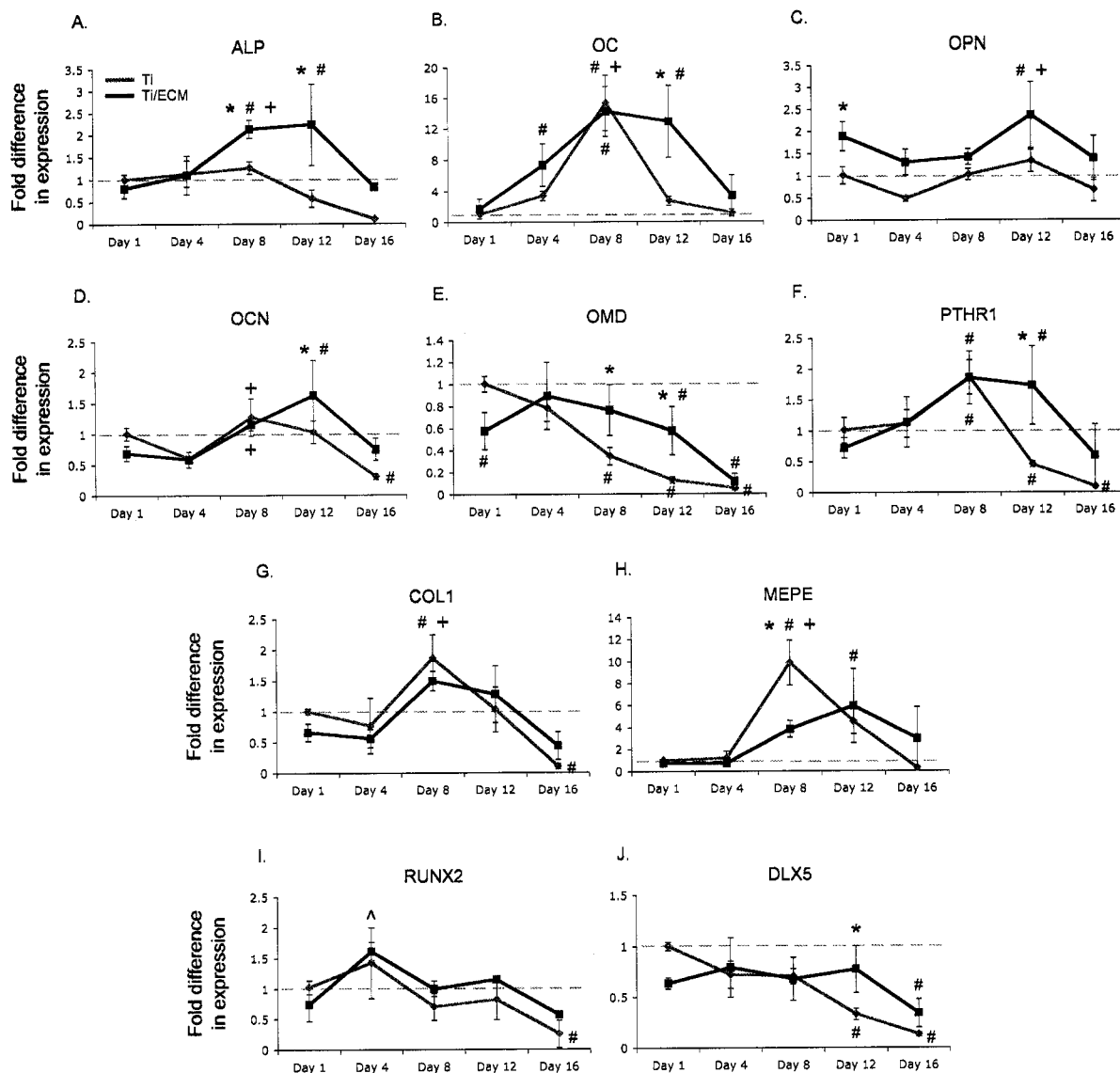
Figure 3-2

Gene expression profiles of bone-specific markers of osteoblastic differentiation as determined by RT-PCR. The data represents fold difference in expression of four samples normalized to Ti day 1 samples. A * indicates a significant difference in expression level at the specified timpoint ($p<0.05$); a # symbol indicates a significant difference in expression level with respect to the baseline ($p<0.05$); a + symbol indicates a significant increase in expression level from the previous timepoint. The blue line represents the Ti group while the black line represents the Ti/ECM group and applies to all graphs. The dashed grey line indicates the baseline expression level.
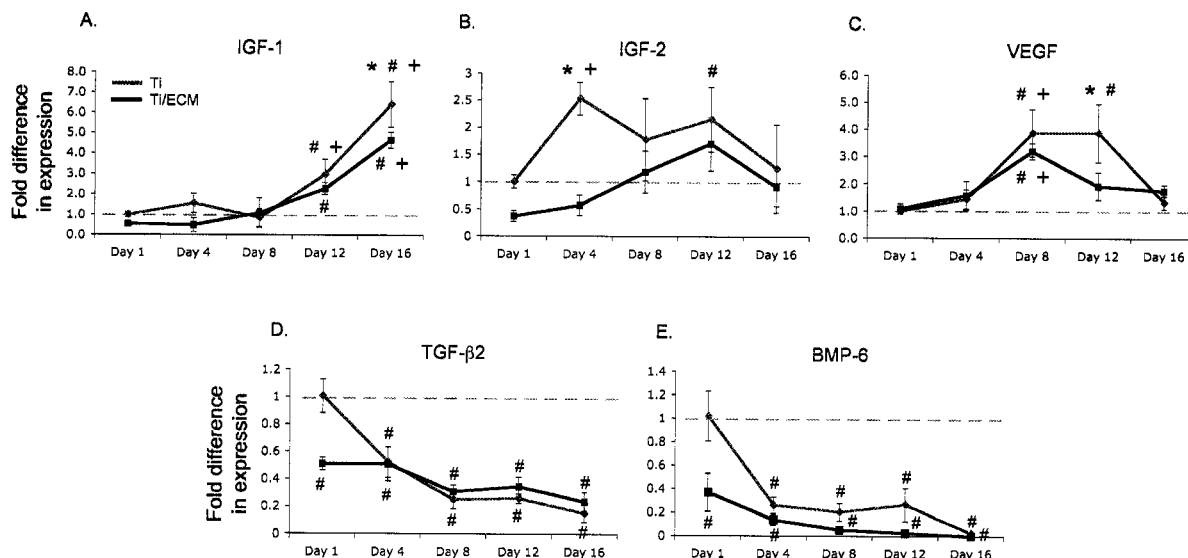
Figure 3-3

Gene expression profiles of growth factors that exhibited significant (A-C) upregulation or (D, E) downregulation compared to the baseline on both Ti and Ti/ECM constructs as determined by RT-PCR. The data represents fold difference in expression of four samples normalized to Ti day 1 samples. A * indicates a significant difference in expression level at the specified timpoint ($p < 0.05$); a # symbol indicates a significant difference in expression level with respect to the baseline ($p < 0.05$); a + symbol indicates a significant increase in expression level from the previous timepoint. The blue line represents the Ti group while the black line represents the Ti/ECM group and applies to all graphs. The dashed grey line indicates the baseline expression level.
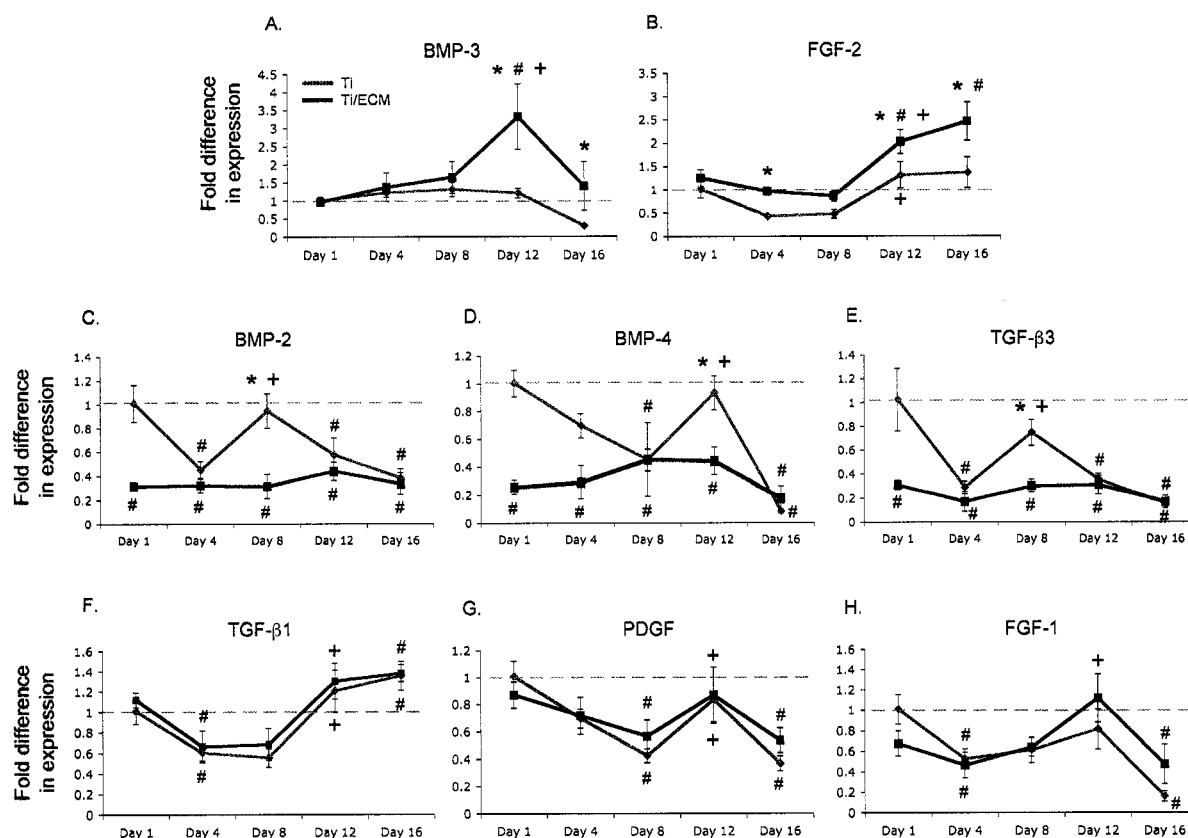
Figure 3-4

Gene expression profiles of growth factors that were upregulated (A, B), attenuated (C-E), or had no effect (F-H) by the extracellular matrix as determined by RT-PCR. The data represents fold difference in expression of four samples normalized to Ti day 1 samples. A * indicates a significant difference in expression level at the specified timpoint (p<0.05); a # symbol indicates a significant difference in expression level with respect to the baseline (p<0.05); a + symbol indicates a significant increase in expression level from the previous timepoint. The blue line represents the Ti group while the black line represents the Ti/ECM group and applies to all graphs. The dashed grey line indicates the baseline expression level.

Day 1   Day 4   Day 8   Day 12   Day 16
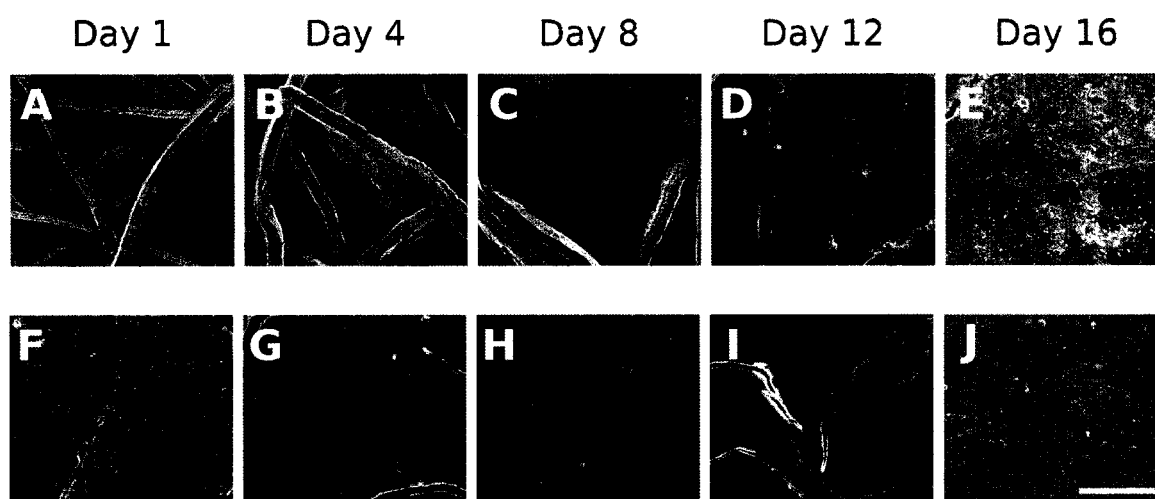
Figure 3-5

Representative scanning electron microscopy images of the top surfaces of Ti (A-E) and Ti/ECM (F-J) constructs at the timepoints indicated. The scale bar shown represents 100 μm and applies to all images.

Day 1   Day 4   Day 8   Day 12   Day 16
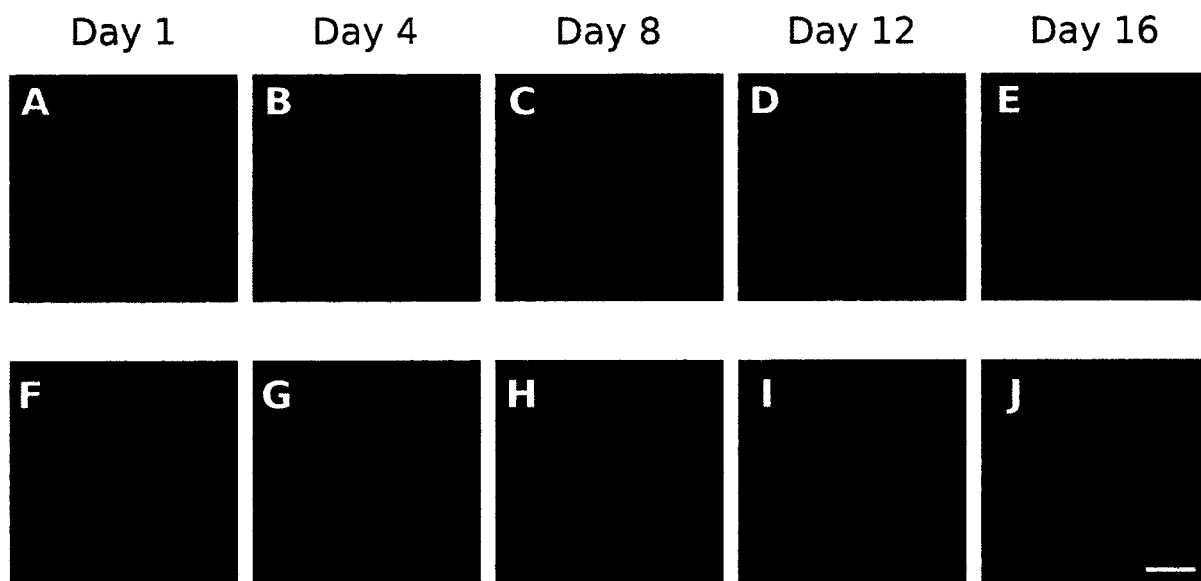
Figure 3-6

Representative laser scanning confocal images of the top surfaces of Ti (A-E) and Ti/ECM (F-J) constructs stained with calcein AM to visualize viable cells. The scale bar shown represents 200 μm and applies to all images.
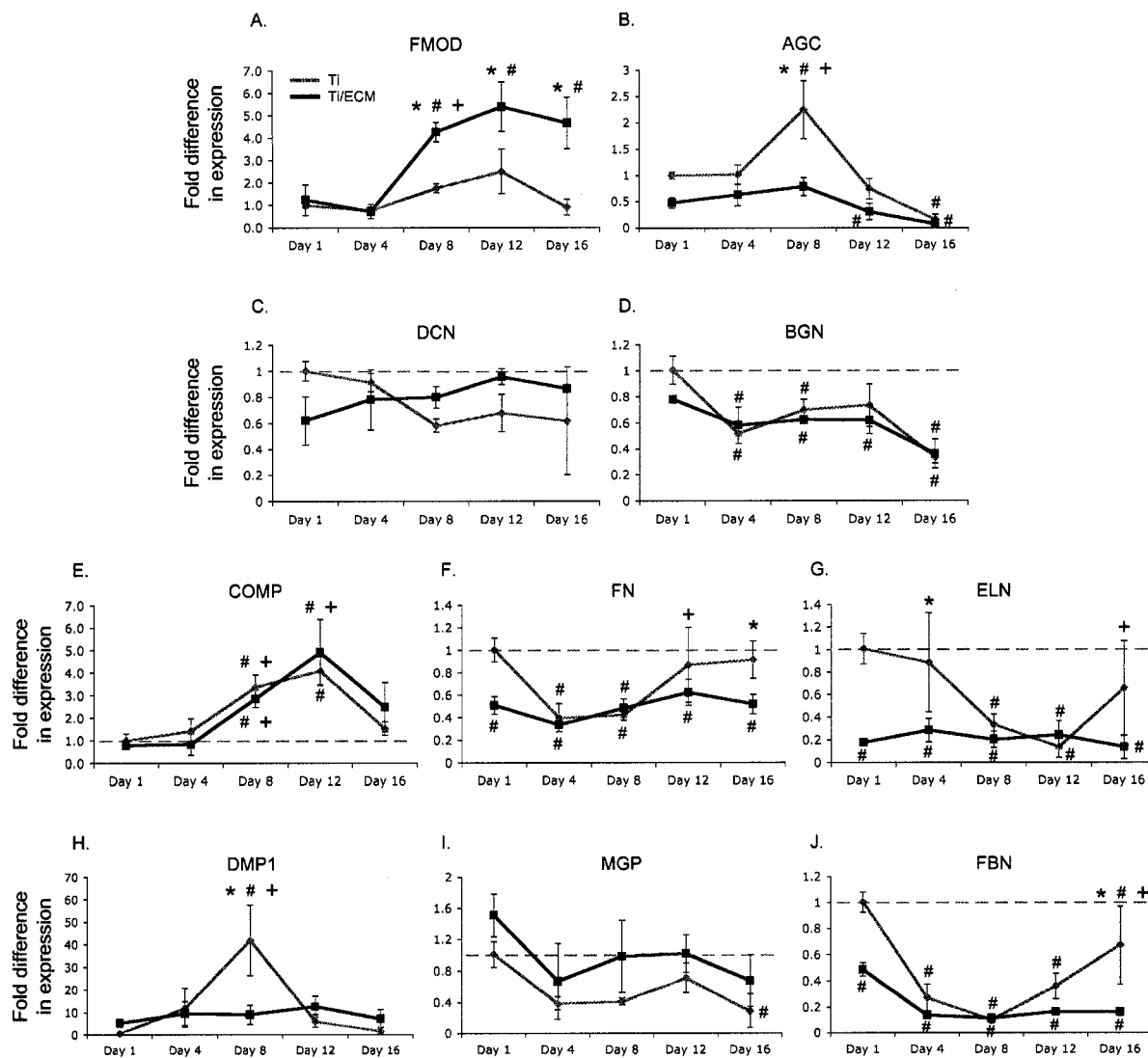
Figure 3-7

Gene expression profiles of extracellular matrix molecules (caption on following page)
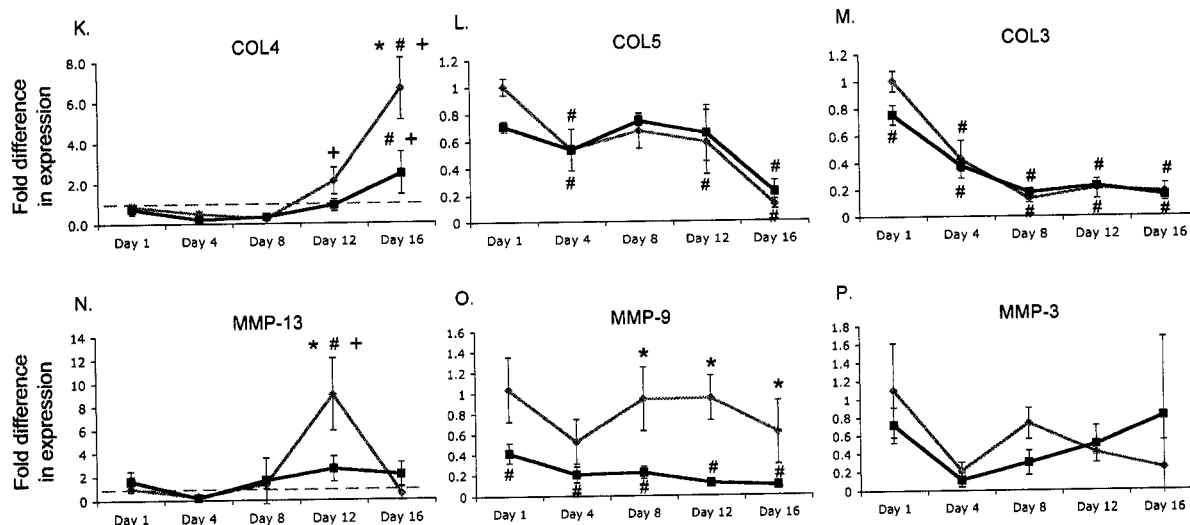
(continued from previous page)

Figure 3-7

Gene expression profiles of extracellular matrix molecules found in bone as determined by RT-PCR. The data represents the mean fold difference in expression of four samples normalized to Ti day 1 samples. The investigated componenets include proteoglycans (A-D), glycopproteins (E-J), collagens (K-M), and matrix metalloproteinases (N-P). A * indicates a significant difference in expression level at the specified timpoint (p<0.05); a # symbol indicates a significant difference in expression level with respect to the baseline (p<0.05); a + symbol indicates a significant increase in expression level from the previous timepoint. The blue line represents the Ti group while the black line represents the Ti/ECM group and applies to all graphs. The dashed grey line indicates the baseline expression level.

CHAPTER 4[*]

FLOW PERFUSION AND EXTRACELLULAR MATRIX ACT SYNERGISTICALLY TO ENHANCE MARROW STROMAL CELL OSTEOBLASTIC DIFFERENTIATION

Abstract

This study instituted a novel approach to bone tissue engineering by combining effects of mechanical stimulation in the form of fluid shear stresses and the presence of bone-like extracellular matrix (ECM) on osteodifferentiation. Rat marrow stromal cells (MSCs) harvested from bone marrow were cultured on titanium fiber mesh discs for 12 days in a flow perfusion system to generate constructs containing bone-like ECM. To observe osteodifferentiation and bone-like matrix deposition, these decellularized constructs and plain titanium fiber meshes were seeded with MSCs (Ti/ECM and Ti, respectively) and cultured while in the presence of fluid shear stresses and either with or without the osteogenic culture supplement dexamethasone. The calcium content, alkaline phosphatase activity, and osteopontin secretion were monitored as indicators of MSC differentiation. Ti/ECM constructs demonstrated a 75-fold increase in calcium content compared to their Ti counterparts after 16 days of culture. After 16 days, the presence of dexamethasone enhanced the effects of fluid shear stress and the bone-like ECM by increasing mineralization 50-fold for Ti/ECM constructs; even in the absence of dexamethasone, the Ti/ECM constructs exhibited approximately a 40-fold increase

---

in mineralization compared to their Ti counterparts. Additionally, denatured Ti/ECM* constructs demonstrated a 60-fold decrease in calcium content compared to Ti/ECM ones after 4 days of culture. These results indicate that the inherent osteoinductive potential of bone-like ECM along with fluid shear stresses synergistically enhance the osteodifferentiation of MSCs with profound implications on bone tissue engineering applications.

Introduction

Despite the innate ability of bone to heal, there are still approximately one million bone substitute operations performed annually in the United States alone [134]. Current treatments for osseous defects and anomalies include the use of autografts, allografts, and metallic implants [135]. However, the limited availability and donor site morbidity of autografts and issues with immune responses from allografts and metallic implants are drawbacks to these methods [136, 137]. The need for osteogenic bone substitutes has led to the development of many bone tissue engineering strategies. By combining different components of the tissue engineering paradigm (biomaterial scaffolds, cells, and bioactive molecules), the conditions of normal tissue development *in vivo* may be mimicked to recreate functional and structural tissues *in vitro* [138].

An ideal bone tissue engineering scaffold would be both osteoconductive and osteoinductive. Osteoconductivity refers to a scaffold's ability to support osteoblast and osteoprogenitor cell attachment and subsequent bone matrix deposition and formation [54, 137]. Inorganic compounds, such as calcium phosphates or hydroxyapatite crystals, are often incorporated into scaffolds with a low osteoconductivity resulting in increased cell attachment [54]. Osteoinductivity describes a scaffold that encourages osteogenic precursor cells to differentiate into mature bone-forming cells [139]. Many small fractures and defects heal due to the osteoinductivity of natural bone, which has led to investigations of demineralized bone as a potential bone tissue engineering scaffold [140]. However, in large bone

defects, the inherent osteoinductivity of bone may not be sufficient for adequate healing. Thus, a model scaffold would itself be capable of recruiting stem and osteoprogenitor cells to a bone healing site where they would eventually differentiate into ECM-secreting osteoblasts [139]. Other considerations for a tissue engineering scaffold include mechanical integrity, biodegradability, biocompatibility, and a porosity that would allow for bone tissue ingrowth [58].

Most tissue engineering scaffolds (i.e. ceramics, metals, polymers) are only osteoconductive [58, 141, 142]. One method to incorporate osteoinductive properties to a scaffold is through the inclusion of growth factors or cytokines specific to the desired tissue to be regenerated. Growth factors known to influence bone cells include transforming growth factors (TGFs) [24], insulin-like growth factors [25], bone morphogenetic proteins (BMPs) [26], fibroblast growth factors (FGFs), and platelet-derived growth factors [27]. These critical mediators of bone function regulate the phenotype of osteoblasts and other bone cells by binding to cell surface receptors which, in turn, activate cellular responses such as proliferation and differentiation [143].

Marrow stromal cells (MSCs) are multipotent cells found predominantly within the bone marrow and are undifferentiated but, when given the proper environmental cues, can potentially differentiate into various tissue types including but not limited to bone, cartilage, and adipose [8]. *In vivo,* osteodifferentiation is marked by sequential stages of cellular proliferation, bone extracellular matrix (ECM) maturation, and

matrix mineralization [6]. This progression is mediated by cell-growth factor, cell-cell, and cell-matrix interactions [144]. Mechanical strain and fluid shear stress have also been demonstrated to influence osteodifferentiation with load-induced fluid shear stress being shown to have greater effects [88, 145, 146]. *In vivo*, bone cells experience interstitial fluid shear stress upon mechanical loading of bone through fluid flow inside the canalicular-lacunar and trabecular spaces within bone tissue [90]. To accurately mimic the *in vivo* matrix architecture, cells should be cultured in a 3D environment with the appropriate mechanical stimulation.

Bioreactors provide a means to expose cells to dynamic culture conditions *in vitro* [77, 83]. An approach used previously in our group focuses on the use of fluid shear stresses generated by a flow perfusion bioreactor to influence osteodifferentiation of MSCs . We have shown that fluid flow not only mitigates nutrient transport limitations in 3D perfusion cultures of MSCs but also provides mechanical stimulation to seeded cells in the form of fluid shear stress resulting in increased depositions of mineralized matrix [91, 96]. Cellular constructs cultured in a flow perfusion bioreactor yielded a significant increase in matrix mineralization after 16 days as compared to those cultured statically when cultured in the presence of osteogenic supplements including dexamethasone, which has been shown to be a powerful promoter of osteodifferentiation [147]. Furthermore, flow perfusion culture in the absence of dexamethasone resulted in more mineralization than static culture in the presence of dexamethasone [22]. These results indicated that fluid shear stresses

can positively influence and enhance osteodifferentiation of MSCs on porous scaffolds.

In vivo, the ECM plays an important role in maintaining and mediating bone function. Several studies suggest that the 3D matrix structure and organization can influence the phenotypic behavior of cells [134, 148]. Native bone is a highly dynamic and complex system that consists predominately of a mineralized ECM secreted by osteoblasts [149]. The organic components of bone-like ECM are composed of 90% type I collagen while the remaining 10% consists of noncollagenous proteins [5, 150]. The ECM contains various osteoinductive factors as evidenced by bone formation in ectopic sites using demineralized bone [151]. Located throughout the bone matrix are a variety of glycoproteins, such as thrombospondin, fibronectin, vitronectin, and fibrillin, which help promote cellular attachment [5]. Mechanical signals are conveyed through these adhesion proteins to attached cells and cause changes in gene expression and phenotype [130]. Osteopontin and bone sialoprotein are other matrix glycoproteins also involved in the matrix mineralization processes [150]. To capitalize upon the beneficial properties of ECM, we have previously cultured MSCs on titanium scaffolds to generate bone-like ECM *in vitro.* The presence of this bone-like ECM resulted in significantly larger mineral deposition by MSCs over 16 days under static culture conditions as compared to constructs without pre-generated ECM [101]. These results suggested that the presence of the pre-generated bone-like ECM transformed the titanium scaffold from an osteoconductive to an osteoinductive construct.

In this work, we aimed to combine the beneficial properties of fluid shear stress with those of pre-generated ECM. To do so, MSCs were seeded onto either plain titanium or pre-generated ECM-containing titanium meshes and cultured in a flow perfusion bioreactor. A comparison of these constructs enabled us to examine the osteoinductive potential of an *in vitro* pre-generated ECM on osteoblast differentiation while in the presence of fluid shear stresses. Because plain titanium constructs and those containing pre-generated ECM have different pore sizes (the ECM fills the void volume of the plain Ti scaffold), fluid flow through each of these constructs will exert different shear stresses on the seeded cells. To separate the effects of the *in vitro* pre-generated ECM from those due to differences in shear stress, a group of constructs containing denatured pre-generated ECM were fabricated; doing so allowed for the effects of the pre-generated ECM to be measured directly. Finally, in order to elucidate its osteogenic effect, the 3D *in vitro* culture of such constructs was carried out either with or without dexamethasone in the culture media. Known markers of differentiation, including expression of alkaline phosphatase, secretion of osteopontin, and deposition of a calcified ECM were used as indicators of cell differentiation and mineralization. Our approach combines all three elements of the tissue engineering paradigm: marrow stromal cells capable of osteodifferentiation, titanium fiber mesh as an osteoconductive scaffold, and a pre-generated bone-like ECM as a source of bone cell differentiation supporting factors.

Materials and Methods

Scaffold Preparation

Titanium (Ti) fiber meshes (Bekaert N.V., Zwevegem, Belgium) with porosity of 86% and fiber diameter of 20 μm were die-punched into 8 mm diameter discs (thickness = 0.8 mm). Scaffolds were sterilized by autoclaving prior to use [91].

Rat Marrow Stromal Cell Isolation

Marrow stromal cells (MSCs) were harvested and pooled together from 10 male Wistar rats weighing 150-175 g, according to established protocols [101]. Cells were cultured in the presence of 10^{-8} M dexamethasone for 6 days in complete osteogenic media containing minimum essential media (alpha modification), 10 mM β-glycerophosphate, 50 mg/ml ascorbic acid, (all from Sigma, St. Louis, MO), and 10% (vol) fetal bovine serum (FBS) (Gemini Bio-Products, Woodland, CA). Cells were trypsinized on day 6, suspended in 10% (vol) dimethyl sulfoxide (Sigma, St. Louis, MO) in FBS, aliquoted in 1.5 ml cryovials, placed in a freezing canister overnight at -80 °C, and then transferred to liquid nitrogen until use. For constructs cultured without dexamethasone, all procedures were identical except dexamethasone was omitted from the media.

Experimental Design

To generate the bone-like ECM, plain titanium meshes were first seeded with MSCs and cultured in complete media under flow for a period of 12 days after which they were decellularized [101] and sterilized with ethylene oxide gas for 12 hours. To remove residual ethylene oxide, the meshes were subsequently aerated for at least

6 hours. Titanium constructs either with or without pre-generated ECM (Ti and Ti/ECM constructs, respectively) were pre-wet in PBS for 1 hour and then seeded with MSCs and cultured in a flow perfusion bioreactor for 4, 8, or 16 days. Additionally, denatured Ti/ECM constructs (Ti/ECM*) were obtained by exposing Ti/ECM constructs to heat; these Ti/ECM* constructs were subsequently seeded with MSCs and cultured in complete media under flow for 4 days. To study matrix mineralization in the absence of dexamethasone, Ti and Ti/ECM constructs were also seeded with MSCs and cultured in the absence of dexamethasone for 16 days; these groups are represented as Ti/- and Ti/ECM/- constructs.

Flow Perfusion Culture of MSCs on Ti Meshes

The flow perfusion culture system was set up as described in detail by Bancroft et al.[83]. Plain titanium fiber meshes were seeded with 250,000 MSCs in 200 μl of complete media to generate Ti constructs. After 2 days, the cassettes containing the seeded constructs were placed in the bioreactor. The operation of the bioreactor system was driven by a peristaltic pump set at a rate of 1 ml/min. The cells were cultured in complete media for 4, 8, or 16 days with a complete media exchange every 48 hrs. Each group consisted of 6 samples, including 1 for scanning electron microscopy (SEM) analysis. At the end of the culture period, all constructs were rinsed with PBS and stored in 1.5 ml distilled-deionized water at -20°C until further use.

Ti/ECM Construct Generation

Cryo-preserved MSCs were resuscitated in complete osteogenic media and subsequently cultured for 6 days. Titanium meshes were seeded as described above. The constructs were cultured for 12 days in the flow perfusion bioreactor in complete medium. At the end of the culture period, constructs were rinsed and stored in distilled-deionized water at -20°C.

To remove cellular components, the meshes were decellularized using three consecutive freeze-thaw cycles [152] resulting in constructs that have been shown to contain no cells [101]. The Ti/ECM constructs were allowed to air dry, sterilized with ethylene oxide, and then press-fit into flow system cassettes in a 6-well plate for further culture in the bioreactor as previously described. Preparation of Ti/ECM* constructs was performed in a similar manner except that, immediately after decellularization, the Ti/ECM meshes were placed in a 70°C water bath for 5 min.

Mercury Porosimetry

Scaffold pore size was measured using mercury porosimetry (Autoscan 500, Quantachrome Instruments, Boynton Beach, FL) as previously described [153]. Scaffolds were placed into the sample chamber, and the void space in the chamber was filled with mercury. The pressure was then increased at a rate of 0.01 psi/s until a total pressure of 50 psi was reached. Volume versus pressure data were converted to pore size using software supplied by the vendor (Quantachrome Autoscan, ver. 3.00). Measurements were made on 3 samples of each scaffold type.

Scanning Electron Microscopy Analysis

Samples were fixed in 2.5% (vol) glutaraldehyde for 2 hrs. The samples were cut in half for analysis of both the top and bottom; additionally, a cross-section was cut. All samples were dried, mounted on aluminium stages, sputter coated with gold, and examined with an FEI-XL 30 Environmental Scanning Electron Microscope; energy dispersive spectroscopy (EDAX, Mahwah, NJ) was performed in conjunction with the SEM imaging.

Biochemical Assays

The cellularity and alkaline phosphatase (ALP) enzyme activity of the constructs were determined as described previously [101]. Briefly, titanium constructs were sonicated for 10 min. The DNA of the supernatant was quantified using the PicoGreen assay (PicoGreen, Molecular Probes) and compared to DNA extracted from known numbers of MSCs. ALP enzyme activity of the constructs was measured using the supernatant and the Alkaline Phosphatase Assay from Sigma (St. Louis, MO). Calcium content of the constructs was determined using a calcium quantification assay obtained from Diagnostic Chemicals Limited (Charlottetown, PEI, Canada) as previously described [22]. After the DNA and ALP assays were performed, the constructs were placed in acetic acid (0.5 N) overnight to dissolve calcium. For all Ti/ECM and Ti/ECM* constructs, the calcium present in the initial decellularized construct (approximately 40 µg) was accounted for.

In order to determine the total collagen and glycosaminoglycan (GAG) content of the Ti/ECM constructs, constructs were first cut into fine pieces with scissors and then digested with proteinase K solution (1 mg/mL proteinase K, 10 µg/ml pepstatin A, and 185 µg/ml iodoacetamide) in phosphate-buffered EDTA (6.055 mg/ml Tris(hydroxymethyl aminomethane), 0.372 mg/ml EDTA, pH 7.6 adjusted by HCl) for 16 hours in a 56°C water bath. An aliquot of the solution after digestion was used to perform the dimethylmethylene blue dye assay to determine the GAG content in each construct as previously described [154]. Total collagen content was performed following a hydroxyproline assay of an aliquot of the digested samples. Briefly, 200 µl of the digested sample was hydrolyzed in 6M hydrochloric acid for 4 hours at 115°C. Samples were allowed to cool to room temperature and the HCl evaporated under nitrogen flow. The hydrolyzate was dissolved in 700 µl of ddH$_2$O and then a sample was mixed with chloramine-T solution and p-dimethylaminobenzaldehyde [155]. The absorbance was read using a plate reader at a wavelength of 570 nm. Collagen content was determined following a 1:10 ratio of hydroxyproline to collagen [156].

Osteopontin Assay

Osteopontin content of the constructs was measured using an ELISA kit against rat osteopontin available from Assay Designs (Ann Arbor, MI) as previously described [101]. Media samples were collected every 2 days during the culture period and stored at -20°C. Samples were run in duplicate and compared against rat osteopontin standards.

Statistical Analysis

Samples for DNA, ALP, and calcium assays were performed in triplicate and results reported as means ± standard deviation for 4 different scaffolds. Osteopontin secretion was determined from a media sample that represented a pool of six samples; the assay for osteopontin was performed in duplicate. A 2 factor repeated measures ANOVA was performed prior to making multiple comparisons between Ti, Ti/ECM, Ti/-, and Ti/ECM/- constructs using the Tukey procedure at a significance level of 95%. A one way ANOVA was performed prior to comparing means between Ti, Ti/ECM, and Ti/ECM* constructs using the Tukey procedure at a significance level of 95%. Statistical analysis of total collagen and GAG content was performed similarly for 3 different scaffolds.

Results and Discussion

This study investigated the osteoinductive capacity of an *in vitro* pre-generated ECM on the proliferation and differentiation of marrow stromal cells seeded on 3D titanium fiber mesh scaffolds and cultured in a flow perfusion bioreactor. The pre-generated ECM used in this study was secreted by MSCs over a 12 day culture period to allow for sufficient matrix deposition; compositional analysis of the matrix indicated the presence of GAGs and collagen (as determined by biochemical analysis of the Ti/ECM constructs-see Figure 5). The specific questions we wanted to answer were: 1. What effects do the combination of bone-like ECM and flow have on

osteodifferentiation? 2. How is this effect different in the presence and absence of osteogenic culture supplement dexamethasone?

Since the endpoint of osteoblast phenotypic expression is indicated by the production of a calcified, mineralized matrix [157], we measured the calcium content in the constructs as an indicator of osteodifferentiation. The measured calcium content increased with time for both Ti and Ti/ECM constructs (Figure 1). Ti constructs, when cultured under flow perfusion in the presence of dexamethasone for 16 days, contained approximately 50 μg of calcium. In contrast, the Ti/ECM constructs yielded 75 times more calcium after the same amount of time, approximately 3800 μg. After only 4 days of culture, the calcium content of the Ti/ECM constructs was already approximately 1600 μg, whereas only 2 μg were observed in Ti constructs.

The substantial increase in calcium content after only 4 days in Ti/ECM constructs could be attributed to two things: (1) the presence of the ECM in the Ti/ECM constructs and (2) differences in the shear stress exerted on the cells in these constructs compared to plain Ti ones. A previously developed cylindrical pore model showed that the fluid shear stress exerted on cells in a scaffold is dependent on the pore size of the construct: for a given flow rate, MSCs on constructs with smaller pore sizes experience larger shear stress, and subsequently demonstrate greater matrix mineralization [153]. Mercury porosimetry measurements confirmed a difference in the pore sizes of Ti and Ti/ECM scaffolds (65.3 ± 3.0 μm versus 29.8 ±

7.1 μm, respectively) which could explain the increased mineralization in Ti/ECM scaffolds.

To separate the effects of the pore size differences between the Ti and Ti/ECM groups from the impact of the ECM, some Ti/ECM scaffolds were denatured by heat treatment in order to deactivate the growth factors contained within the *in vitro* generated ECM. These Ti/ECM* constructs had an average pore size that was not significantly different from Ti/ECM constructs (29.8 ± 7.1 versus 25.7 ± 4.6 μm, respectively). Nevertheless, Ti/ECM* constructs demonstrated significantly less calcium than Ti/ECM constructs after 4 days of culture (27 μg and 1600 μg, respectively) (Figure 2A). The Ti/ECM* constructs had greater cellularity than Ti and Ti/ECM constructs indicating that the cells were able to attach and proliferate on these scaffolds (data not shown). Therefore, we hypothesize that the increased matrix mineralization observed on Ti/ECM constructs compared to Ti/ECM* is an indicator of enhanced osteodifferentiation of MSCs on the Ti/ECM constructs due to bioactive growth factors present in the pre-generated matrix; in the heat treated Ti/ECM* constructs, these growth factors were not active and therefore less osteodifferentiation was observed.

The role of dexamethasone in these substantial increases of mineral content was examined by comparing calcium data for the Ti/ECM/- and Ti/- constructs in flow perfusion to those constructs cultured in the presence of dexamethasone (Ti/ECM and Ti). After 16 days of culture, Ti/ECM/- constructs contained about 75 μg of

calcium, and the Ti/- constructs had approximately 1 μg of Ca (Figure 2B). Because the mineralized matrix deposition in both ECM containing groups (Ti/ECM and Ti/ECM/-) was significantly higher than their counterparts (Ti and Ti/-), there was a stimulatory effect of the pre-generated ECM on MSCs. Furthermore, even in the absence of dexamethasone, the calcium content in the Ti/ECM/- constructs after 16 days of culture was greater than in the Ti constructs, lending further credence to the osteoinductive capability of the bone-like ECM.

Furthermore, the results of this study were compared to a previous study in which Ti/ECM constructs were cultured statically [101] in order to isolate the effects of the pre-generated ECM from those of flow perfusion culture. The calcium content of the Ti/ECM constructs in this study demonstrated a 5-fold increase relative to corresponding static Ti/ECM constructs of the previous study. For plain Ti constructs, only a 2-fold increase was observed for flow culture as compared to static culture. These results indicate that the combination of the pre-generated bone-like ECM and flow perfusion culture in the presence of dexamethasone synergistically impact the differentiation of MSCs.

The calcium data was corroborated by examining the constructs using SEM and EDAX. Prior to *in vitro* culture, cells were seeded on the top of the scaffolds, which resulted in more cells and ECM at the top of the scaffolds initially (Figure 6). Images of the tops and bottoms of Ti and Ti/ECM constructs were obtained at 0, 4, 8, and 16 days to follow the evolution of the ECM deposition and matrix mineralization

throughout the construct. Extensive mineralization (composed of calcium and phosphorous according to EDAX analysis) was observed at the top surfaces of Ti/ECM scaffolds after 4, 8, and 16 days of culture; by day 16, the titanium fibers were encased in ECM and no longer visible on either side of the construct.

Additionally, cross-sections of the constructs were cut and analyzed by SEM to examine the distribution of ECM throughout the constructs. Figure 3 shows SEM images of a Ti construct after 16 days of culture (Figure 3A), a Ti/ECM construct after 4 days of culture (Figure 3B), and a Ti/ECM construct after 16 days of culture (Figure 3C). After 16 days of flow culture, it is evident that ECM is distributed throughout Ti constructs; however, void spaces are still visible and little mineralization is observed. In contrast, there are few open spaces in the Ti/ECM constructs after the same amount of time due to the presence of a substantial amount of mineralized matrix (Figure 3C). Furthermore, a direct comparison of a Ti construct cultured for 16 days (Figure 3A) and a Ti/ECM construct cultured for 4 days (Figure 3B) provides a qualitative appreciation for the impact of pre-existing ECM. (The Ti/ECM construct is pre-generated with a 12 day culture period, so the total *in vitro* culture period under flow perfusion is 16 days for both cases.) These results indicated that the presence of ECM and flow leads to enhanced mineralization and more uniform matrix distribution.

Prior to matrix mineralization, osteodifferentiation is marked by sequential stages of cellular proliferation and bone ECM maturation [6]. As a measure of proliferation,

the cellularities of the Ti and Ti/ECM constructs were measured (Figure 7). In both groups, the cellularities exhibited a peak at day 8 accompanied by a fall by day 16. The decrease in cellularity of constructs between days 8 and 16 can be attributed to the fact that higher matrix deposition and mineralization with time cause cells to become encased within the matrix and, hence, not detected by the DNA assay. Additionally, the Ti/ECM constructs had significantly lower cellularities at days 8 and 16 compared to Ti constructs, which could be an indication of poor cell proliferation or cell death in the interior of these scaffolds. However, the presence of extensive mineralized matrix indirectly suggests that the cells were viable and continued to deposit matrix. An alternative explanation is that since Ti/ECM constructs contain more matrix, the lower cell numbers could be attributed to more cells being encased. As suggested by the calcium data, we hypothesize that MSCs seeded on Ti/ECM constructs interacted with the pre-generated ECM and began to differentiate down the osteoblastic lineage.

This theory is further supported by the measurement of changes in the expression of osteoblastic markers. Specifically, ALP expression is known to peak following the end of the proliferative stage and before matrix maturation during osteoblastic differentiation [14]. For both Ti and Ti/ECM constructs, there was an increase and then decrease in ALP activity, with a peak occurring between 4 and 16 days of culture, suggesting osteodifferentiation was occurring (Figure 4). Additionally, at each time point, the ALP activity is significantly higher for the Ti/ECM constructs as compared to the Ti constructs. For example, at day 8 the ALP activity of the Ti/ECM

constructs is approximately 3-fold higher than the Ti constructs. The increased ALP activity in the Ti/ECM constructs indicates that the presence of the bone-like ECM enhances MSC differentiation towards osteoblast-like cells.

In accordance with the ALP activity, we expected the presence of pre-generated bone-like ECM to cause the cells to secrete more osteopontin. Our results, however, demonstrate higher cumulative osteopontin secretions in the Ti constructs as compared to Ti/ECM after 7 days of culture (Figure 8). In light of the ALP activity of the Ti/ECM constructs, it is likely that osteopontin secretion is underestimated for these samples. We attribute this underestimation to the fact that osteopontin is a calcium-binding protein and will therefore be sequestered within the mineralized matrix of the Ti/ECM constructs [101]. Additionally, the mineralized matrix will prevent the physical release of osteopontin.

The potential implications of this study on tissue engineering applications are profound. This approach provides a means to mimic the *in vivo* extracellular environment using *in vitro* culture. Typical bone tissue engineering scaffolds, such as collagen type I [56], ceramics [141], and demineralized bone [123] contain only the organic or inorganic component of bone and are not representative of native ECM. Composite scaffolds consisting of both phases of bone may represent the overall composition of bone but do not accurately mimic the complexities of bone ECM. Furthermore, there are also considerable limitations with the ability to incorporate multiple bioactive molecules in an optimal configuration for development

of bone. Our strategy for bone tissue engineering is to incorporate *in vitro* pre-generated ECM into a scaffold in order to capitalize on its inherent benefits. The pre-generated ECM in this study contained about 40 µg of calcium. The presence of calcium-phosphate within the matrix alters the chemical composition and surface roughness of the titanium fiber mesh, which can affect the attachment of osteoblast-like cells [158] and adsorption of cytokines and growth factors [35, 159, 160]. In addition to calcium, we have shown previously that ECM generated using a flow perfusion bioreactor contains bone signaling molecules, such as BMP-2, FGF-2, vascular endothelial growth factor, and TGF-β1 [161]. Although the effects of decellularization on this pre-generated ECM and the contained biomolecules are unknown, the enhanced matrix mineralization observed in Ti/ECM constructs as compared to plain Ti indicates that the ECM retains its osteoinductive nature.

A construct incorporating this pre-generated ECM could thus be implanted into a defect site, where its osteoinductive properties would result in the recruitment of stem and osteoprogenitor cells and adsorption of bioactive molecules within the *in vivo* environment leading to bone repair and regeneration. Alternatively, the constructs containing pre-generated ECM could be re-seeded with autologous MSCs and further cultured *in vitro* prior to implantation with two beneficial effects. First, the existing pre-generated ECM contains bioactive molecules, which provide signaling cues to direct and enhance MSC differentiation. Second, the *in vitro* 3D flow culture of the Ti/ECM constructs after re-seeding leads to an improved distribution of the mineralized matrix throughout the porosity of the scaffolds. This

improved distribution is particularly advantageous for tissue engineering applications; an ideal implant would be able interact with its 3D environment, rather than in a restricted 2D interface.

Conclusions

This study demonstrated the synergistic effect of *in vitro* pre-generated extracellular matrix and fluid flow on the proliferation and differentiation of marrow stromal cells seeded on titanium fiber mesh and cultured in a flow perfusion bioreactor with dexamethasone. The presence of the pre-generated ECM yielded a significant increase in the amount of mineralized matrix deposited in Ti/ECM constructs as compared to denatured Ti/ECM* constructs demonstrating the osteoinductive capability of the ECM. In addition, Ti/ECM/- constructs also demonstrated significantly higher calcium content than the Ti/- constructs indicating that, even in the absence of dexamethasone, the ECM induces osteodifferentiation.

In constructs cultured with dexamethasone, after 16 days of flow culture, mineralized matrix was observed throughout the Ti/ECM constructs. Additionally, an increase in ALP activity of the cells in Ti/ECM constructs was observed. Both ALP and calcium content are indicative of increased osteodifferentiation indicating that Ti/ECM constructs have increased osteodifferentiation compared to Ti constructs. Also the mineral content in the Ti/ECM constructs cultured under flow perfusion was five-fold larger than measured previously for Ti/ECM constructs cultured statically, indicating a synergistic effect between the bone-like ECM and fluid flow. These results

highlight the potential of pre-generated bone-like ECM as a viable scaffold for tissue engineering applications.

Acknowledgements
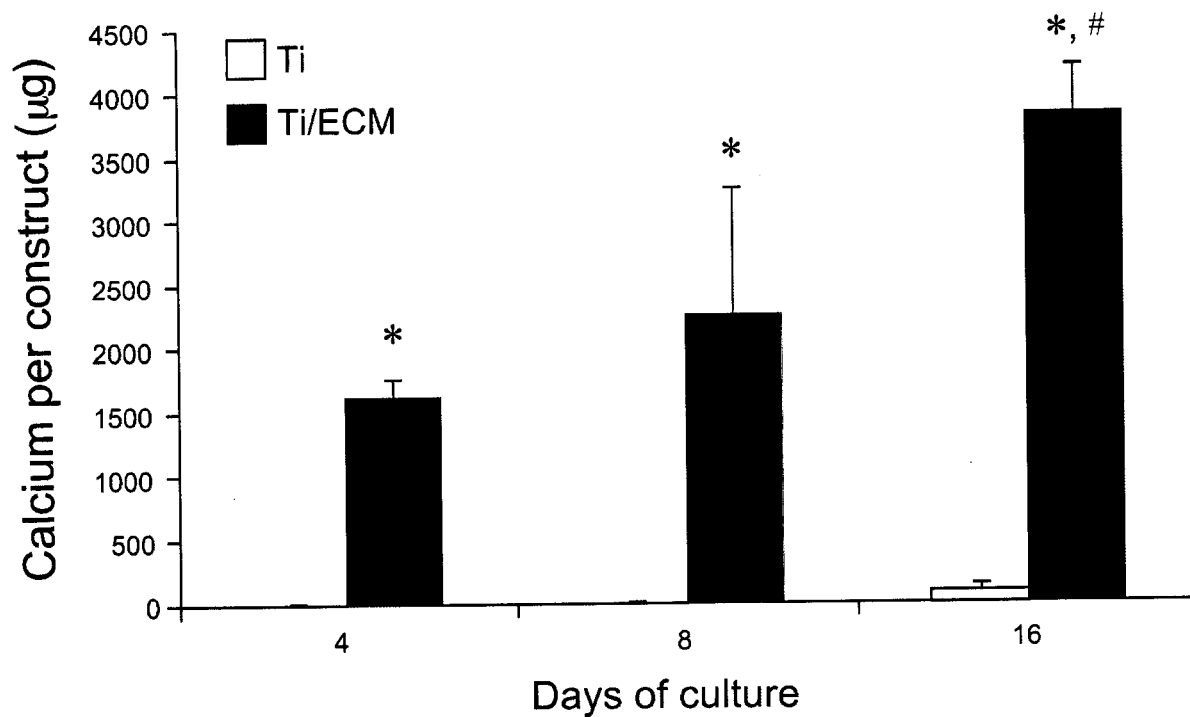
Figure 4-1

The calcium content of Ti and Ti/ECM constructs cultured in the flow perfusion bioreactor after 4, 8, and 16 days of culture. The data represent means of 4 samples with the error bars representing the standard deviations. Statistical differences ($p < 0.05$) between Ti and Ti/ECM constructs are indicated with a *; # designates a statistical difference ($p < 0.05$) between all other data points.
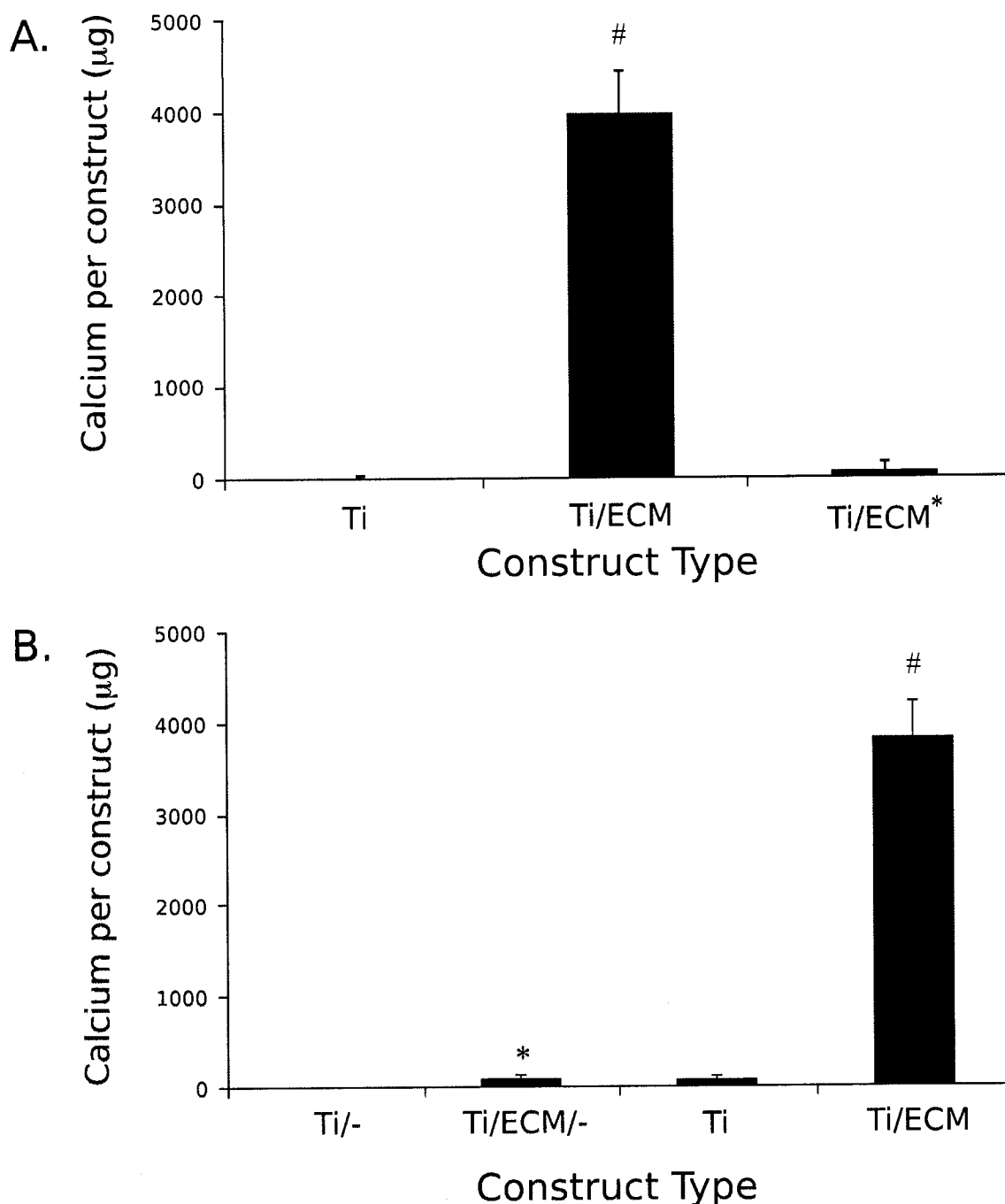
Figure 4-2

Calcium content of constructs cultured in the flow perfusion bioreactor. (A) The calcium content of Ti, Ti/ECM, and Ti/ECM* constructs after 4 days of culture. (B) The calcium content of Ti and Ti/ECM constructs cultured in the presence and absence (-) of dexamethasone after 16 days. The data represent means of 4 samples with the error bars representing the standard deviations. Statistical differences ($p < 0.05$) between constructs are indicated with a *; # designates a statistical difference ($p < 0.05$) between all other data points.
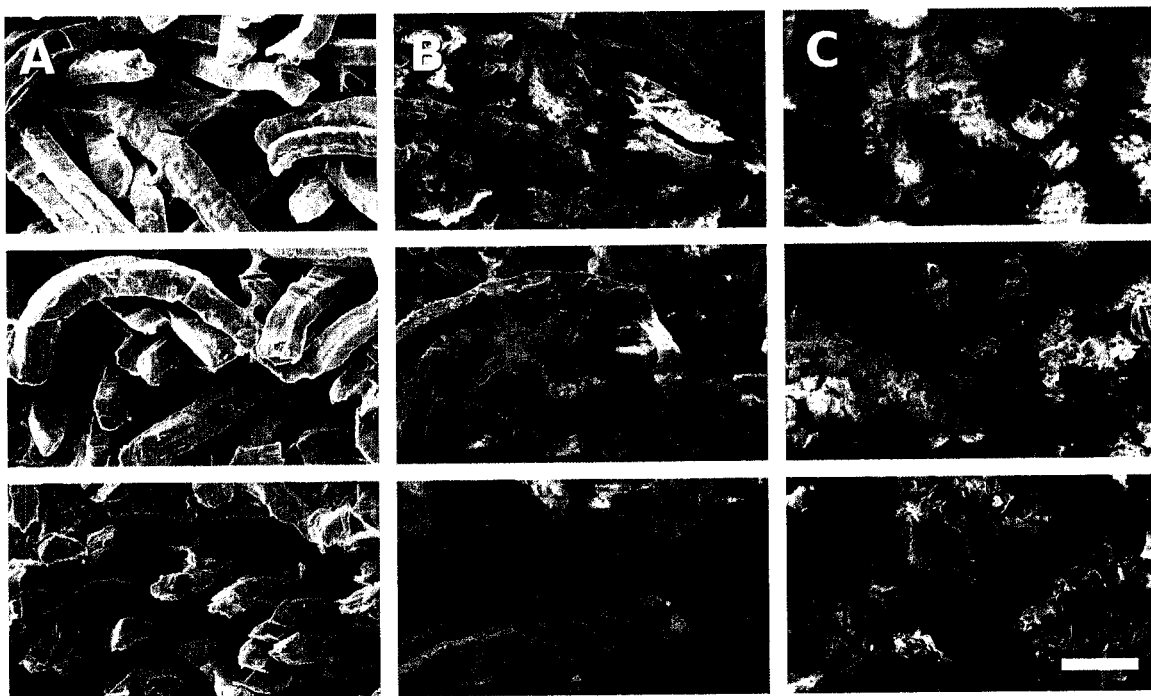
Figure 4-3

SEM images obtained from the cross-sections of constructs cultured *in vitro* in a flow perfusion bioreactor. Each image consists of 3 panels: the top ones are taken 100 mm from the top of the construct, the middle one is taken at the middle of the construct, and the bottom one is taken 100 μm from the bottom surface. These images show the plain Ti construct after 16 days of culture (A), the Ti/ECM construct after 4 days of culture (B), and the Ti/ECM construct after 16 days of culture (C). The scale bar shown applies to all SEM images and is equal to 50 micrometers.
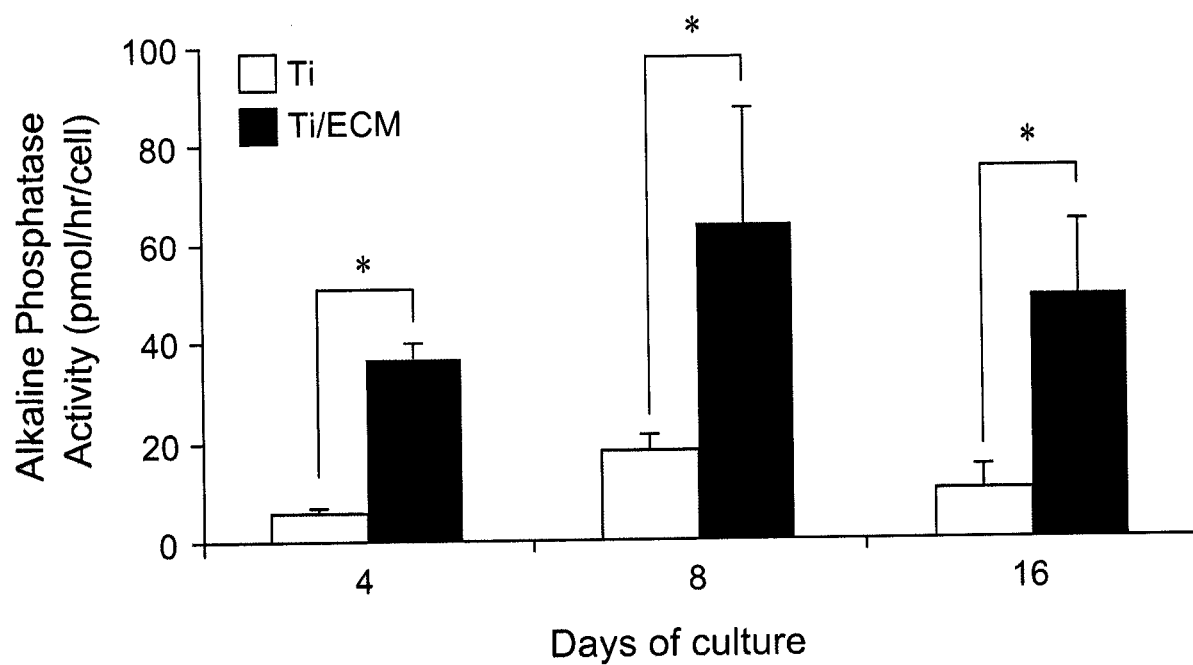
Figure 4-4

ALP activity of Ti and Ti/ECM constructs after 4, 8, or 16 days of culture under flow perfusion. The data represent means of 4 samples with the error bars representing the standard deviations. Statistical differences ($p < 0.05$) between Ti and Ti/ECM constructs are indicated with a *.
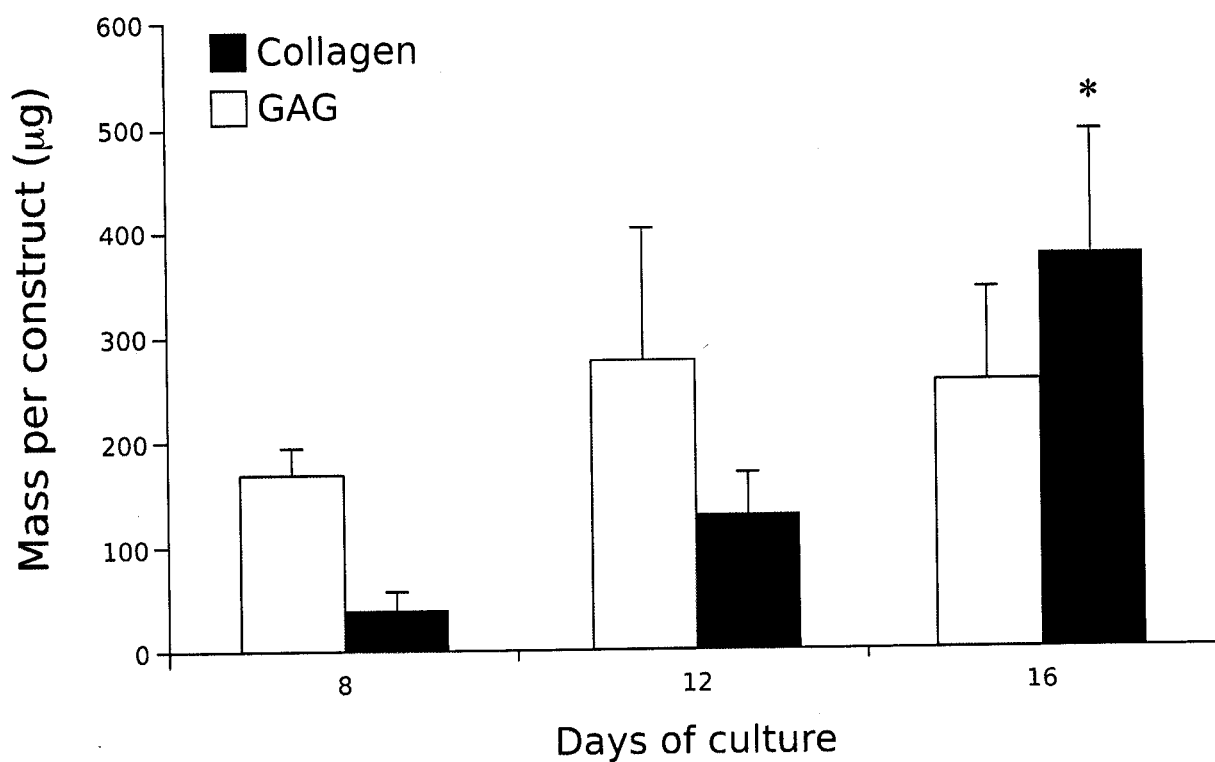
Figure 4-5

Glycosaminoglycan and collagen content of extracellular matrix in Ti/ECM constructs generated by marrow stromal cells cultured in the bioreactor for 8, 12, and 16 days. A * indicates statistical significance ($p < 0.05$) compared to day 8 sample.
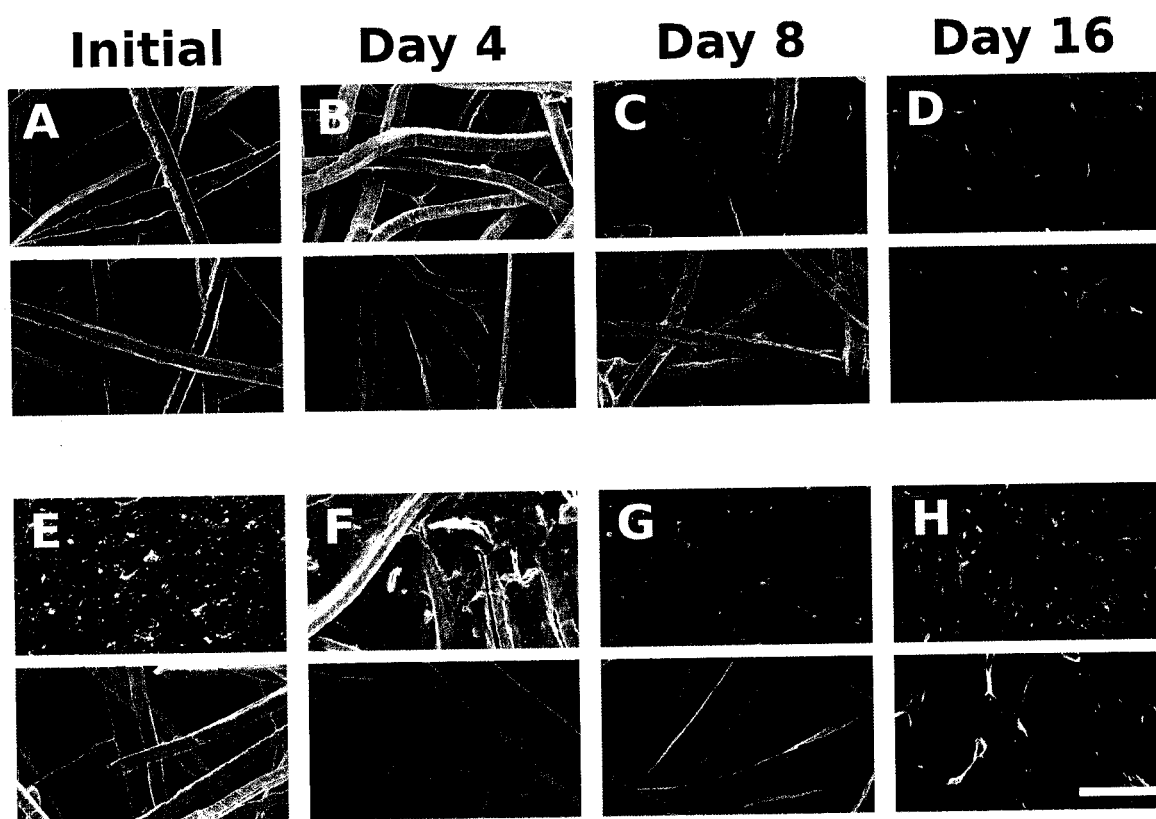
Figure 4-6

Scanning electron microscope images of the top and bottom of constructs after *in vitro* culture in a flow perfusion bioreactor. The upper panels of each image (A–H) represent the top of the construct as placed in the bioreactor. These images show the plain Ti construct (A) and plain Ti constructs seeded with marrow stromal cells (MSCs) after 4, 8, and 16 days (B–D). The decellularized Ti/ECM construct is shown in E. Ti/ECM constructs were reseeded with fresh MSCs and cultured *in vitro* for 4, 8, and 16 days (F–H). (Scale bar, 100 μm applies to all SEM images).
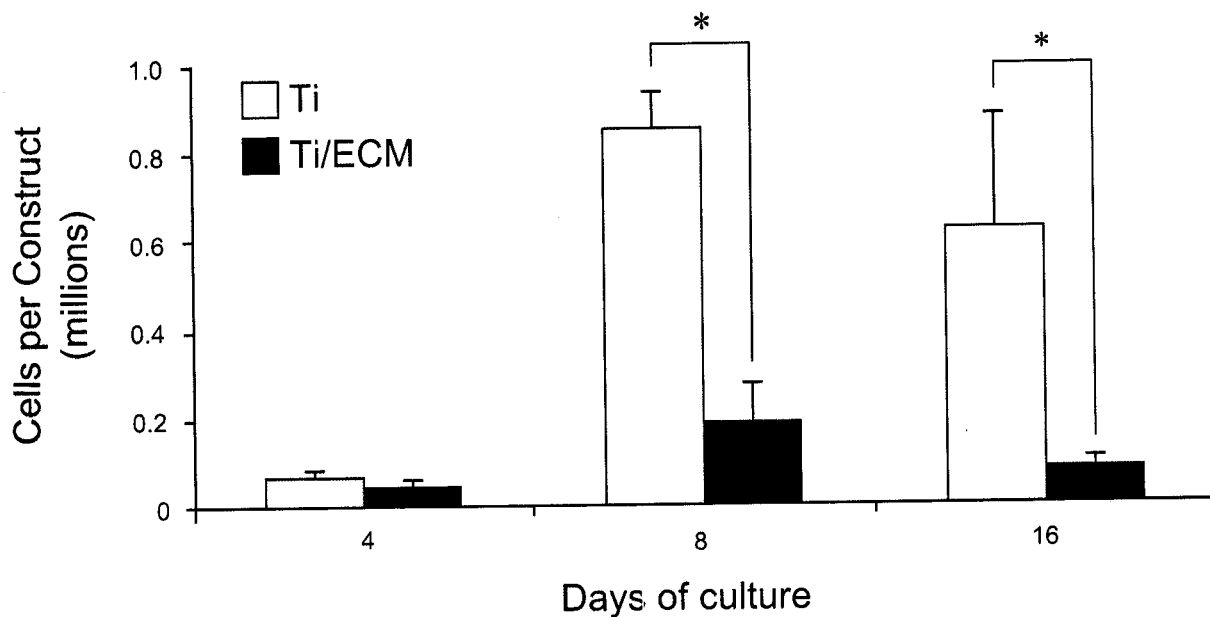
Figure 4-7

Cellularity of Ti and Ti/ECM constructs after 4, 8, or 16 days of culture under flow perfusion. The data represent means of four samples with the error bars representing the standard deviations. Statistical differences ($p < 0.05$) between Ti and Ti/ECM constructs are indicated with an *.
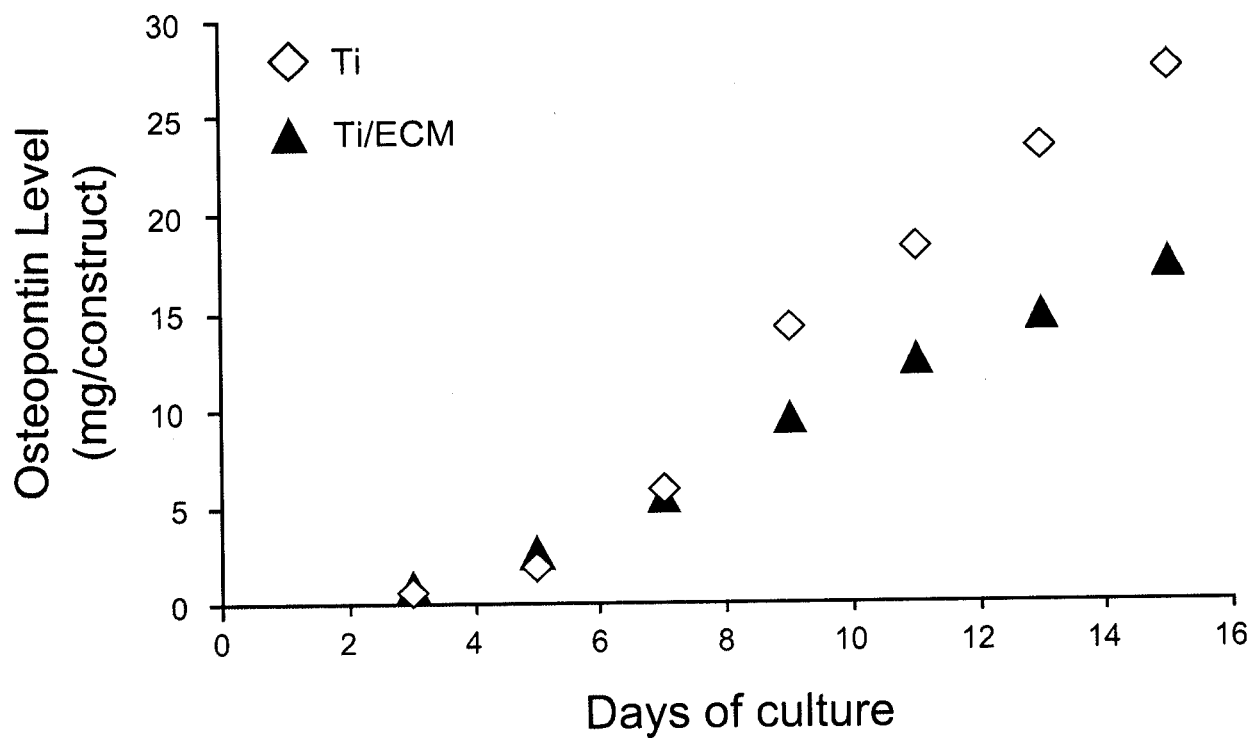
Figure 4-8

Cumulative osteopontin levels of media samples from Ti and Ti/ECM constructs during 16 days of culture under flow perfusion. The individual data points represent secretion levels of media samples pooled from six constructs.

CHAPTER 5[*]

ANALYSIS OF THE OSTEOINDUCTIVE CAPACITY AND ANGIOGENICITY OF AN *IN VITRO* GENERATED EXTRACELLULAR MATRIX

Abstract

In this study, the osteoinductive potential of an *in vitro* generated extracellular matrix (ECM) deposited by marrow stromal cells seeded onto titanium fiber mesh scaffolds and cultured in a flow perfusion bioreactor was investigated. Culture periods of 8, 12, and 16 days were selected to allow for different amounts of ECM deposition by the cells as well as ECM with varying degrees of maturity (Ti/ECM/d8, Ti/ECM/d12, and Ti/ECM/d16, respectively). These ECM-containing constructs were implanted intramuscularly in a rat animal model. After 56 days, histologic analysis of retrieved constructs revealed no bone formation in any of the implants. Surrounding many of the implants was a fibrous capsule, which was often interspersed with fat cells. Within the pore spaces, the predominant tissue response was the presence of blood vessels and young fibroblasts or fat cells. The number of blood vessels on a per area basis calculated from a histomorphometric analysis increased as a function of the amount of ECM within the implanted constructs, with a significant difference between Ti/ECM/d16 and plain Ti constructs. These results indicate that although an *in vitro* generated ECM alone may not induce bone formation at an ectopic site, its use may enhance the vascularization of implanted constructs.

Introduction

Osteoinductivity, or the ability of a material to induce stem cells to differentiate into osteoprogenitor and bone-forming cells in ectopic sites, is desirable for bone graft substitutes. Such a material would not only aid in osteogenesis but may facilitate and accelerate bone healing in skeletal defects [162]. In addition to being osteoinductive, an ideal graft material should also be osteogenic (containing living cells capable of differentiation into bone-forming cells or osteoblasts) and osteoconductive (supporting bone formation onto its surface). Autologous tissue, because it contains viable cells, extracellular matrix (ECM) elements, and bioactive growth factors, possesses all three characteristics and is currently the gold standard for treating skeletal defects [163]. However, the donor site morbidity associated with obtaining autologous tissue is a major drawback and has prompted investigation of alternative treatment options.

An acellular alternative to autologous tissue that is widely used as an osteoinductive bone graft substitute is demineralized bone matrix (DBM). DBM is bone that has been processed (usually with acid) to remove the mineral content, leaving behind growth factors, non-collagenous proteins, and collagen [164]. Although considered safe for clinical use, the efficacy of DBM on bone formation has been variable; this inconsistency has been attributed to the variable amounts of growth factors found between lots or batches of commercially available DBM [165]. The successful application of DBM can also be dependent on the surgical model and the carrier that is used to deliver the DBM to the defect site [164, 166].

Both autologous tissue and DBM contain components of native bone ECM. The ECM environment is a dynamic milieu where cell-cell and cell-matrix signaling interactions regulate cellular activity [167, 168]. In addition to providing a physical support structure for adherent cells, the ECM can also sequester growth factors resulting in localized reservoirs that are released when needed [169]. Indeed, the osteoinductive nature of autologous tissue and DBM has been attributed to the presence of these growth factors, primarily bone morphogenetic proteins (BMPs). These proteins have been found to be such potent osteoinductive factors, that new osseous tissue formation is observed following injection into muscle tissue [164, 170]. While a scaffold alone can support the attachment and proliferation of cells, it often lacks the ability to induce a desired response from cells. The bone-forming capabilities of synthetic scaffolds can be improved prior to implantation in defect sites by seeding the scaffolds with osteogenic cells and/or by loading them with bone-inductive growth factors [171]. In this approach, the seeded cells would support bone formation, and the growth factors would enhance bone formation by the host's own cells.

We have recently investigated an approach to produce tissue engineering constructs whereby an *in vitro* generated bone-like ECM is secreted by marrow stromal cells (MSCs) onto a synthetic scaffold. This ECM was generated either by using static culture or by using dynamic culture in the form of a flow perfusion bioreactor [101, 172]. When seeded with fresh MSCs *in vitro*, this ECM (containing collagen, glycosaminoglycans, and mineralized matrix) was shown to enhance and accelerate

MSC osteoblastic differentiation in the presence of osteogenic cell culture supplements and especially dexamethasone, as indicated by significant increases in deposited calcium [101, 172]. Using immunohistochemistry, growth factors, such as BMP-2, transforming growth factor-β1 vascular endothelial growth factor, insulin-like growth factor-2, and basic fibroblast growth factor, were found to be present in an *in vitro* generated ECM produced by rat MSCs cultured in a bioreactor [161]. Previous studies have demonstrated that the bioactivity of these factors influences bone formation and remodeling *in vivo* [173]. Consequently, the enhanced osteoblastic differentiation of freshly seeded MSCs *in vitro* was attributed in part to the presence of these growth factors within the ECM.

Based on these results *in vitro*, we sought to investigate the osteoinductive potential of this *in vitro* generated ECM. The overall objective of this study was to answer the following questions: First, can an *in vitro* generated ECM alone (i.e., without a cellular component) induce bone formation in an ectopic site; second, is there an angiogenic response to the *in vitro* generated ECM?; third, does the physical presence of ECM impede the infiltration of tissue within the pore spaces of the implant?; and finally, does the *in vitro* culture period used to generate the ECM have an influence on the above events? To determine the answers to these questions, rat MSCs were seeded onto titanium fiber mesh scaffolds and cultured in a flow perfusion bioreactor for different periods of time to allow for ECM deposition. These constructs were subsequently decellularized and implanted intramuscularly in a rat animal model to determine their osteoinductive capacity and angiogenicity.

Materials and Methods

Scaffold Preparation

Titanium (Ti) fiber meshes (Bekaert N.V., Zwevegem, Belgium) with porosity of 86%, a thickness of 0.8 mm, and fiber diameters of 20 μm were punched into 6 mm diameter discs using a die punch. Prior to cell culture use, the scaffolds were sterilized by autoclaving.

Rat Marrow Stromal Cell Isolation

Marrow stromal cells (MSCs) were harvested from 7-8 week old male Fischer 344 rats (Harlan, Indianapolis, IN) weighing 140-160 g according to established protocols [174]. Cells were cultured in the presence of 10^{-8} M dexamethasone for 6 days in complete osteogenic media containing minimum essential media (alpha modification), gentamicin (1 ml/l of media), amphotericin-B (1.25 mg/ml), 10 mM β-glycerophosphate, 50 mg/ml ascorbic acid, (all from Sigma, St. Louis, MO), and 10 vol% fetal bovine serum (FBS) (Gemini Bio-Products, West Sacramento, CA). Cells were trypsinized (0.25% trypsin/EDTA, Sigma, St. Louis, MO) on day 6, suspended in 10 vol% dimethyl sulfoxide (Sigma, St. Louis, MO) in FBS, aliquoted in 1.5 ml cryovials, placed in a freezing canister overnight at -80 °C, and then transferred to liquid nitrogen for storage.

Ti/ECM Construct Generation

For *in vitro* ECM generation, the cells frozen in liquid nitrogen were thawed and expanded in tissue culture flasks with osteogenic media until confluent. Cells were

then trypsinized and seeded onto Ti scaffolds that were press-fit into poly(methyl methacrylate) seeding cassettes designed for use in a flow perfusion bioreactor as described in detail by Bancroft et al. [83]. Plain Ti fiber meshes were seeded with 140,000 MSCs in 200 µl of complete media and cultured in the bioreactor for either 8, 12, or 16 days to generate constructs with different amounts of ECM as well as ECM with differing stages of maturity. Fluid flow through the bioreactor was driven by a peristaltic pump operating at a rate of 0.56 ml/min. The seeding density and flow rate in this study were selected based on a previous *in vitro* study [172]; however, the seeding density and flow rate were scaled to account for differences in scaffold diameters (8 mm in the previous study and 6 mm in the current study). Scaling was done such that the overall seeding density and volumetric flow rate were identical to the previous study. Complete media exchanges were performed every 48 hrs. At the end of the culture period, the constructs (Ti/ECM) were rinsed and stored in distilled-deionized water at -20°C until further use.

Scanning Electron Microscopy

Each bioreactor produced six constructs; one was chosen for analysis by scanning electron microscopy (SEM, FEI Quanta 400 Environmental, Hillsboro, OR) and elemental dispersive x-ray spectroscopy (EDS, EDAX, Mahwah NJ) to visualize the top surface of the constructs prior to implantation. For this analysis, constructs were fixed in 2.5% glutaraldehyde for 2 hours, underwent a gradient increasing ethanol series, and were then left to air dry. Samples were mounted onto aluminum stubs and sputter coated with gold for 30 seconds prior to imaging. EDS was performed on

the samples to identify the presence of Ti, calcium, and phosphorus and to qualitatively map the location of these elements on the sample. The overlay of the three individual elements onto one single image was performed using EDAX Genesis software version 4.6 (Mawah, NJ).

Construct Implant Preparation

Prior to implantation, the constructs with *in vitro* generated ECM were subjected to a decellularization process. Briefly, the constructs underwent three freeze/thaw cycles in liquid nitrogen (10 min) and a 37°C water bath, respectively [101]. These Ti/ECM constructs were air-dried in a laminar flow hood and then sterilized with ethylene oxide and subsequent aeration prior to implantation.

Implantation Study

This study was conducted following an unpublished ASTM International draft standard *Guide for the Assessment of Bone Inductive Materials* which has since been replaced by the *Guide for the In Vivo Assessment of Demineralized Bone Materials* [175]. Sixty four 11-12 week old syngeneic, male Fischer 344 rats (Harlan, Indianapolis, IN) were used for the implantation study. Surgery was performed under general inhalation anesthesia with 4% isofluorane and oxygen. Three experimental groups (n=8) were investigated: (1) decellularized Ti/ECM constructs cultured for 8 days in the bioreactor (Ti/ECM/d8), (2) decellularized Ti/ECM constructs cultured for 12 days in the bioreactor (Ti/ECM/d12), and (3) decellularized Ti/ECM constructs cultured for 16 days in the bioreactor (Ti/ECM/d16). A control

group of plain Ti scaffolds (containing no *in vitro* generated ECM) was also included. The Ti and Ti/ECM constructs were implanted intramuscularly in the adductor thigh muscle of the leg in accordance with U.S. National Institutes of Health guidelines for a period of 28 and 56 days.

An animal was prepared for construct implantation by first placing it on its side under anesthesia, shaving the groin and right leg, washing with alcohol, and disinfecting with povidone-iodine. The animal was then given a subcutaneous injection of Ketofen® (5 mg/kg body weight, Fort Dodge, Fort Dodge, IA) and an intradermal injection of Marcaine® (0.1 ml of a 0.5% Bupivacaine solution with epinephrine 1:200,000, Hospira, Inc., Lake Forest, IL) at the incision site. Once complete, the animal was transferred onto a heating pad in the operating field where an incision was made parallel to the thigh through the skin and fascia. A pocket was made in the adductor thigh muscle. Each muscle pocket had one implant placed inside. The muscle and skin incisions were closed with 5-0 Vicryl sutures and 4-0 Monocryl sutures (Ethicon, Somerville, NJ), respectively. Each animal received only a single implant.

At the end of the surgery, the animal was placed on a heating pad and a subcutaneous injection of sterile saline (10 ml/kg/hr of surgery) was administered to compensate for any fluid loss during surgery. Each animal was monitored until effects of anesthesia had worn off and was then placed into its own cage with food and water. Twenty four hours post-surgery, the animals were given an additional

dose of Ketofen® for continued post-operative analgesia. The first 32 animals that received this second dose were placed under anesthesia to facilitate administration of this injection; however, this practice was discontinued after 4 animals died prematurely within 24 hours of this second round of anesthesia. Animals were monitored individually with a written record kept of their post-operative recovery. Extra injections of sterile saline were given to animals that did not exhibit signs of healthy metabolic activity for the first week after surgery.

Four animals from each group that were to be sacrificed at 56 days post-implantation received sequential fluorochrome injections to track the front of bone growth. Fluorochrome labels (25 mg/kg body weight) of tetracycline (Sigma, St. Louis, MO), alizarin-complexon (Acros Organics, Morris Plains, NJ), and calcein (Acros Organics, Morris Plains, NJ) were administered at 3, 5, and 7 weeks, respectively.

Histological Analysis

After euthanasia, the implants were retrieved along with the surrounding tissue and histologically processed. All specimens were fixed in 10% neutral buffered formalin for at least 1 week, rinsed with phosphate buffered saline, and stored in a 70% ethanol solution until further processing. After dehydration in an ethanol gradient, the specimens were embedded in methyl methacrylate (Fisher Emergo, Landsmeer, The Netherlands), and polymerized. Three transverse sections of 10 μm thickness were cut using a modified microtome saw equipped with a diamond blade (Leica

Microsystems SP1600, Rijswijk, The Netherlands). Sections were stained with methylene blue/basic fuchsin. Images were obtained with a light microscope (Eclipse E600; Nikon, Melville, NY) and attached video camera (3CCD Color Video Camera DXC-950P; Sony, Park Ridge, NJ).

An adaptation of an established histological grading scale for soft-tissue implants [176] was used to evaluate the tissue response bordering the implant surface (i.e., interface) and the pore spaces within the implants. Two individuals (QPP and FKK) blindly evaluated the sections independently and subsequently reached a consensus on the final score when differences arose. For each implant, three sections from the middle of the scaffold were evaluated and scored. Blood vessel counts were determined for each group by examining each section (at 40x magnification to clearly distinguish blood vessels) in three different locations. Three predetermined locations were viewed from each section; specifically, the center, 1 mm from the left margin and 1 mm from the right margin of the section. Counts were normalized to the area viewed (a rectangular field from the top to the bottom of the section in the predetermined locations), which was calculated by using Image Pro-Plus software version 5.1 (Media Cybernetics, Inc., Bethesda, MD) to trace the perimeter around the viewed area. Comparisons between the groups using the Tukey-Kramer procedure were made after a one way ANOVA indicated differences existed ($p < 0.05$).

Results

Scanning Electron Microscopy

SEM analysis was performed on scaffolds after *in vitro* ECM generation prior to implantation. The SEM images indicate that with increasing culture time, more cells and ECM were present on the top surface of the constructs (Figure 1, A-D). By day 16 of bioreactor culture, individual Ti fibers of the scaffold were difficult to distinguish. EDS analysis showed that the plain Ti and Ti/ECM/d8 constructs did not contain any calcium or phosphorus and as expected, consist of predominantly Ti fibers (blue) (Figures 1E and 1F). On the other hand, constructs that had been cultured for either 12 or 16 days demonstrated the presence of calcium (green) and phosphorus (red) (Figures 1G and 1H).

Macroscopic Evaluation

Of the 64 animals, four died on the 2nd day post-surgery. These deaths were determined to be unrelated to the implantation surgery but rather to increased stress to the animal resulting from the second round of anesthesia during the injection of Ketofen® 24 hours post surgery. Two of these animals were designated to be sacrificed at day 28 and had ECM constructs containing 8 and 12 days of matrix accumulation. The other two animals were to be sacrificed at day 56 and had ECM constructs containing 8 and 16 days of matrix deposition. Therefore, the number of implants per group was either 7 or 8, and at the conclusion of the study, a total of 58 implants (with the surrounding tissue intact) had been harvested. No noticeable macroscopic differences were discernable among any of the retrieved implants.

Histological Analysis

Significant artifact was present in each of the histological sections from the 28 day implants that prevented the scoring and analysis of these sections. Such artifact is characteristic of samples with incongruities in hardness that, in this case, likely stemmed from difference between sparse, immature tissue in the implant and the titanium fibers of the implant. Histological analysis revealed there was no bone formation in any of the constructs retrieved after 56 days of implantation, and little differences were found among the experimental groups and control (Figure 2). In addition to scattered foreign body giant cells, there were predominantly two tissue responses that were generally observed at the interface: fibrous capsule formation or the presence of fat cells (Figures 3A and 3B). Oftentimes, a combination of these two responses existed and based on the histological grading scale, the implants all scored a 3 (Figure 4). Within the implant porosity, there was more variation in tissue response among the samples, although this was not significant. Observed responses consisted of either obvious fibrous tissue or fat cells and young fibroblasts spread throughout the section (Figure 3C, 3D, and 3E). The majority of the plain Ti implants contained fat tissue within their porosity (7 of 8 implants), while most of the ECM implants contained mainly young fibroblasts or fibrous tissue (Figure 4). Additionally, the presence of fibrous tissue (a score of 4) was noted only in implants containing ECM.

Differences were found in the vascularity of the different implants. Ti, Ti/ECM/d8, Ti/ECM/d12, and Ti/ECM/d16 implants contained 42.9 ± 8.5, 51.6 ± 18.8, 56.5 ± 7.2, and 65.8 ± 17.1 blood vessels/mm^2, respectively. The distribution of the calculated number of blood vessels per area is presented as a Box-Whisker plot in Figure 5. A significant difference ($p<0.05$) existed between the Ti and Ti/ECM/d16 groups.

Discussion

We have previously shown that *in vitro* generated ECM secreted by MSCs has a significant impact on the osteoblastic differentiation of marrow stromal cells cultured *in vitro* either under static or dynamic conditions in the presence of osteogenic cell culture media supplements including dexamethasone [101, 172]. These promising results led us to investigate the potential of applying this strategy for bone tissue engineering applications *in vivo*. The objectives of this study were to evaluate (1) the capacity of *in vitro* generated ECM to induce bone formation in an intramuscular site in rats; (2) the soft tissue and angiogenic response to the ECM; (3) whether the ECM acts as a physical barrier to tissue in-growth; (4) and how the amount and maturity of the ECM influences these responses.

It was hypothesized that factors present in the *in vitro* generated ECM would aid in the recruitment and differentiation of undifferentiated cells resulting in bone formation when implanted intramuscularly in the adductor thigh muscle of rats. However, no bone formation was observed, and as a result, quantitative comparisons of bone formation between the experimental groups were not made.

Instead, the *in vivo* soft tissue response to the *in vitro* generated ECM was evaluated

within (1) the pore spaces of the implant and (2) at the interface between the implant

and surrounding tissue. Histological scoring of the sections demonstrated that there

were no significant differences in tissue response between any of the groups with

respect to both the interface and pore spaces of the implants. Therefore, the tissue

response to the cell-secreted ECM was similar to that of plain Ti. Additionally, this result

suggests that the decellularization and ethylene oxide sterilization procedures the constructs underwent prior to implantation

did not exacerbate the tissue response to these implants.

A fibrous capsule was observed at the interface of the implants in all the sections

analyzed. In addition to distinct fibrous capsule formation around the perimeter of

the implants, patches of fat cells were often interspersed with the fibrous capsule in

many of the implants, occurring more often with the ECM implants than in plain Ti

implants. It has been suggested that the occurrence of fat cells can indicate implant

biocompatibility [177] and thus the original scoring guide was modified to reflect that.

Similarly, there was no difference in tissue response within the porosity of the

implants. The majority of the implants contained either fat cells or immature fibrous

tissue interspersed with blood vessels. Based on the histological scoring guide,

there was no difference in the scores between any of the groups; however, the

presence of fat cells within the majority of the implants was noted more often in the

Ti and Ti/ECM d8 groups. This is the opposite of what was observed at the

interface; a possible explanation could be that the infiltration of fat cells into the

Ti/ECM/d12 and d16 implants might have been physically hampered by the ECM on

the surfaces of these particular implants. While a lower occurrence of fat cells was observed within the interior of these implants, fibroblasts, blood vessels, and some inflammatory cells (all of which are smaller than fat cells) could clearly be observed within the sections, indicating that ECM containing constructs did not impede tissue in-growth. Indeed, immature fibrous tissue was noted in some implants that contained *in vitro* generated ECM (Figure 4).

The mineralized content in the Ti/ECM/d12 and Ti/ECM/d16 constructs was expected to have a positive impact on osteogenesis by making these constructs more osteoconductive, serving as a substrate to allow tissue in-growth had any bone formation occurred. Also, the mineral content in these constructs could have led to increased protein adsorption from the surrounding environment, thereby enhancing its bone-forming capabilities in a manner similar to calcium phosphate osteoinduction [54]. However, the lack of bone formation suggests that the mineral deposits on these constructs were not of the specific chemistry, geometry, and composition for this phenomenon to occur [178]. Although we expected the mineral component to have these constructive functions, it should also be noted that the mineralized matrix could have inhibited the hydration of BMPs residing in the organic phase of the matrix, resulting in their inactivation [179, 180]. Thus, incorporating mineralized content into scaffolds can have potential advantages and drawbacks, indicating the need to further investigate the role of mineral content in the cell-secreted ECM and the effects of demineralization.

The observations from our previous *in vitro* study provide some insight into the disparate results from that study and the present one [172]. In both studies, ECM constructs were generated by seeding MSCs onto Ti scaffolds, culturing these constructs in the bioreactor to allow matrix deposition, and subsequently decellularizing them prior to use. The *in vitro* experiments showed that MSC osteoblastic differentiation was enhanced when seeded and cultured on ECM-containing scaffolds compared to plain Ti scaffolds. This effect was significantly more pronounced when dexamethasone was added to the culture media. Specifically, ECM constructs (8 mm diameter circular discs) seeded with 250,000 fresh MSCs and cultured in the presence of dexamethasone for 16 days in bioreactor culture contained 3800 μg of calcium while the equivalent constructs cultured in the absence of dexamethasone contained only 75 μg, a 50-fold difference [172]. Dexamethasone is known to alter the expression of various genes and cell receptors, which in turn could lead to favorable interaction with ECM components [181]. However, no direct comparison can be made with the results of the present *in vivo* study, as dexamethasone was included as a media supplement for specific groups in the *in vitro* study.

The *in vitro* experimental model also benefited from the direct seeding of fresh MSCs onto the ECM constructs, thereby facilitating cell-matrix interactions; *in vivo*, undifferentiated cells co-exist with inflammatory and other cell types within the local environment. Therefore, these progenitor cells may not have easy access to the ECM. Previous studies showed that the incorporation of MSCs into DBM implants

improved the quantity and quality of bone formed in humans and canine models [182-184]. Since we sought to examine the osteoinductivity of the *in vitro* generated ECM alone, the inclusion of osteogenic cells was not considered for this study.

While the inclusion of ECM alone did not induce bone formation, it did have a positive impact on the vascularity of the implants. As noted previously, many blood vessels could be identified within the sections. Vascularization of an implant is necessary for continued supply of nutrients to the interior of the implant in order to maintain its viability. Thus, early angiogenesis and continued blood vessel in-growth are crucial for the success of an implant as a graft material. In this study, the number of blood vessels observed on a per area basis increased with increasing culture duration of the ECM. Also, a significant difference was observed in the number of blood vessels between the Ti/ECM/d16 and plain Ti implants (Figure 5). That the ECM had an influence on the vascularity of the implants may be attributed to angiogenic factors released from the ECM. The implanted constructs in this study were well-vascularized after 56 days of implantation, and the appearance of more blood vessels in the implants containing ECM is an encouraging tissue response.

Conclusion

This study investigated the osteoinductive and angiogenic potential of an osteoconductive scaffold generated using a bioreactor for bone tissue engineering. Titanium fiber mesh scaffolds containing ECM secreted by cells were successfully generated and decellularized. Constructs with varying amounts of ECM were

produced using different *in vitro* bioreactor culture periods. These ECM-containing constructs were implanted in an intramuscular site to induce bone formation for 28 or 56 days. While no bone formation was observed, there was also no adverse tissue response attributable to the ECM, which did allow soft-tissue in-growth into the implants. Although the low mineral content in implants containing ECM did not confer osteoinductive properties, improved implant vascularity was observed. These results provide further insight into development of ECM based substitutes for tissue engineering applications and indicate that additional studies are necessary to determine the optimal culture conditions for the controlled production of an osteoinductive cell-secreted ECM. This ECM-based approach holds great potential and a key area for future study involves its evaluation in an orthotopic site.

Acknowledgments

Table 1. Modified histological scoring guide for the *in vivo* biocompatibility of implants in soft tissues.

Evaluation	Response	Score
Interface qualitatively	Shows fibrous capsule or fat cells in contact with the implant surface with scattered foreign body giant cells present	3
	Shows one layer of macrophages and foreign body cells are present	2
	Shows multiple layers of macrophages and foreign body cells are present	1
	Cannot be evaluated because of infection or other factors not necessarily related to the material	0
Pore space qualitatively	Is immature fibrous tissue (with or without fat cells) resembling connective tissue in the non-injured regions	4
	Shows blood vessels, and young fibroblasts nvading the spaces and/or fat cells and some inflammatory cells	3
	Shows giant cells and other inflammatory cells in abundance but connective tissue components in between	2
	Is dense and exclusively of inflammatory type	1
	Cannot be evaluated because of infection or factors not necessarily related to the material	0
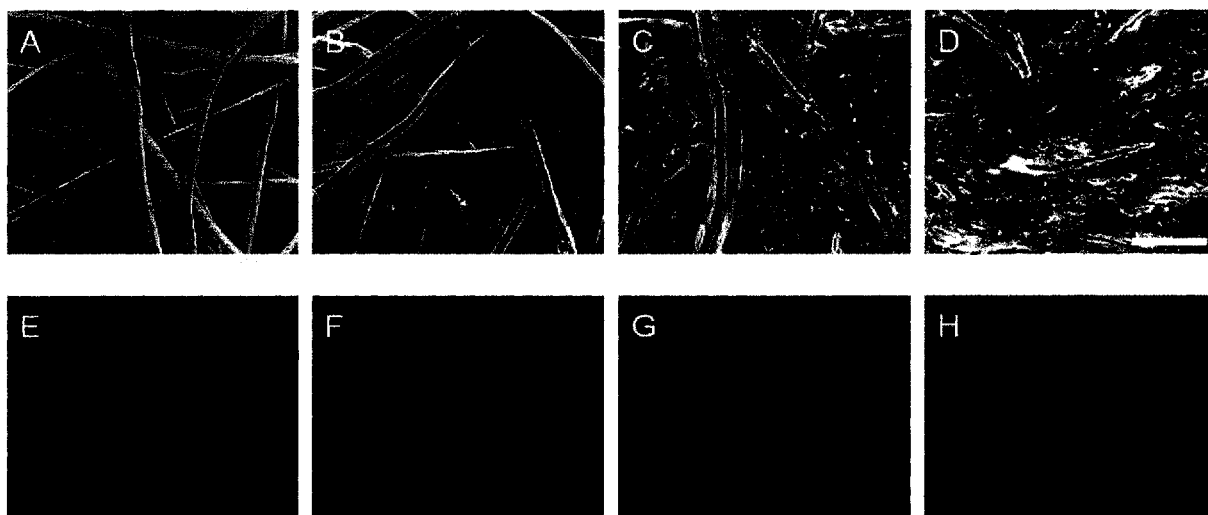
Figure 5-1

(A-D) Scanning electron micrographs of the implants illustrating extracellular matrix deposition on the top surface: (A) Plain Ti scaffolds (control group); (B) Implants containing extracellular matrix produced by MSCs for 8 days of bioreactor culture (Ti/ECM/d8); (C) Implants containing extracellular matrix produced by MSCs for 12 days of bioreactor culture (Ti/ECM/d12); (D) Implants containing extracellular matrix produced by MSCs for 16 days of bioreactor culture (Ti/ECM/d16). (E-H) Qualitative map overlays of the presence of phosphorus (red), calcium (green), and Ti (blue) as determined by energy dispersive x-ray spectroscopy: (E) Plain Ti scaffolds (control group); (F) Implants containing extracellular matrix produced by MSCs for 8 days of bioreactor culture (Ti/ECM/d8); (G) Implants containing extracellular matrix produced by MSCs for 12 days of bioreactor culture (Ti/ECM/d12); (H) Implants containing extracellular matrix produced by MSCs for 16 days of bioreactor culture (Ti/ECM/d16). Scale bar represents 100 μm and applies to A-H.
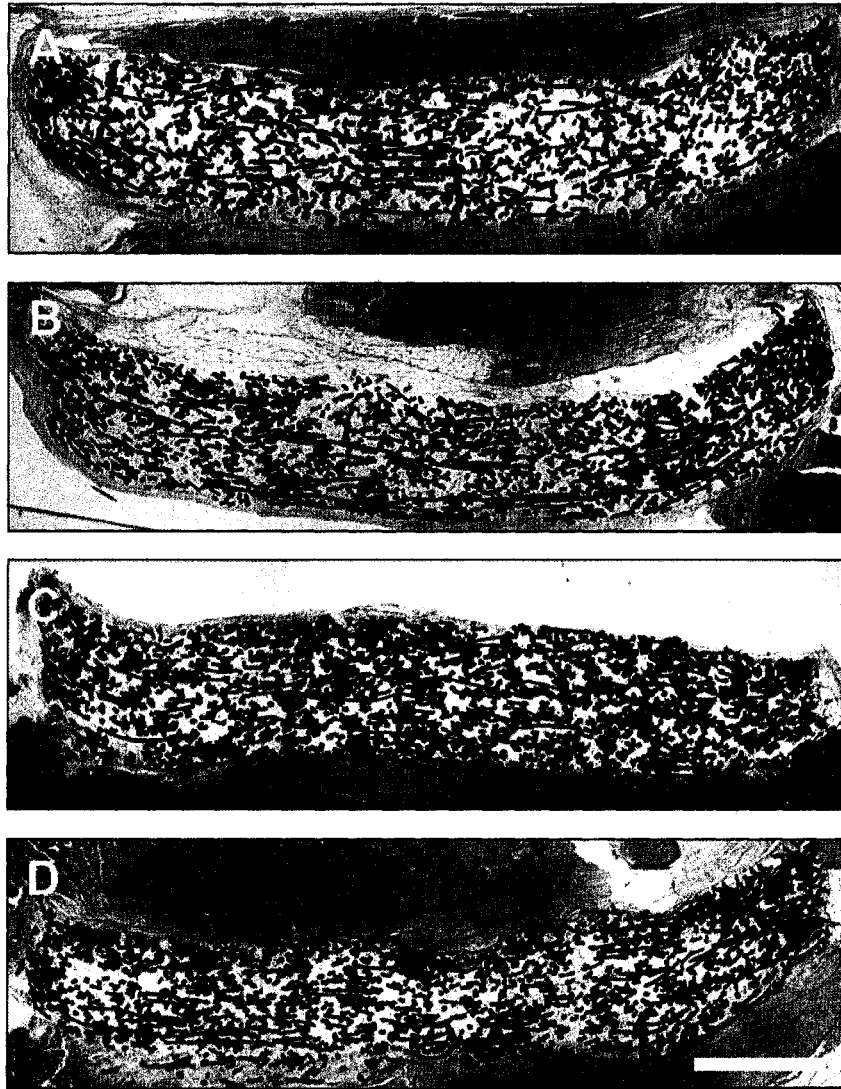
Figure 5-2

Representative light microscope images (10x magnification) of the different constructs retrieved after 56 days of implantation. (A) Plain Ti scaffolds (control group); (B) Implants containing extracellular matrix produced by MSCs for 8 days of bioreactor culture (Ti/ECM/d8); (C) Implants containing extracellular matrix produced by MSCs for 12 days of bioreactor culture (Ti/ECM/d12); (D) Implants containing extracellular matrix produced by MSCs for 16 days of bioreactor culture (Ti/ECM/d16). Sections were stained with methylene blue/basic fuchsin. No bone formation was observed in any of the implants. Scale bar represents 1 mm and applies to all images.
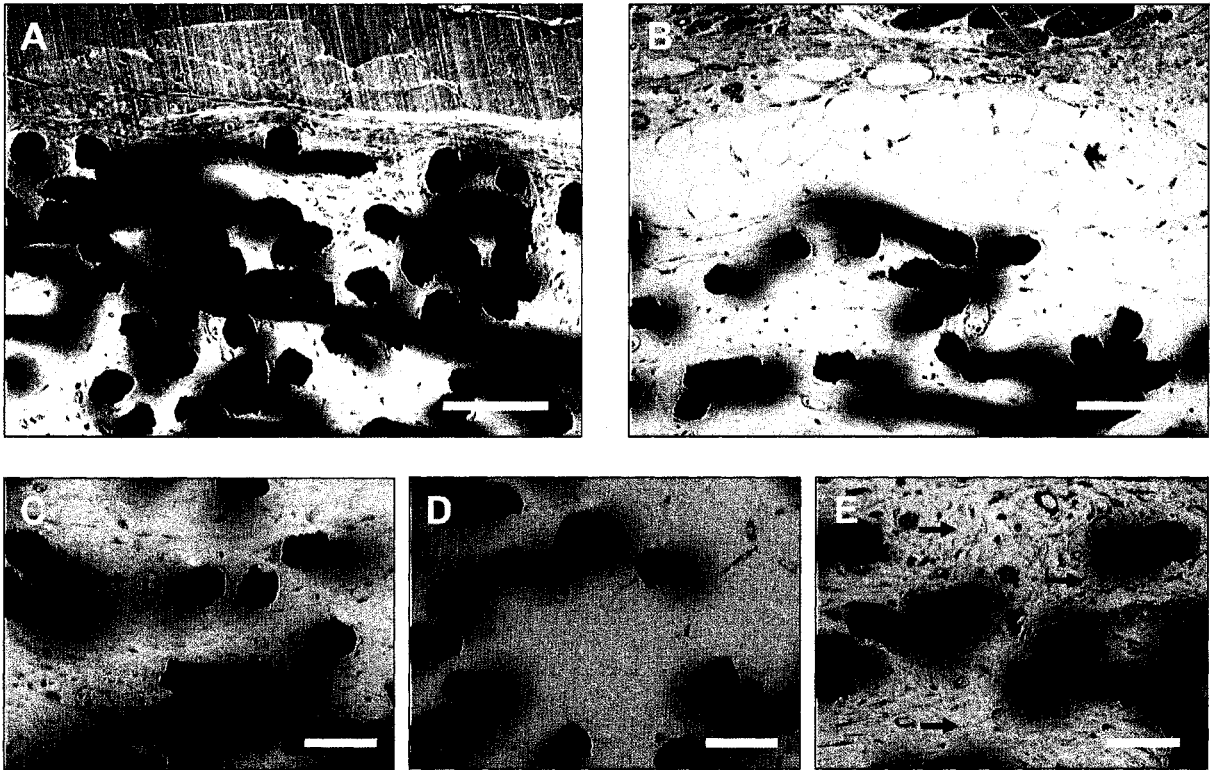
Figure 5-3

Light microscope images of the observed tissue responses at the implant interface (A, B 20x magnification, scale bar 100 mm) and within the pores (C, D, E 40x magnification, scale bar 50 mm). (A) Representative image illustrating an implant surface surrounded by a distinct fibrous capsule. (B) Representative image illustrating an implant surface contacted by a layer of fat cells. (C, D) Representative image illustrating an implant containing blood vessels (black arrow) and young fibroblasts and/or fat cells within its porosity. (E) Representative image illustrating an implant that contains immature fibrous tissue (black arrows). Sections were stained with methylene blue/basic fuchsin.
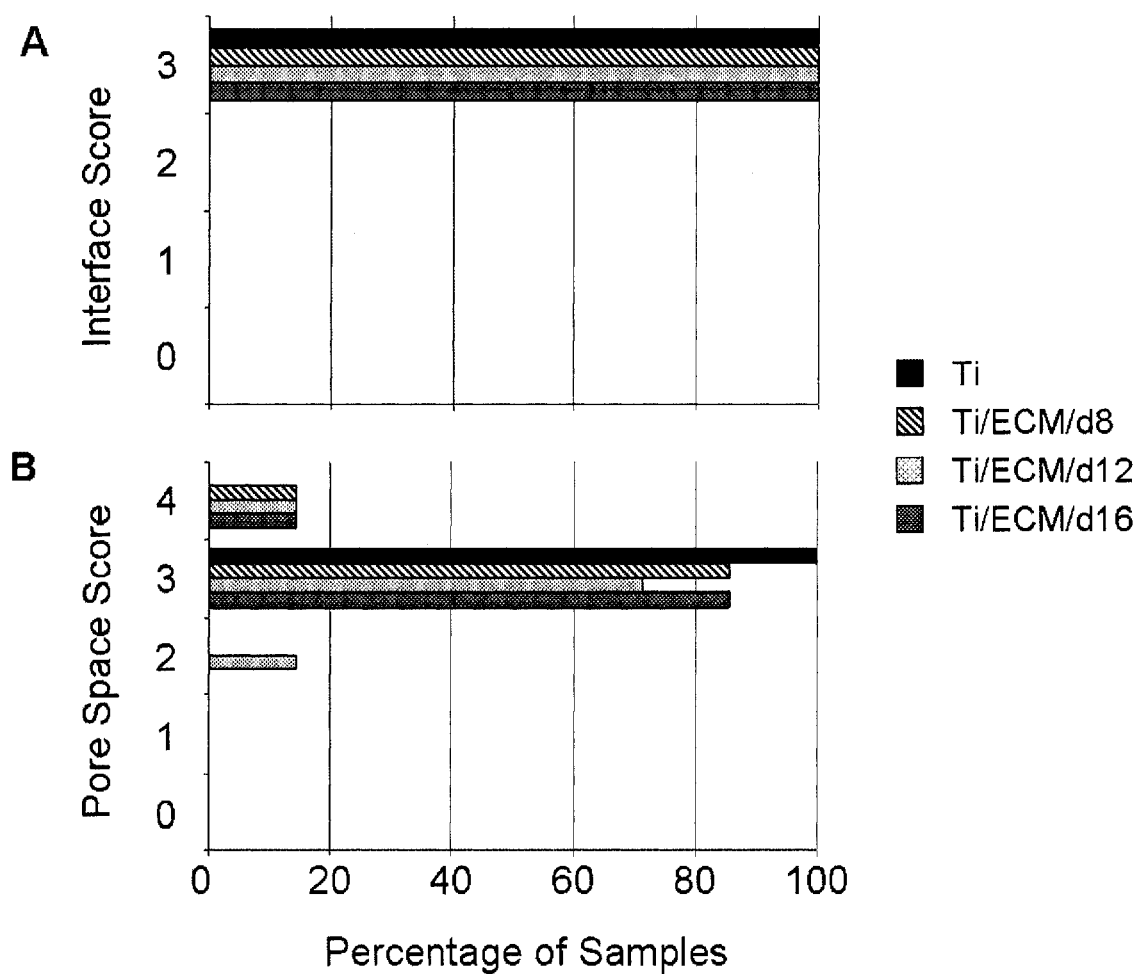
Figure 5-4

Summary of the histological grading of the tissue response at the (A) interface and (B) pore spaces of the implants. The data represent the percentage of specimens that received a particular score.
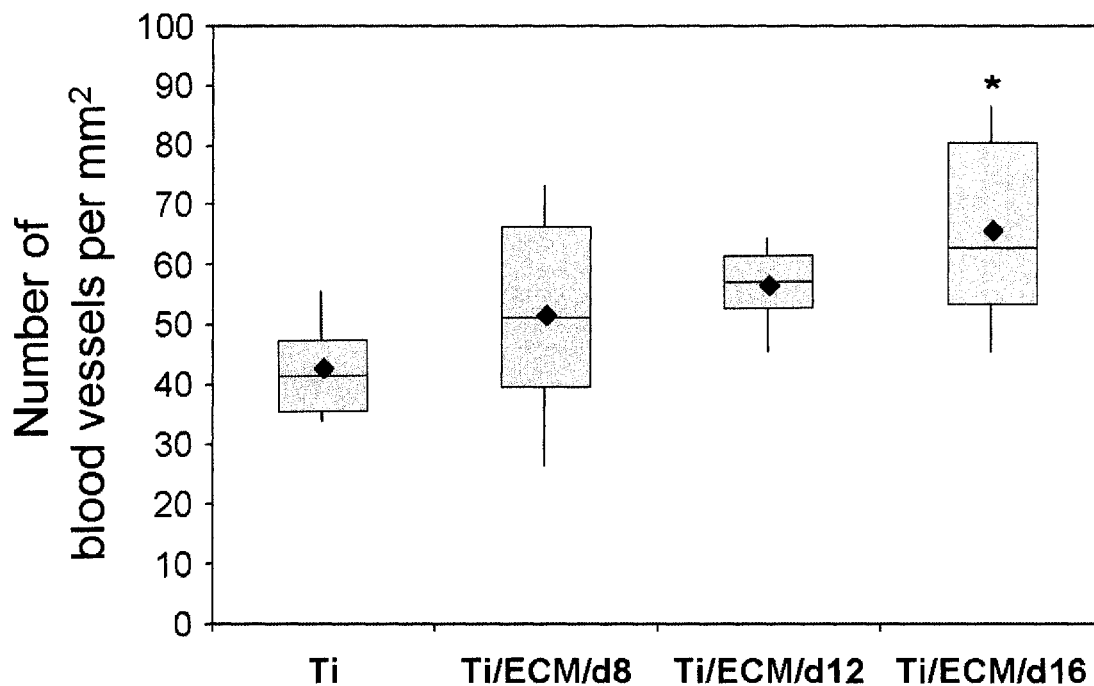
Figure 5-5

Summary of the number of blood vessels observed in the implants of the different groups displayed in a Box-Whisker plot. The diamond and line within the boxes indicates the average and median, respectively. The grey boxes represent the 25th to 75th percentile of the data and the error bars represent the 5th and 95th percentile. A * symbol indicates a significant difference with plain Ti ($p < 0.05$).

CHAPTER 6[*]

ELECTROSPINNING FOR TISSUE ENGINEERING APPLICATIONS

Abstract

Interest in electrospinning has recently escalated due to the ability to produce materials with nanoscale properties. Electrospun fibers have been investigated as promising tissue engineering scaffolds since they mimic the nanoscale properties of native extracellular matrix. In this review, we examine electrospinning by providing a brief description of the theory behind the process, examining the effect of changing the process parameters on fiber morphology, and discussing the potential applications and impacts of electrospinning on the field of tissue engineering.

Introduction

Electrospinning has gained popularity in the last ten years due in large part to an increased interest in nanoscale properties and technologies. This technique allows for the production of polymer fibers with diameters varying from 3 nm to greater than 5 μm [185]. Potential applications of electrospinning include filtration membranes, catalytic nanofibers, fiber-based sensors, and tissue engineering scaffolds [185, 186] [187].

One attractive feature of electrospinning is the simplicity and inexpensive nature of the setup; the typical electrospinning setup consists of only a syringe pump, a high voltage source, and a collector (Figure 1). During the electrospinning process, a polymer solution is held at a needle tip by surface tension. The application of an electric field using the high voltage source causes charge to be induced within the polymer resulting in charge repulsion within the solution. This electrostatic force opposes the surface tension; eventually, the charge repulsion overcomes the surface tension, causing the initiation of a jet. As this jet travels, the solvent evaporates and an appropriate collector can be used to capture the polymer fiber. Figure 2A shows a scanning electron microscopy image of an electrospun polymer mesh [69, 188] This approach has been used successfully to spin a number of synthetic and natural [189-193] polymers into fibers many kilometers in length [187, 188].

Recently, electrospinning has gained popularity with the tissue engineering community as a potential means of producing scaffolds. The objective of this review is to briefly describe the theory behind the technique, examine the effect of changing the process parameters on fiber morphology, and to discuss the application and impact of electrospinning on the field of tissue engineering.

Theory of Electrospinning

The stable electrospinning jet was described in detail by Reneker and Chun as being composed of 4 regions: the base, the jet, the splay, and the collection [188]. In the base region, the jet emerges from the needle to form a cone known as the Taylor cone. The shape of the base depends upon the surface tension of the liquid and the force of the electric field; jets can be ejected from surfaces that are essentially flat if the electric field is strong enough. Charging of the jet occurs at the base, with solutions of higher conductivity being more conducive to jet formation [188]. Electric forces then accelerate and stretch the polymer jet causing the diameter to decrease as its length increases. Additionally, solvents with high vapor pressures may begin to evaporate causing a decrease in jet diameter and velocity [188]. In the next region, Reneker and Chun hypothesized that radial charge repulsions caused the jet to "splay" into many small fibers of approximately equal diameter and charge per unit length [188]. The final diameter of the electrospun fibers upon collection was dependent upon how many splays were created [188].

Rutledge and co-workers have recently used high-speed photography with exposure times as low as 18 ns to demonstrate that the jet which appears to "splay" is actually a single, rapidly whipping jet [194, 195]. At high electric fields after traveling a short distance, the jet becomes unstable, begins to whip with a high frequency, and undergoes bending and stretching [194]. They modeled the behavior of the jet in terms of three instabilities: the classical Rayleigh instability and two "conducting" modes. The axisymmetric, Rayleigh instability is dominated by surface tension and is suppressed at high electric fields or charge densities [194]. The conducting modes are independent of surface tension and are dominated by electric forces; one conducting mode is axisymmetric and the other is nonaxisymmetric (whipping instability) [194, 196, 197]. Rutledge and co-workers examined the competition between these instabilities for various applied electric fields and the flow rate and determined the dominant mode [194]. They constructed operating diagrams which outlined the conditions at which whipping could be expected; their predictions agreed well with experimental results [194].

Electrospinning Process Parameters

From the previous description of the electrospinning theory, it is clear that the process can be manipulated by a number of variables. Doshi and Reneker classified the parameters that control the process in terms of solution properties, controlled variables, and ambient parameters [69]. Solution properties include the viscosity, conductivity, surface tension, polymer molecular weight, dipole moment, and dielectric constant. The effects of the solution properties can be difficult to

isolate since varying one parameter can generally affect other solution properties (e.g., changing the conductivity can also change the viscosity). Controlled variables include the flow rate, electric field strength, distance between tip and collector, needle tip design, and collector composition and geometry. Ambient parameters include temperature, humidity, and air velocity. In this section, studies that investigate the effect of each parameter on electrospun fiber morphologies and sizes will be highlighted.

Viscosity/Concentration

Solution viscosity (as controlled by changing the polymer concentration) has been found to be one of the biggest determiners of fiber size and morphology when spinning polymeric fibers. The relationship between the polymer viscosity and/or concentration on fibers obtained from electrospinning has been studied in a number of systems [[198]] including poly(DL-lactic acid) (PDLA) [199], poly(lactic-co-glycolic acid) (PLGA) [192, 200-202], poly(ethylene oxide) (PEO) [203-206], poly(vinyl alcohol) (PVA) [207], poly(methyl methacrylate) (PMMA) [208], polystyrene [209], poly(L-lactic acid) (PLLA) [189], gelatin [191], dextran[192] and collagen type I-PEO [210]. At low polymer concentrations, defects in the form of beading and droplets have been observed (Figure 2b) [200]; the process at these conditions was characteristic of electrospraying rather than spinning [189, 192, 200, 208]. Additionally, the presence of junctions and bundles have been seen indicating that the fibers were still wet when reaching the collector [200]. Increasing the solution viscosity by increasing polymer concentration yielded uniform fibers with few beads

and junctions [208]. In some cases, increasing the concentration of a polymer solution can also affect its surface tension [208]; however, for polystyrene solutions with constant surface tension, beading still decreased with increased viscosity [198, 210, 211]. This result indicates that the variation in viscosity was responsible for the morphological change of the fibers [203]. For solutions that were too concentrated (and therefore too viscous), the droplet dried out at the tip before jets could be initiated preventing electrospinning [201].

Attempts have been made to quantify the minimum polymer concentrations and viscosities required to electrospin fibers. Koski et al. found that it was possible to spin PVA as long as $[\eta]c > 5$ where $[\eta]$ was the intrinsic viscosity and c was the concentration [212]. For PEO, it was found that solutions with $[\eta]c > 10$ allowed for spinning [212]. McKee et al. found that a concentration greater than the entanglement concentration, c_e, was required to spin linear and branched poly(ethylene terephthalate-co-ethylene isophthalate) (PET-co-PEI) [207]. Solutions with concentrations 2 to 2.5 times the entanglement concentration yielded uniform, bead-free fibers [207]. Recently, Gupta et al. synthesized PMMA and determined the critical chain overlap concentration, c^* [207]. They determined that when the solution concentration was less than c^* there was insufficient chain overlap to form polymer fibers; at all conditions, droplet formation was observed [189, 200, 212-214]. In the semi-dilute region (concentrations between c^* and c_e), beading was occasionally observed. At concentrations approximately double c_e, uniform, bead-free fibers were obtained [209].

The diameter of the fibers produced by electrospinning has been found to increase with increasing solution concentration [204]. For example, PLLA fibers with diameters of 100 to 300 nm were produced from 1 wt% solutions while 5 wt% solutions yielded 800 to 2400 nm fibers [214]. Additionally, the diameter of PVA fibers increased from 87 ± 14 nm to 246 ± 50 nm by increasing the PVA concentration from 6% to 8% [189]. It was found that an increased fiber diameter correlated directly to a decrease in the surface area of electrospun mats [210].

Researchers have aimed to find a relationship between solution concentration and the fiber diameter. For example, it was found that increasing the concentration of gelatin yielded fibers with an increasing diameter with a power law relationship [212]. For polyurethaneurea, it was found that fiber diameter was proportional to c^3 for solutions of a single polymer molecular weight [200]. McKee et al. found for PET-co-PEI solutions that the concentration could be normalized by c_e. They found that the fiber diameter scaled with $(c/c_e)^{2.6}$ regardless of polymer chain length and extent of branching [200].

Electrospun fibers typically have a unimodal distribution; surprisingly, for PEO solutions spun at high concentrations, Deitzel et al. observed a bimodal distribution of fibers [210]. They found a secondary population of PEO fibers with a diameter approximately 1/3 of the primary population which they attributed to fiber splaying

events [74, 191, 192, 198, 202, 215, 216]. Demir et al. also found that polyurethane fibers electrospun at 12.8 wt% yielded fibers with 3 different sized diameters [202].

Conductivity/Solution Charge Density

It has been found that increasing the solution conductivity or charge density can be used to produce more uniform fibers with fewer beads present [192]. One approach to increasing solution conductivity has been through the addition of salt; for fibers spun from PEO [74], collagen type I-PEO [216], polyacrylic acid (PAA) [198], polyamide-6 [209], and PDLA [215] uniformity increased and beading decreased upon the addition of salt. Pyridium formiate has also been used to increase in conductivity of PLLA solutions and demonstrated a significant reduction in beading; it was hypothesized that this volatile salt additive would not remain in the fibers and therefore would not affect the properties of electrospun fibers [215].

Conductivity has also been increased by the addition of alcohol to the solvent resulting in smoother fibers of poly(hydroxybutyrate-co-valerate) (PHBV) with fewer beads present [217]. Likewise, the addition of tetrachloromethane, which reduced the solution conductivity, gave larger beads [217]. Cationic surfactants dodecyltrimethylammonium bromide and tetrabutylammonium chloride were added to polystyrene solutions, and it was found that a small amount (concentrations as low as 10^{-6} M) prevented the formation of beads [204]. The use of a nonionic surfactant, Triton X-405, did not completely prevent the formation of beads, so it was hypothesized that charged surfactants increased the solution conductivity and net

charge density causing an increase in the whipping instability yielding more uniform fibers [198].

The impact of the solution conductivity and charge density on the diameters of electrospun fibers was also studied. Zhang et al. showed that PVA fiber diameters were decreased from 214 ± 19 nm to 159 ± 21 nm when NaCl concentration was increased from 0.05% to 0.2% (spinning conditions: solvent = water, voltage = 5 kV, distance to collector = 10 cm, flow rate = 0.2 mL/hr) [198]. Zong et al. studied the effect of the addition of various salts (NaCl, KH_2PO_4, NaH_2PO_4) to PDLA solutions [198]. They found that salts with smaller ionic radii produced smaller fibers (~210 nm) while salts with larger ionic radii yielded larger ones (~1000 nm) [191]. They attributed this difference to the higher charge density, and thereby mobility, of ions with smaller radii; the higher mobility resulted in increased elongational forces exerted on the fiber jet yielding a smaller fiber [217]. Additionally, the addition of proteins to dextran solutions, yielded fibers with decreased diameters; since the proteins did not affect the solution viscosity, the variation in fiber diameter was attributed to changing the solution charge density [74]. In the same way, the addition of cationic surfactants was found to yield fibers with smaller diameters [216]; the addition of anionic surfactants has not been systematically investigated to date.

While increases in conductivity and charge density generally produced smaller fibers, for the spinning of PAA the reverse trend was observed: increases in conductivity yielded increases in the fiber diameter [215]. This difference could be

attributed to the ionic groups inherent in PAA. Similarly, the addition of 1 to 5 wt% MgCl2 to polyamide-6 increased the solution conductivity without impacting the viscosity or surface tension. This increase in conductivity also produced an increase in the fiber diameter [202, 204].

Surface Tension

The impact of surface tension on the morphology and size of electrospun fibers has also been investigated. PHBV solutions with different surface tensions and similar conductivities were obtained using triethylbenzyl ammonium chloride; it was found that beading was affected by surface tension [202]. The addition of ethanol to PEO and PVA solutions lowered the surface tension [204]. In the case of the PEO, the solution containing ethanol exhibited less beading [210]; however, when ethanol was added to PVA solutions, beading was increased [207]. The difference in the effect of ethanol addition to these systems was attributed to the fact that it is a non-solvent for PVA and a solvent for PEO. Another approach to reducing the surface tension of polyurethaneurea solutions was to add polydimethylsiloxane, but no significant effect in fiber morphology was observed [207].

Polymer Molecular Weight

Researches have examined the relationship between polymer molecular weight and the morphology and size of electrospun fibers. Gupta et al. synthesized PMMA varying in molecular weight from 12.47 kDa to 365.7 kDa [207]. They determined c^* for each of these polymers and found that c^* decreased with increasing molecular

weight. All polymers were then electrospun at identical conditions to isolate and ascertain the effect of molecular weight (spinning conditions: solvent = dimethylformamide, voltage = 10 kV, distance to collector = 15 cm, flow rate = 3 mL/hr). Upon electrospinning, they found that as the molecular weight increased, the number of beads and droplets was reduced. Uniform fibers were observed at concentrations that were six-fold or more greater than c^* regardless of polymer molecular weight [190]. Additionally, PMMA with a narrow molecular weight distribution gave uniform fibers at a lower concentration than those with larger molecular weight distributions [218]. For chitosan in acetic acid solutions, 30 kDa chitosan yielded fragile fibers with many beads present; polymer with a molecular weight of 398 kDa produced narrow fibers with rough surfaces [211]. For poly(N-isopropyl acrylamide), lowering the molecular weight produced smaller fibers which were more densely packed [216]. Varying the molecular weight of PEO from 600 to 4000 kDa during the spinning of PEO/chitosan solutions resulted in little difference in fiber diameter [208]. It was found that spinning polyamide-6 at various molecular weights gave fibers with diameters that were dependent upon the solution viscosity [219].

Dipole Moment and Dielectric Constant

Few studies have been performed to date to investigate the effect of dipole moment and dielectric constant on fiber properties. The spinning of polystyrene was studied in 18 different solvents, and it was found that the only solvents that could be used successfully were ones with high values of dipole moment [220]. Solvents with a

high dielectric constant were used to produce PMMA "cups" [198]. Also, the productivity (number of fibers produced per unit time) of spinning polystyrene fibers was found to correlate with the dipole moment and dielectric constant [204, 215, 220, 221]. To date, few studies have methodically examined the effect of dipole moment and dielectric constant on the resulting fiber morphology since these parameters are difficult to isolate.

Flow Rate

Few studies have systematically investigated the relationship between solution feed or flow rate on fiber morphology and size. In general, it was found that lower flow rates yielded fibers with smaller diameters [200]. Flow rates that were too high resulted in beading since fibers did not have a chance to dry prior to reaching the collector [200].

Field Strength/Voltage

One of the most studied parameters among the controlled variables is the effect of field strength or applied voltage. At low voltages/field strengths, a drop is typically suspended at the needle tip, and a jet will originate from the Taylor cone producing bead-free spinning (assuming that the force of the electric field is sufficient to overcome the surface tension) [198, 200]. As the voltage is increased, the volume of the drop at the tip decreases causing the Taylor cone to recede. The jet will originate from the liquid surface within the tip, and more beading will be seen [210]. As the voltage is increased further, the jet eventually moves around the edge of the

tip with no visible Taylor cone; at these conditions the presence of many beads can be observed [200, 202].

Using laser diffraction, it has also been shown that increased voltages produces jets with larger diameters and ultimately leads to the formation of several jets [198]. The presence of beads and junctions at high voltages was found when spinning solutions of PEO [221], PDLA [190], bisophenol-A polysulfone [189], chitosan [198], and gelatin [204]. The correlation between fiber diameter and the voltage was ambiguous. For PDLA [222] and PVA [221] higher voltages yielded larger fiber diameters; however, when spinning silk-like polymer with fibronectin functionality [190] and bisophenol-A polysulfone [189, 205], the fiber diameter tended to decrease with increasing applied voltage.

Distance between Tip and Collector

Varying the distance between the tip and the collector has been examined as another approach to control the fiber diameters and morphology. It has been found that a minimum distance is required to allow the fibers sufficient time to dry before reaching the collector [204]. At distances that are either too close or too far, beading has been observed [189]. For the spinning of PVA [190], gelatin [223], chitosan [222], and poly(vinylidene fluoride) [221], no significant effect of the distance between the tip and collector on the fiber size and morphology was observed. The spinning of silk-like polymer with fibronectin functionality fiber at closer distances produced flatter fibers while further distances gave rounder fibers [224]. For

bisophenol-A polysulfone, closer distances between the tip and collector yielded smaller fibers [224].

Needle Tip Design and Placement

Several designs and configurations of needle tips have been investigated for the electrospinning process. For example, Li and Xia developed a coaxial, 2-capillary spinneret (Figure 3a) [225]. Using feeds consisting of 2 immiscible liquids they were able to produce hollow nanofibers (Figure 3b) [226]. They also used this spinneret to prepare blends of polymers [227].

The use of multiple tips was investigated as a way to increase the throughput and production rate of electrospinning of PEO [228]. Multiple needle tips were also used to prepare blends of PVA and cellulose acetate. Using four tips and varying the number containing PVA and cellulose acetate, allowed for fibers with various weight ratios of PVA and cellulose acetate to be produced [228]. Using two tips and a collector that could move transversely, mixes of PEO and polyurethane fibers were spun [199]. The transverse motion of the collector allowed for more uniform distribution of each polymer [199].

Collector Composition and Geometry

A number of materials and geometries have been studied for the collection of electrospun polymeric fibers. Kim et al. collected PLLA and PLGA fibers on metal collectors, a water reservoir, and a methanol collector [213]. They found that

smooth fibers were obtained using the metal collector. Collection on the surface of water caused the hydrophobic polymer fibers to shrink, while methanol caused swelling of the fibers [213]. Cellulose acetate was collected using copper mesh, aluminum foil, water, and paper [213]. It was found that the packing density was influenced by the conductivity of the collectors: the more conductive collectors dissipated the charge of the fibers. When this charge was not dissipated (non conductive collectors), the fibers repelled one another yielding a more porous structure [229]. Also, porous collectors such as paper and copper mesh gave a less packed structure as compared to fibers collected on aluminum foil and water [195, 230]. Poly(ethylene-co-vinyl alcohol) was even spun directly onto a human hand [186].

Collectors with various geometries have also been designed and used. Rutledge and co-workers used two parallel plates when spinning their fibers in order to generate uniform electric fields [231]. Frame collectors were shown to yield aligned fibers with a conductive frame producing better alignment than a non-conductive one [231]. Also, an array of electrospun fibers has been produced using two conductive, collection rings [232]. The fibers were suspended between the rings, and fibers with lengths up to 10 cm were obtained. The rotation of one of the collection rings allowed for the production of a multi-filament yarn [232]. PEO was also spun using a multiple field method in which the polymer jet passed through 3 parallel rings each connected to an independent power supply [193, 233]. This method produced smaller, bead-free fibers that collected in a more focused area [234].

Fibers have also been collected using a rotating cylindrical drum collector rather than a stationary target (Figure 3c); doing so has allowed for the alignment of the fibers (Figure 3d) [235]. Better alignment was observed when this idea was extended to use a drum composed of copper wires that were grounded [232]. In another variation, a thin, steel pin was used as a counter electrode and was placed behind a rotating, non-conductive cylindrical collector; aligned fibers greater than 10 cm in length were obtained [236]. The rotating drum was also combined with the previously mentioned multiple field method to enable the collection of fibers into thin strips or yarns [236]. Theron et al. employed a "tapered and grounded wheel like bobbin" to collect and align nanofibers of PEO [216]. Their approach yielded fibers several hundred microns in length with diameters from 100 to 300 nm; braided fibers were also obtained [237].

Ambient Parameters

Few studies have been conducted to examine the effects of ambient parameters (i.e., temperature and humidity) on the electrospinning process. Mit-uppatham et al. spun polyamide-6 fibers at temperatures ranging from 25°C to 60°C [237]. They found that increasing the temperature yielded fibers with a decreased fiber diameter, and they attributed this decrease to the decrease in the viscosity of the polymer solutions at increased temperatures. The humidity was varied by Casper et al. while spinning polystyrene solutions [188]. Their work showed that increasing the humidity resulted in the appearance of small, circular pores on the surface of the

fibers; increasing the humidity further lead to the pores coalescing [238]. Spinning has also been performed under vacuum in order to obtain higher electric fields; doing so produced fibers and yarns with larger diameters [239].

In summary, we have highlighted studies that examine the effect of manipulating each parameter in the electrospinning process and the effect of that parameter on the resulting fiber morphology. Table 1 lists each parameter studied and its effect on the fiber morphology; however, it is difficult to isolate the effect of many of the parameters since they are interrelated. For example, changing the solution concentration/viscosity affects other solution properties such as the conductivity and surface tension.

Additionally, though a large number of distinct polymers have been electrospun, there has been little systematic investigation on the conditions required for successful spinning. Typically, a trial and error approach has been employed in which the solution properties and spinning parameters are varied until uniform, defect-free fibers are obtained. Previously, it has been shown that a minimum concentration is required to electrospin; if there is insufficient chain overlap, uniform fibers will not be observed. This minimum concentration is typically five to ten times c^*; once this minimum concentration has been determined varying other process parameters can be used to tune the resulting fiber morphology.

Overall, these studies highlight the potential of electrospinning for producing polymeric fiber meshes. By changing the solution and processing conditions, such as the polymer concentration, the properties of resulting mesh can be easily tuned. These meshes have tremendous potential as tissue engineering scaffolds, and the applications to date will be discussed in the next sections.

Tissue Engineering Scaffolds: Synthetic Extracellular Matrices

As defined by Langer and Vacanti in 1993, tissue engineering is "an interdisciplinary field that applies the principles of engineering and life sciences toward the development of biological substitutes that restore, maintain, or improve tissue function [240]." One aspect of tissue engineering has been on designing polymeric scaffolds with specific mechanical and biological properties similar to native extracellular matrix (ECM) in order to modulate cellular behavior. *In vivo*, a vast majority of the cells are in contact with the extracellular matrix, which is composed of a network of nanometer-sized proteins and glycosaminoglycans [241]. The intricate complexities of this spatial and temporal environment dynamically influence phenotypic and other cellular behavior by providing indirect and direct informational signaling cues [242]. For example, in bone, the presence of an organized type I collagen ECM for integrin binding is required for development of osteoprogenitor cells towards mature osteoblasts [67, 243, 244]. These types of interactions between cells and ECM can modulate cellular activities such as migration, proliferation, differentiation, gene expression, and secretion of various hormones and growth factors [57, 58]. Thus, the more closely the *in vivo* environment (i.e.

chemical composition, morphology, surface functional groups) can be recreated, the more likely the success of the tissue engineering scaffold [57].

Tissue engineering scaffolds function as temporary extracellular matrices until repair or regeneration occurs. A scaffold provides a 3D framework for the cells to attach and develop *in vitro* [58, 245]. Subsequently, the cell/scaffold construct can be implanted into a defect site for tissue repair and regeneration [57, 58]. Although the desired characteristics of a scaffold vary slightly with the tissue trying to be recreated, there are general properties that are desirable. First and foremost, the scaffold should be biocompatible, meaning that it will integrate with the host tissue without eliciting a major immune response [58, 130]. The scaffold should also be porous with a high surface to volume ratio to allow for cell attachment and in-growth as well as exchange of nutrients during *in vitro* or *in vivo* culture [130]. Furthermore, the porous nature of the scaffold will allow for angiogenesis upon implantation in a defect site (for vascularized tissues). Also, because the scaffold acts as a temporary support for the cells to adhere and proliferate, it should mimic native extracellular matrix both architecturally and functionally [245]. Finally, a tissue engineering scaffold should be biodegradable so that a second surgery is not required to remove the implant [246, 247]. The rate of degradation should coincide or at least be controllable to mimic the rate of neo-tissue formation [247].

Cellular Responses to Nanophase Elements

An important aspect of native ECM is its nanoscale components, such as collagen. It follows that tissue engineering scaffolds should also contain nanophase elements. Studies have shown that nanometer-sized elements can affect cellular behavior [248]. For example, osteoblast and osteoclast activity were increased on spherical nanophase alumina particles, which resembled the structure of hydroxyapatite crystals found in bone [249]. The nanofibrous architecture has also been shown to selectively promote osteoblast proliferation and differentiation in carbon nanofibers [250]. Nanogrooved surfaces can induce contact guidance of human corneal epithelial cells causing them to elongate and align their cytoskeleton along these topological features [239]. Highly porous PLLA scaffolds with nanoscale pores created using a liquid-liquid phase separation have been used for culture of neural stem cells and were shown to have a positive effect on neurite outgrowth [251]. Because the fiber diameters of nanofibrous scaffolds are orders of magnitude smaller than the size of cells, cells are able to organize around the fibers [252] or spread and attach to adsorbed proteins at multiple focal points [243].

Electrospinning for Tissue Engineering Applications

Compared to self-assembly and phase separation techniques, electrospinning provides a simpler and more cost-effective means to produce scaffolds with an interconnected pore structure and fiber diameters in the sub-micron range. The field of tissue engineering has sought to capitalize upon these features for the production of

3D scaffolds. The following sections highlight the use of electrospun scaffolds for tissue engineering applications.

Synthetic Polymer Scaffolds

There has been a surge in the use of electrospinning techniques to create nanofibrous scaffolds for tissue engineering. The most typical method of collecting the electrospun fibers is on a grounded, collecting plate. Because of the randomness of the instable fiber jet, a highly porous, nonwoven fibrous sheet with a large surface-to-volume ratio is collected [253]. Electrospun PLGA fiber mats have been shown to have a porosity greater than 90% [75, 252]. This material is ideal for tissue engineering scaffolds because the high surface area allows for a high percentage of cellular attachment as well as for multiple focal adhesion points on different fibers due to nano-sized fiber diameters [185, 186]. Additionally, fibers in the nanometer and sub-micron range more closely resemble the size-scale of extracellular components [253]. The versatility of the technique has allowed for spinning of a very diverse set of synthetic and biological materials [243]. Innovative designs for fiber collection broaden the library of available scaffolds and increase the likelihood of successful engineering of specific tissue types. Furthermore, functional modifications to electrospun nanofiber matrices can improve a polymer's biocompatibility and cytocompatibility.

Electrospun nanofibrous scaffolds are capable of supporting a wide variety of cell types. Human umbilical vein endothelial cells attached better and exhibited more

proliferation when seeded onto 50:50 poly(L-lactic acid-co-ε-caprolactone) (PLCL) fibers with a diameter of 300 nm compared to 7 μm fibers. Cells attached to microfibers were rounded in shape and non-proliferative, whereas on nanofibers, the cells were spread and anchored on multiple fibers [67]. Mouse fibroblasts seeded on PLGA nanofibers adhered and spread according to fiber orientation [254]. Similar results were reported by smooth muscle and endothelial cells seeded onto hybrid scaffolds of 75:25 PLCL [252].

The ECM-like properties of electrospun nanofibers have been shown to affect the phenotypic behavior of a variety of cell types. NIH 3T3 fibroblasts and normal rat kidney cells seeded onto polyamide nanofibers rearranged their actin cytoskeleton to a more *in vivo*-like morphology [255]. Breast epithelial cells on the same surface underwent morphogenesis to form multicellular spheroids. Fetal bovine chondrocytes seeded on nanofibrous poly(ε-caprolactone) (PCL) scaffolds were able to maintain the chondrocytic phenotype during 3 weeks of culture, specifically upregulating collagen type IIB expression, which is indicative of a mature chondrocyte phenotype [138]. These studies demonstrate that nanofibers scaffolds are not only cytocompatible but also can be used to stimulate and encourage cell proliferation and phenotypic behavior. To date, the use of such scaffolds has been investigated for the engineering of mainly cartilage, bone, ligament/tendon, and vascular tissues.

Cartilage and bone engineering strategies have increasingly incorporated marrow stromal cells (MSCs) because of their ability to differentiate into multiple cell lineages. Electrospun scaffolds have been shown to support the attachment and proliferation of MSCs [256]. Bone marrow-derived human MSCs seeded onto nanofibrous PCL scaffolds are able to differentiate into adipogenic, chondrogenic, or osteogenic lineages based upon the culture media selected [257]. Marrow stromal cells seeded on electrospun PCL and in the presence of transforming growth factor beta (TGF-β) differentiated into a chondrocytic phenotype at levels comparable to traditional pellet cultures. Moreover, the constructs displayed a zonal morphology with a layer of cartilaginous matrix composed of collagen type II, cartilage proteoglycan link protein, and aggrecan [258].

For bone tissue engineering, Yoshimoto et al. seeded MSCs from neonatal rats on electrospun PCL and cultured this construct in a rotating bioreactor; matrix mineralization and type I collagen deposition throughout the construct occurred after four weeks [74]. *In vivo* studies with similar constructs showed multi-layers of osteoblast-like cells, globular accretions, a woven bone-like appearance, and the presence of osteocyte-like cells embedded in mineralized matrix after explantation from the omenta of rats [74].

Lee et al. used a rotating cylindrical target to align polyurethate nanofibers for tissue engineering ligament [231]. They discovered that when exposed to mechanical strain, human ligament fibroblasts exhibited a spindle-shaped along aligned

polyurethane fibers and secreted more extracellular matrix than when attached to a random fiber configuration [67]. Dalton et al. used yarns produced by collection of nanofibers between dual rings as potential scaffolds for tissue engineering of tendons and muscles or as medical sutures [259].

Novel fiber collecting methods have been employed for tissue engineering of other tissue types. Ramakrishna et al. used a rotating drum collector for the alignment of electrospun fibers for vascular tissue engineering [260]. Human coronary artery smooth muscle cells attached and migrated along the axis of aligned PLCL (75:25) while expressing a spindle-like contractile phenotype; furthermore, the organization of the cytoskeleton inside these cells were parallel to the direction of the nanofibers [261].

Fiber alignment was also conducive for cardiomyocyte attachment and growth; when seeded onto electrospun PLLA scaffolds, they exhibited fiber-guided filipodia-like protrusions and developed into sarcomeres [262]. A contractile cardiac graft was created by Shin et al. from cardiomyocytes seeded onto an electrospun PCL mesh that was spun and collected across a wire ring [263]. The passive load of this structure helped to condition the cardiomyocytes, which expressed cardiac-specific proteins such as α-myosin, connexin43, and cardiac troponin I after 14 days of culture. Research is underway to extend this method to create implantable cardiac grafts.

Natural Polymer Scaffolds

Natural polymers are often used because of their enhanced biocompatibility, and biofunctional motifs [264]. Collagen, for example, is often used as a scaffold for cells since it makes up a major component of the extracellular matrix. Furthermore, incorporation of collagen and other biological components such as alginate [265], hyaluronic acid [266], and starch [193, 267] into synthetic polymers can improve the overall cytocompatibility of a scaffold. Thus, electrospinning of various biological substances, such as collagen, silk, fibrinogen, and chitosan for various biomedical applications have been investigated. Compared to synthetic polymers, electrospinning of biological materials is less versatile because a suitable solvent has to be used that does not compromise its integrity [193].

A collagen nanofiber mesh scaffold may have the advantage of not only resembling the size-scale but also the chemical and biological function of extracellular matrix. The spinning of type I collagen and type III collagen is feasible using 1,1,1,3,3,3 hexafluoro-2-propanol (HFP) as a solvent [268]. Collagen fiber diameters of 100 nm (type I) and 250 nm (type III) were achieved; these fibers possessed the typical 67 nm banding pattern observed in native collagen [269]. Culture of aortic smooth muscle cells under dynamic conditions led to proliferation and infiltration into the collagen network. By coating electrospun collagen with PCL, Venugopal et al. produced a scaffold with mechanical properties similar to skin and with the ability to support the attachment and proliferation of human dermal fibroblasts for dermal tissue engineering [270].

Elastin and fibrinogen are other proteins found in the body that have been electrospun into nanofibrous matrices. Elastin is a major component of the arteries and lungs, imparting resiliency and elasticity to these tissues [271]. Huang et al. developed a method to electrospin a synthetic peptide sequence of elastin, (Val-Pro-Gly-Val-Gly)$_4$(Val-Pro-Gly-Lys-Gly) mixed in water [272]. The ultimate tensile strength of dried nanofiber meshes was 35 MPa with a Young's modulus of 1.8 GPa. Through hydration and peptide cross-linking, it is possible to modulate these values to better mimic material properties of blood vessels.

Fibrinogen is a plasma serum protein that is part of the wound healing and blood clotting cascade. In order to spin human or bovine fibrinogen, it was solubilized in minimum essential medium/HFP (10:90) [273]. A linear relationship between the fiber diameter (80 – 700 nm) and fibrinogen concentration (0.083 - 0.167 g/mL) was observed. A fibrinogen nanofiber mesh can be utilized as a biomedical gauze for wound healing [274]. Additionally, a fibrinogen scaffold could be conducive for cartilage repair, as fibrin glue has been suggested as a candidate material for neocartilage formation [275, 276].

Interestingly, Fang and Reneker were able to spin actual DNA fibers [276]. Other natural molecules that have been successfully spun include silk, chitosan, and dextran. Silk fibrin is derived from silkworm and has good biocompatibility, biodegradability, and minimal inflammatory response when implanted *in vivo* [191,

211]. The silk nanofibers were able to support bone marrow stromal cell attachment and growth despite the presence of PEO in the spinning solution [228]. The preparations of chitosan and dextran have also been investigated and although their cytocompatibilities were not tested, these materials possess material and functional properties that could prove useful in tissue engineering strategies [267].

Composite Scaffolds

Composite scaffolds can also be created using electrospinning. For example, by sequentially spinning different polymer solutions, a scaffold with layers can be created. Each layer can be tailored for specific cell adhesion and could be potentially beneficial for zonal articular cartilage or arterial vessel repair [193]. Boland et al. have demonstrated smooth muscle cell infiltration into a multi-layered scaffold of collagen types I, III, and elastin when cultured in a rotary cell culture system [228]. Alternatively, two or more polymer solutions can be spun concurrently, resulting in a scaffold with mixed types of fibers. Collagen type I and collagen type III could be spun in this manner to create a scaffold that better mimic their *in vivo* ratios [266]. Another strategy is to use a polymer that degrades faster than the other, thereby increasing the microvoid spaces for tissue in-growth [228]. By co-spinning solutions of PCL and gelatin, bigger pore sizes were achieved upon gelatin degradation, resulting in an increase in rabbit bone marrow cell migration [277]. However, the reported migration depth of the attached bone-marrow stromal cells was still only about 100 μm. The incorporation of gelatin to increase the pore

size could be important since the small mesh sizes of electrospun scaffolds may be a limitation for tissue engineering applications.

In many of the *in vitro* studies described, the attached cells formed a monolayer at the top of the scaffold, but there is little evidence to suggest that cells migrated into the depths of the scaffold, especially since the pore sizes are small compared to the size of cells [257]. It has been suggested that cells cannot migrate through pores smaller than 10 μm [258, 267, 277]. In order for these nanofibrous scaffolds to be functionally useful as tissue engineering scaffolds, cultivation of cells into a 3D framework is critical [267, 278]. However, dynamic culture conditions and *in vivo* studies have shown that there is cellular penetration and matrix deposition throughout nanofibrous constructs although the mechanisms by which this occurs is not clear [257, 279]. It is posited that in these conditions, cells are able to push against the fibers during their migration paths and thus optimize pore sizes for further cellular infiltration [280].

Another type of composite scaffold developed has sought to incorporate carbon nanotubes into the electrospinning process as a means to reinforce polymeric fibers. Multi-walled carbon nanotubes were incorporated into PEO [281] and poly(acrylonitrile) nanofibers (PAN) [282]. The PAN fibers were spun using a moving collector, and, at high concentrations, the nanotubes were aligned. It was found that the reinforced polymer fibers had an increase in tensile modulus by 144% at 20 wt% nanotubes and tensile strength increased by 75% at 5 wt% nanotubes

[283]. Therefore, it may be possible to tailor the mechanical properties of nanofibrous scaffolds to resemble that of the target tissue.

Functionalized Scaffolds

A common strategy in tissue engineering is functionalization of a scaffold in order to increase biocompatibility or induce specific biological responses from attached cells. For example, prolonged *in vivo* activity of TGF-β2 was observed when it was bound to fibrillar collagen via poly(ethylene glycol) (PEG) compared to admixed samples [37]. Functionalization of electrospun fibers is also feasible and is typically carried out either by post-processing methods to conjugate molecules to the surface of nanofibers or by incorporating the bioactive factor into the spinning solution.

A novel, surface modified scaffold was created for support of primary rat hepatocytes to illustrate the feasibility of covalently attaching cell-adhesive molecules on nanofibers. PAA was grafted onto poly(ε-caprolactone-co-ethyl ethylene phosphate) (PCLEEP) allowing for conjugation of galactose ligand, which mediates hepatocyte adhesion. Hepatocytes cultured on these galatosylated PCLEEP nanofibrous scaffolds formed 20-100 μm spheroid aggregates that engulfed the nanofibers [284].

Recently, the conjugation of bone morphogenetic protein-2 (BMP-2) on chitosan nanofibers for bone regeneration was described by Park et al. [285]. BMP-2 conjugated to the surface of chitosan membranes increased osteoblastic cell

attachment and retained bioactivity for up to 4 weeks. Furthermore, the BMP-2 coated surface of the chitosan membranes resulted in better proliferation, alkaline phosphatase activity, and calcium deposition of osteoblastic cells compared to BMP-2 adsorbed membranes.

Casper et al. incorporated low molecular weight heparin (LMWH) into nanofibers of PEO and PLGA by mixing it directly into the spinning solution [248, 286]. By labeling the heparin with a fluorescent dye, the researchers were able to use multiphoton microscopy to show that heparin was distributed both throughout individual fibers as well as the thickness of the mesh. Incorporation of PEG-LMWH resulted in improved heparin retention in the fibers and could theoretically allow slower release of attached growth factors that bind to heparin, such as basic fibroblast growth factor, vascular endothelial growth factor, heparin-binding epidermal growth factor, and TGF-β. Thus, this approach represents a simple way to deliver growth factors through incorporation of a growth-factor binding molecule into electrospun fibers.

Drug Delivery Carriers

The effective delivery of therapeutic agents towards alleviating medical conditions is one aspect of polymeric biomaterials design. Polymeric drug delivery systems are advantageous because they can be controlled to efficiently deliver drugs to a localized area [287]. The nuances of such a system may have profound implications on tissue engineering: nanofibrous drug delivery systems may provide insight into the direct incorporation of bioactive growth factors into scaffolds. Additionally, drug

delivery systems can be combined with implantable tissue engineering scaffolds to prevent infection while repair and regeneration occurs. The following sections describe the approaches to modulate the release of drugs from nanofibrous scaffolds with an emphasis on antibiotic delivery.

The high surface area to volume ratio of electrospun scaffolds allows the efficient delivery of a loaded drug. Various drugs have been successfully introduced (i.e., maintain their structure and bioactivity) into nanofibrous scaffolds which can potentially be used as drug delivery vehicles [198]. One method to incorporate therapeutic drugs into nanofibers involves solubilizing the drug into the polymer solution to be spun [288]. Using this method, a loading efficiency of 90% into PDLA nanofibers was reported for the antibiotic drug Mefoxin [289]. Covalent conjugation to polymers represents another method to modulate drug release [289]. Jiang et al. used a PLGA/PEG-*g*-chitosan (PEG-*g*-CHN) blend for delivery of ibuprofen [198]. The interactions between ibuprofen and chitosan in the physical blend attenuated ibuprofen release rates by limiting its diffusion. Moreover, conjugation of ibuprofen to PEG-*g*-CHN prior to spinning reduced the release rate even further.

It has also been suggested that the high porosity of nanofibers allows for rapid diffusion of degradation byproducts [290]. Burst release of Mefoxin in PDLA nanofibers was observed in the first 3 hours and complete release occurred within 48 hours [186]. Such a release profile may be suitable for prevention of post-operation infections. However, the burst release may also be indicative of the drug

being attached only on the surface of the nanofibers. This was observed by Luu et al., who successfully incorporated intact plasmid DNA into PLGA and PLLA-PEG block copolymers that, upon release, was active over a 20 day period [291]. However, the DNA was localized on the nanofiber surfaces, leading to burst release within 2 hours. This approach could serve as a potential platform for successful gene delivery. A tubular fiber structure, in which a bioactive molecule is encased within the nanofibers, could be a more effective platform for drug and gene delivery systems [73]. By changing solution components, it might be possible to encapsulate DNA into the fibers by micelle formation and thus obtain slower release kinetics [287]. More research is required to understand the mode of drug incorporation in electrospun nanofibers; for example, the high surface to volume ratio of nanofibers scaffolds may contribute to an increased burst release delivery effect.

Different release rates may be obtained by simply varying the fiber diameter or loading dosage. Zeng et al. used triethylbenzyl ammonium chloride and sodium dodecyl sulfate in PLLA solutions to create more uniform and smaller fiber diameters; the release of rifampin from these fibers in the presence of proteinase K followed zero order kinetics [73]. Also, blends of biodegradable polymers with different degradation rates can be used to control drug release. Release kinetics of tetracycline hydrochloride changed from burst to a more sustained release when 50:50 blends of PLLA:poly(ethylene-co-vinyl acetate) (PEVA) were used compared to either PLLA or PEVA alone [71, 200, 292]. However, the polymer choice may be dependent on the desired drug to be released and vice versa. Doxorubicin

hydrochloride, a hydrophobic drug, was not well dispersed within electrospun PLLA fibers until it was made lipophilic [172].

Summary

Although electrospinning was first described over seventy years ago, attention on the technique has increased dramatically within the past ten years, due in large part to the rising interest in nanoscale properties and materials. The tissue engineering community has begun to capitalize on the inherent nanoscale nature of electrospun polymeric fibers as potential scaffolds to mimic native extracellular matrix. Electrospun matrices are able to support the attachment and proliferation of a wide variety of cell types; moreover, the cells are able to maintain their phenotypes on these nanofiber scaffolds. Using innovative collectors and spinning techniques, scaffolds with aligned fibers, different compositions, improved mechanical properties, varying degradation rates, or functional moieties can be produced. Nevertheless, despite the comprehensive experimental and theoretical studies illustrating the ability to control fiber formation, concerns with fiber diameter uniformity still need to be addressed. Precise control of fiber morphology will be necessary for improved scaffold designs that better recreate the functions of native extracellular matrix. The generation of designer scaffolds with clinically relevant dimensions and the homogeneous distribution of cells within them will also need to be addressed for tissue engineering applications.

Table 1. Summary of the effect of changing the electrospinning process parameters on the resultant fiber morphology.

Process parameter	Effect on fiber morphology	References
Viscosity/Concentration	• Low concentrations/viscosities yielded defects in the form of beads and junctions; increasing concentration/viscosity reduced the defects • Fiber diameters increased with increasing concentration/viscosity	6, 8, 9, 15-38
Conductivity/Solution Charge Density	• Increasing the conductivity aided in the production of uniform, bead-free fibers • Higher conductivities yielded smaller fibers in general (exceptions where PAA and polyamide-6)	8, 9, 20, 26, 30, 32, 37, 39-41
Surface Tension	• No conclusive link established between surface tension and fiber morphology	19, 21, 28, 38
Polymer Molecular Weight	• Increasing molecular weight reduced the number of beads and droplets	24, 29, 30, 34
Dipole Moment and Dielectric Constant	• Successful spinning occurred in solvents with a high dielectric constant	25, 41, 42
Flow Rate	• Lower flow rates yielded fibers with smaller diameters • High flow rates produced fibers that were not dry upon reaching the collector	15, 21, 38, 42, 43
Field Strength/Voltage	• At too high voltage, beading was observed • Correlation between voltage and fiber diameter was ambiguous	16, 22, 25, 26, 28, 30, 32
Distance between Tip and Collector	• A minimum distance was required to obtain dried fibers • At distances either too close or too far, beading was observed	6, 7, 21, 22, 32, 33, 43
Needle Tip Design	• Using a coaxial, 2-capillary spinneret, hollow fibers were produced • Multiple needle tips were employed to increase throughput	44, 46-48
Collector Composition and Geometry	• Smoother fibers resulted from metal collectors and more porous fiber structure was obtained using porous collectors • Aligned fibers were obtained using a conductive frame, rotating drum, or a wheel like bobbin collector • Yarns and braided fibers were also obtained	2, 10, 12, 19, 23, 27, 49-51, 53-55
Ambient Parameters	• Increased temperature caused a decrease in solution viscosity giving smaller fibers • Increasing humidity resulted in the appearance of circular pores on the fibers	5, 29, 56
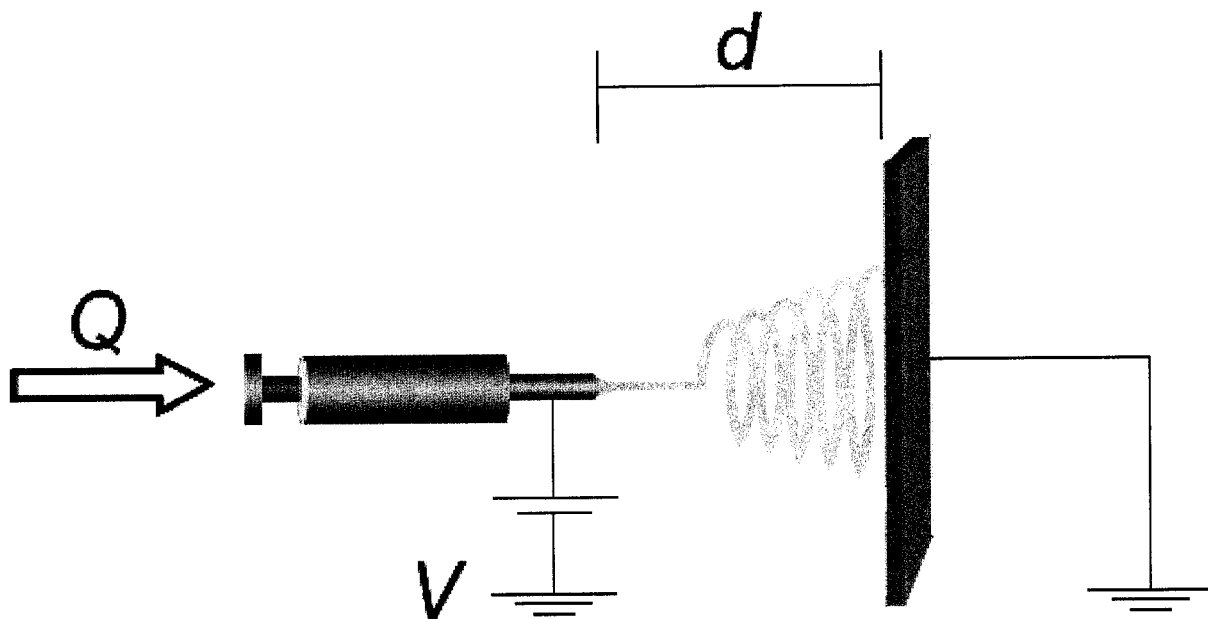
Figure 6-1

Typical electrospinning setup. Q represents flow rate, d is the distance between the plate and the needle, and V is the applied voltage.
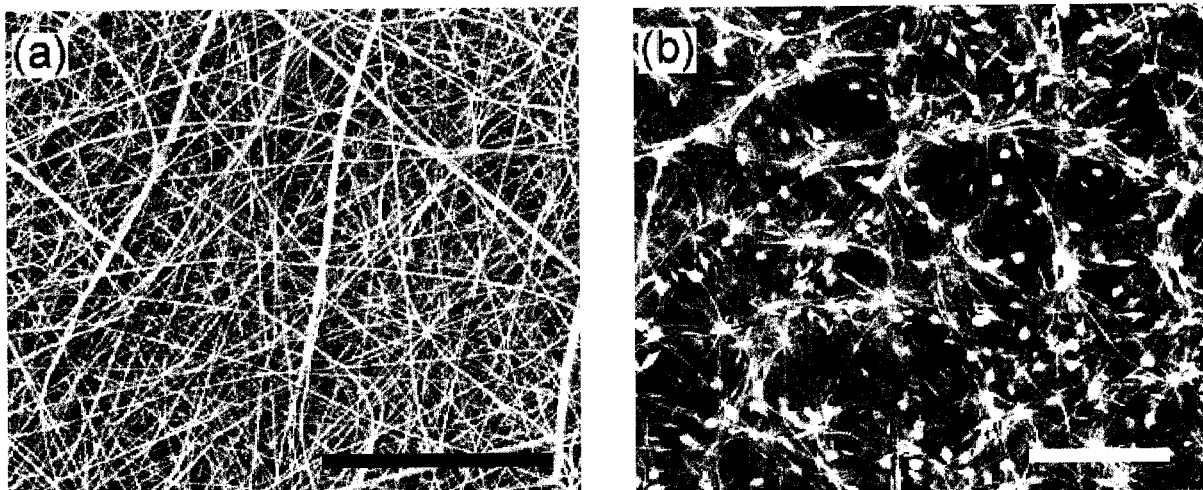
Figure 6-2

Examples of fiber meshes produced via electrospinning. (A) A non-woven, random polymer fiber mesh produced by electrospinning a 9% PCL solution. (B) Electrospun mesh obtained using a 5% PCL solution; at low polymer concentrations defects in the form of beads and junctions are observed. Scale bars, 100 mm, spinning conditions: solvent = chloroform/methanol (3:1 by vol), voltage – 25 kV, distance to collector = 15 cm, flow rate = 6mL/h.

Electrospinning setup modification	Resulting fibers
Co-axial, two capillary spinneret (a)	(b)
Rotating drum collector (c)	(d)
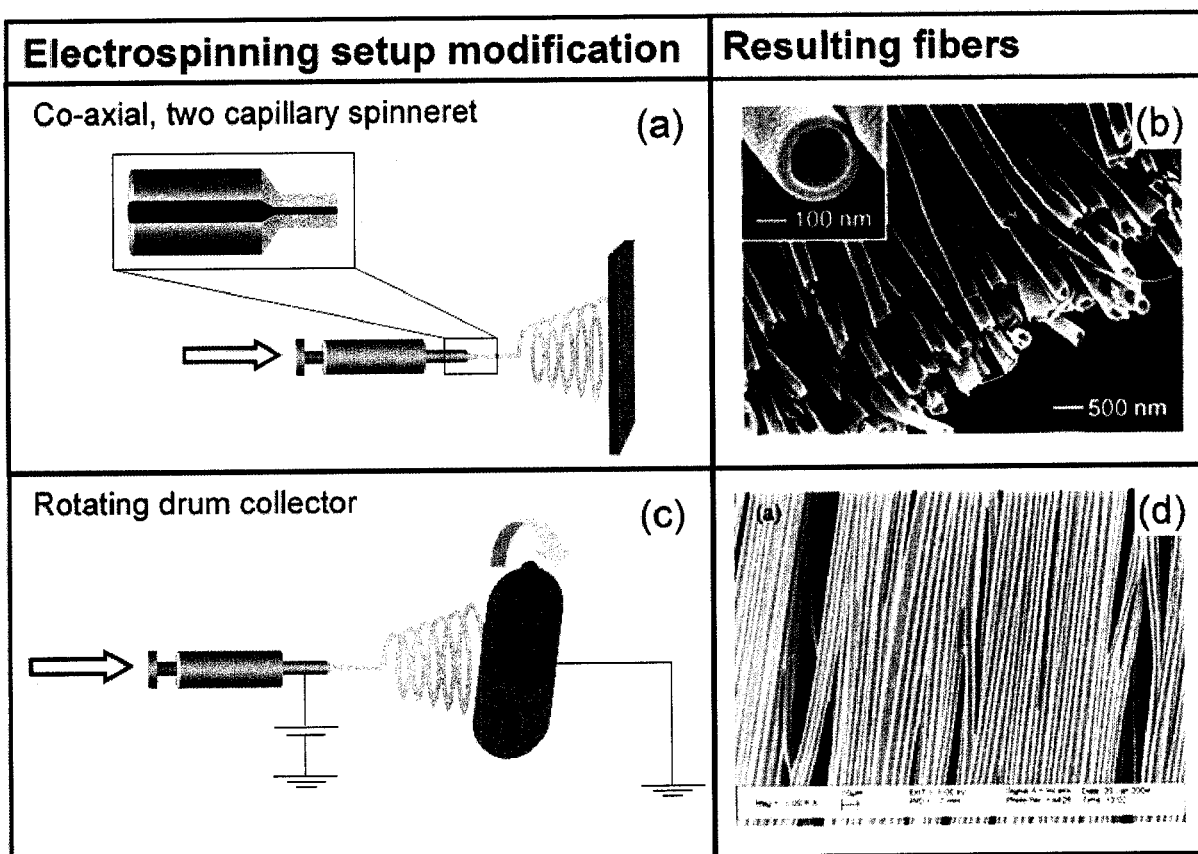
Figure 6-3

Modifications of the typical electrospinning setup used to produce meshes with unique morphologies. (A) A co-axial, two capillary spinneret can be used to electrosin hollow nanofibers showin in (B). A rotating drum collector (C) can be used to prodce aligned fibers (D). Adapted (A) and reproduced (C) from Li and xia. Direct fabrication of composite and ceramic hollow nanofibers by electrospinning. Nano. Lett. 4, 933, 2004. (D) Reproduced with permission from Chew et al. Sustained release of proteins from electrospun biodegradable fibers. Biomacromolecules 6, 2017, 2005.

CHAPTER 7[*]

ELECTROSPUN POLY(ε-CAPROLACTONE) MICROFIBER AND MULTI-LAYER NANOFIBER/MICROFIBER SCAFFOLDS: CHARACTERIZATION OF SCAFFOLDS AND MEASUREMENT OF CELLULAR INFILTRATION

Abstract

The physical and spatial architectural geometries of electrospun scaffolds are important to their application in tissue engineering strategies. In this work, poly(ε-caprolactone) microfiber scaffolds with average fiber diameters ranging from 2 μm to 10 μm were individually electrospun to determine the parameters required for reproducibly fabricating scaffolds. As fiber diameter increased, the average pore size of the scaffolds, as measured by mecury porosimetry, increased (values ranging from 20-45 μm), while a constant porosity was observed. To capitalize on both the larger pore sizes of the microfiber layers and the nano-scale dimensions of the nanofiber layers, layered scaffolds were fabricated by sequential electrospinning. These scaffolds consisted of alternating layers of poly(ε-caprolactone) microfibers and poly(ε-caprolactone) nanofibers. By electrospinning the nanofiber layers for different lengths of time, the thickness of the nanofiber layers could be modulated. Bi-layered constructs consisting of microfiber scaffolds with varying thicknesses of nanofibers on top were generated and evaluated for their potential to affect rat marrow stromal cell attachment, spreading, and infiltration. Cell attachment after 24

h did not increase with increasing number of nanofibers, but the presence of nanofibers enhanced cell spreading as evidenced by stronger F-actin staining. Additionally, increasing the thickness of the nanofiber layer reduced the infiltration of cells into the scaffolds under both static and flow perfusion culture for the specific conditions tested. The scaffold design presented in this study allows for cellular infiltration into the scaffolds while at the same time providing nanofibers as a physical mimicry of extracellular matrix.

Introduction

Three dimensional, porous polymer scaffolds are common in many tissue engineering strategies. A wide array of architectural configurations and geometries can be created using scaffold fabrication technologies such as rapid prototyping, melt extrusion, salt leaching, emulsion templating, phase separation, and electrospinning [293, 294]. Electrospinning is a process that can generate fiber mesh scaffolds with high porosities, large surface area to volume ratios, and variable fiber diameters [50, 76, 153, 295]. These features, along with the versatility and simplicity of the system, make electrospinning an attractive tool for the production of scaffolds.

The principle and theory behind electrospinning has been described in detail in the literature [246]. By modulating a combination of solution and processing variables (e.g., the polymer solution concentration, flow rate, collector distance, and applied voltage) fibers with diameters up to 10 μm can be produced [296]. Fiber diameter can have an effect on a variety of scaffold properties, such as porosity, pore size, and surface area [295]. These properties, in turn, are important in determining the functionality of scaffolds in tissue engineering applications. The pore size and porosity are critical features of a scaffold that affect cell attachment, proliferation, migration, and/or differentiation [297]. Surface topography and structural size-scale are additional parameters that have been shown to affect the orientation and biological function of cells [295, 298].

The complexity of cell behavior leads to challenges in the design and fabrication of ideal scaffolds for tissue engineering applications. For example, the optimal pore size for cell attachment, proliferation, and migration is not constant across cell types but varies from 5 to 500 μm [243]. A scaffold possessing two or more pore size distributions could facilitate the culture of several cell types to produce multiple interfaces on a single scaffold [243, 253, 254, 267]. Additionally, a scaffold consisting of a gradient in fiber diameter (and thus pore size) has been suggested as a useful model for zonal cartilage tissue engineering [299, 300]. Scaffolds containing gradients in pore size and porosity have also been investigated as bone substitute materials that would allow vascularization and direct osteogenesis on one side while promoting osteochondral ossification on the other [87, 299, 301].

The primary focus in electrospinning has been on the production of nanofibers due to their resemblance scale-wise to native ECM [67, 302]. Polymer meshes comprised of fibers with diameters as low as tens of nanometers, and exhibiting porosities as high as 90% and pore sizes as low as 100 nm have been reported [300]. Cells seeded onto nanofiber matrices tend to spread, attaching at multiple focal points, and in some cases extend filopodia along the length of the fiber [267]. Several studies suggest the ability of attached cells to push against nanofibers and migrate into the nanofiber matrix [302]; however, culture of cells on nanofiber matrices also results in a monolayer of cells and ECM, thus limiting their potential for 3D tissue engineering applications [266]. It has been suggested that smaller fibers can inhibit cellular infiltration [303]. The reduced cellular infiltration into the depths of

the scaffold has been attributed to the pore diameters being smaller than that of a cell [300]. For cell migration or infiltration to occur, the pore size of a scaffold should at least be the size of a cell [138]; a value of 10 μm has been suggested as necessary for cellular infiltration [71].

Although there has been much research related to nanofiber applications, there has been little reported on the electrospinning of electrospun microfiber scaffolds. Although microfiber scaffolds are not on the same size-scale as ECM components, they could be potentially advantageous since they are comprised of larger pores compared to nanofiber scaffolds. These larger pore sizes scaffolds could allow or facilitate cellular infiltration and/or diffusion of nutrients during *in vitro* culture [304]. In a study by Badami et al., MC3T3-E1 osteoprogenitor cells exhibited more proliferation on 2.1 μm fibers compared to 0.14 μm fibers, suggesting that cells on the microfiber scaffolds were able to penetrate into the scaffold and continue proliferating [305].

In this study, we investigated the electrospinning of poly(e-caprolactone) (PCL) microfiber scaffolds. PCL is a biocompatible, biodegradable polymer that has been successfully electrospun; furthermore, it has been shown to be capable of supporting a wide variety of cell types, including marrow stromal cells (MSCs) [172]. Electrospun scaffolds were characterized in terms of fiber diameter (measured by electron microscopy), pore size (measured by mercury porosimetry), and porosity (measured by mercury porosimetry, liquid intrusion, and gravimetry). The ability to

generate a wide range of fiber diameters (5 nm to 10 μm) by electrospinning allows for the possibility of designing fiber scaffolds with multi-modal characteristics to regulate the biological function of cells. Therefore, in addition to the microfiber scaffolds, we have utilized a multilayering technique to construct a bi-modal scaffold consisting of alternating layers of micro- and nanofibers. Using this strategy, the inherent advantages of both nanofibers and microfibers can be realized in a single scaffold. Bi-layered scaffolds consisting of a top nanofiber layer and a bottom microfiber layer were used as model systems to investigate the effect that nanofibers have on rat MSC attachment, spreading, and migration; static and flow perfusion culture conditions were considered.

Methods

Electrospinning Apparatus

Non-woven electrospun scaffolds were electrospun using the schematic shown in Figure 1. The setup consists of a syringe pump (Cole Parmer, Vernon Hills, IL), power supply (Gamma High Voltage Research, Ormond Beach, FL), and a square grounded copper plate (11 x 11 x 0.3 cm). A 10 ml syringe was filled with the appropriate polymer solution; the syringe was then fitted with a blunt needle tip (Brico Medical Supplies, Inc, Metuchen, NJ). A 19 cm diameter copper wire (18 gauge) ring was placed 6 cm in front of the tip of the capillary tip. The positive lead from the power supply was split and attached to both the needle and copper ring. During electrospinning, the fibers were collected onto a glass plate (0.22 cm thick) placed directly in front of the copper plate. After electrospinning, electrospun sheets

were dried overnight in a dessicator. Samples (8 mm diameter discs) were cut from the dried sheets using an arch punch (C.S. Osborne & Co., Harrison, NJ).

Electrospinning

PCL (MW=80,000, Sigma, St. Louis, MO) was used for electrospinning. A series of PCL polymer solutions (8-15 wt%) were prepared in chloroform:methanol ratios of 5:1, 6:1, or 7:1 (by vol) for the electrospinning of microfibers. Table 1 shows the solution and processing variables used to electrospin the different microfiber scaffolds. Q is the flow rate, d is the collector distance (from ring to collector), n is the needle gauge (length = 1.5 in.), and V is the applied voltage. For electrospinning 2 μm fibers, a parallel plate configuration [172] was used in addition to the ring. PCL nanofibers were obtained by electrospinning an 11 wt% PCL solution in a 1:1 (by vol) ratio of chloroform:N,N-dimethylformamide at the following conditions: d = 15 cm, V = 14 kV, Q = 0.8 ml/h, and n = 25.

Scaffold Morphology

Electrospun scaffolds were sputter-coated with gold for 1 min and observed with an FEI-XL 30 Environmental Scanning Electron Microscope (Mawah, NJ) at an accelerating voltage of 20 kV. For quantification of fiber diameter, measurements were made on the first five fibers that intersected a line drawn across the middle of an image (at 2000X magnification). Images from five random locations (selected blindly at 100X magnification) at the top and bottom of the scaffold were used for a total of 50 measurements.

Bi-layered scaffolds consisting of a top nanofiber layer (600 nm) and a bottom 5 μm microfiber layer were electrospun by sequentially electrospinning under the appropriate conditions listed in Table 1. The nanofiber density for different nanofiber electrospin times were characterized by counting the number of fibers that intersected a line drawn across the middle of the image. The percent coverage of nanofibers was taken as the number of nanofibers divided by the total number of fibers (microfiber and nanofibers) that intersect the line. To ensure uniformity and reproducibility of each condition, five different polymer sheets were electrospun, and five samples were taken from each sheet (top, middle, bottom, left, and right of the sheet). From each sample, three measurements were made (at three different magnifications 2000x, 2500x, and 3000x) for a total of 75 counts per condition. The frequency of counts (expressed as a percentage) was graphed as a function of the percent coverage of nanofibers (grouped in 10% bins). For example, a frequency of 20% for the 30% bin would indicate that 15 of the areas examined displayed between 20 and 30% coverage by nanofibers. Herein, these bi-layered scaffolds are referred to by the nanofiber electrospin time (e.g., a 30 sec scaffold refers to a 5 μm microfiber layer with a nanofiber layer on top produced by electrospinning nanofibers for 30 sec).

Cross-sectional images of multi-layered scaffolds were obtained by submerging the scaffolds in liquid nitrogen and cutting with titanium scissors. The samples were prepared for SEM as described above. In order to enhance the contrast between

nanofibers and microfibers in the SEM images, nanofibers and microfibers (based on measurement) were manually false-colored using GNU Image Manipulation Program software (available on the internet under a General Public License).

Mercury Porosimetry

Pore sizes of scaffolds comprised of microfibers were measured by using mercury porosimetry (Autoscan 500, Quantachrome Instruments, Boynton Beach, FL). Scaffolds ($\geq$1 mm in thickness) were weighed and placed into the sample chamber, and the void space in the chamber was filled with mercury (initial pressure $\approx$ 0.6 psi). The pressure was then increased at a rate of 0.01 psi/s until a total pressure of 50 psi was reached. The range of pore diameters, d_p, that could be measured using this approach could be calculated using the Washburn equation:

$$d_p = \frac{-4\gamma \cos\theta}{P}$$

where γ is the surface tension of mercury, θ is the contact angle between the mercury and the scaffold, and P is the pressure. As reported in the literature,[172] a contact angle of 140° between PCL and mercury in air was used. Therefore, the pressure range of 0.6 psi to 50 psi corresponds to pores ranging from 4 μm to 360 μm in diameter. The volume versus pressure data were converted to pore size, porosity, and surface area by using software supplied by the vendor (Quantachrome Instruments AUTOSCAN, ver. 3.00). Measurements were made on three samples of each scaffold type.

Porosity

The porosity of the microfiber scaffolds were also measured using gravimetry and liquid intrusion methods. Scaffolds (n=3) were weighed prior to immersion in ethanol (liquid intrusion). A brief vacuum was applied for ten minutes, and the scaffolds were left overnight on a shaker table to allow diffusion of ethanol into the void volume. The scaffolds were taken out, blotted with a Kimwipe, and re-weighed. The porosity was calculated by dividing the volume of intruded ethanol (as determined by the change in mass due to intrusion and the density of ethanol, 0.789 g/ml) by the total volume after intrusion (i.e., volume of the intruded ethanol combined with the volume of the PCL fibers determined from the initial mass of the PCL scaffold and the density of PCL, 1.145 g/ml).

For gravimetric measurements, the thicknesses of the scaffolds were measured using micro-calipers. Using the measurement of the thickness and knowing the diameter (8 mm) of the scaffolds, the volume of the scaffold could be determined. The mass of the scaffold was also measured allowing for determination of the apparent density of the scaffold, $\rho_{scaffold}$.The porosity, e, was then calculated according to the equation,

$$\varepsilon = 1 - \frac{\rho_{scaffold}}{\rho_{material}},$$

where $\rho_{material}$ is the density of PCL [172].

Scaffold Preparation

Preparation of the scaffolds for cell seeding consisted of sterilization, pre-wetting, and press-fitting phases. Scaffolds were first sterilized with ethylene oxide gas for 14 h. They were then transferred to a centrifuge tube and underwent a gradient ethanol series to 70% and left overnight. Centrifugation was performed to ensure complete wetting. The ethanol was then exchanged with 3 rinses of phosphate buffered saline and then with culture media and left in the incubator overnight. Prior to seeding, the scaffolds were press-fit into cassettes (designed for static and flow perfusion culture) and placed in a 6-well plate for seeding, as previously described [172].

Cell Culture Experimental Design

To investigate the applicability of the microfiber and micro/nanofiber layered scaffolds, we quantified cell attachment, spreading, and infiltration on 0 (microfiber scaffold with no nanofiber layer on top), 30, 90, and 300 s scaffolds. MSCs from male Fischer 344 rats (Harlan, Indianapolis, IN) were isolated and stored as previously described [306]. The prepared scaffolds were seeded with 250,000 MSCs in 200 μl of complete osteogenic media. Quantification of cellular attachment was performed on 4 scaffolds from each group at 2 and 24 h post-seeding. An additional scaffold from each group at both time points was used to stain F-actin to visualize cell spreading.

Twelve constructs from each group were also prepared for culture under static and dynamic conditions for determination of cellular infiltration. Scaffolds (die-punched

into discs with dimensions of 8 mm in diameter and thicknesses between 1 and 1.2 mm) were prepared for seeding as described above. After the 2 h attachment period, the wells of the tissue culture plate were filled with 9 ml of complete media. Twenty-four hours after seeding, six cassettes from each group containing the cell-seeded scaffolds were transferred to a flow perfusion bioreactor system driven by a peristaltic pump operating at a flow rate of 1 ml/min as described previously [307]. The constructs were cultured in complete media under static or flow perfusion culture for 12 d with media changes every 48 h. At the end of the culture period, 4 constructs were used for histological analysis and 1 for scanning electron microscopy.

Cell Attachment and Spreading

The cellularity of the constructs was determined using a fluorometric double-stranded DNA quantification kit [172]. To extract the DNA, constructs were first digested in a proteinase K solution as previously described [71, 268]. To do so, samples were transferred to 1.25 ml of Tris/EDTA buffer (6.055 mg/ml Tris(hydroxymethyl aminomethane), 0.372 mg/ml EDTA, pH 7.6 adjusted by HCl). Samples were digested at 56°C for 16 h after adding 250 ml of a proteinase K solution (1 mg/ml proteinase K, 10 µg/ml pepstatin A, and 185 µg/ml iodoacetamide in Tris/EDTA buffer). To ensure complete extraction, the constructs were then subjected to three repetitions of a freeze/thaw cycle (10 min at -80°C, 10 min at 37°C) followed by 20 min of sonication. The supernatant of the solution was used to measure the cellularity of the scaffolds by measuring double-stranded DNA using the PicoGreen assay (Molecular Probes, Eugene, OR) according to the

manufacturer's instructions. The results were expressed as cells per construct using a standard DNA curve created with double-stranded DNA standards and DNA extracted from known numbers of MSCs.

After 2 and 24 h post-seeding, scaffolds were removed from the cassettes and stained for F-actin with rhodamine phalloidin (Molecular Probes, Carlsbad, CA) according to the manufacturer's specifications. Briefly, the scaffolds were rinsed in PBS and fixed in 10% neutral buffered formalin (Sigma, St. Louis, MO) for 10 min. The scaffolds were then rinsed in PBS and washed with 0.1% Triton X-100 (Fisher Scientific, Pittsburgh, PA) in PBS for 5 min to permeablize the cell membranes. After rinsing in PBS, the scaffolds were incubated in 1% bovine serum albumin (Sigma, St. Louis, MO) in PBS for 20 min to reduce non-specific background staining. Finally, the scaffolds were stained with rhodamine phalloidin at the concentration recommended by the manufacturer for an additional 20 min before visualization. Images were recorded using a laser scanning confocal microscope (Zeiss LSM 510 Axiovert, Carl Zeiss, Germany) under a He/Ne laser (Ex/Em: 543/565 nm).

Histology

For histological analysis, the scaffolds were processed based on a protocol adapted from Holy and Yakubovich [308]. After the culture period, the scaffolds were harvested from the culture cassettes and placed in 10% neutral buffered formalin for further processing. All scaffolds were rinsed in ddH$_2$O and placed in Weigert's iron

hematoxylin (Sigma, St. Louis, MO) for 5 min under vacuum to ensure distribution of the stain throughout the scaffold; they remained in the hematoxylin for an additional 13 min and were then rinsed with ddH$_2$O. After rinsing in 100% ethanol, samples were stained with alcoholic eosin Y (Sigma, St. Louis, MO) in a similar manner. The scaffolds were then immersed in 70% ethanol until all residual eosin was removed and embedded in Histo-Prep freezing medium (Fisher Scientific, Pittsburgh, PA). Frozen sections of 5 μm thickness were obtained using a cryostat (HM500, Microm, Walldorf, Germany) operating at -23°C and mounted onto Superfrost Plus glass slides (Fisher Scientific, Pittsburgh, PA). The slides were allowed to dry overnight at 37°C and mounted with Permount (Fisher Scientific, Pittsburgh, PA). Images were obtained with a light microscope (Eclipse E600; Nikon, Melville, NY) and attached video camera (3CCD Color Video Camera DXC-950P; Sony, Park Ridge, NJ).

To quantify these results, a grid was overlaid on the obtained images. This grid consisted of twenty 10 μm thick "lines"; these lines were spaced evenly (30 μm apart) (Figure 2). To measure the cell infiltration, each of the lines was examined. The distance between the cell that was most penetrated and the top of the scaffold at that line was measured, as well as the thickness of the scaffold at that line. (For example, the sample image (Figure 2) demonstrated 100% infiltration.) Each image yielded 20 measurements of infiltration depth. For each scaffold, sections that were spaced by at least 500 μm were examined using this procedure; 4 sections were examined per scaffold. For each experimental group (nanofiber electrospin times of 0 s, 30 s, 90 s, and 300 s), 4 scaffolds were evaluated using this procedure.

Therefore, each experimental group had the infiltration depth analyzed using 320 different lines.

Statistical methods

Fiber diameter and porosity results are expressed as means ± standard deviation. Statistical differences between the fiber diameter size at the top and bottom of the microfiber scaffolds was determined by performing a Student's t-test (confidence interval of 99%). A single factor analysis of variance was performed to determine whether a significant difference existed between the porosity values measured using the different techniques for each targeted fiber diameter. Multiple pair-wise comparisons were made using the Tukey procedure at a significance level of 99%. Cell infiltration distance and attachment results are expressed as means ± standard deviation. A full two-factor analysis of variance with random-effect, nested factors was performed for both to determine any significance prior to making multiple pair-wise comparisons using the Tukey procedure at a significance level of 99%.

Results and Discussion

In this study, we explored the electrospinning of PCL micro- and nanofibers to generate 3-D scaffolds for tissue engineering applications. Specifically, the first part of this work focused on the characterization of microfiber scaffolds with respect to fiber diameter, pore size, porosity, and surface area. Additionally, results were compared to those obtained using a theoretical model. In the second part of this study, we capitalized on the versatility of electrospinning to fabricate (through

multilayering electrospinning) scaffolds composed of alternating layers of micro- and nanofibers. In particular, we wanted to determine the effect of duration of electrospinning on the percent coverage of nanofibers on top of an existing microfiber layer. Finally, we illustrated the potential use of these scaffolds by evaluating cell attachment, spreading, and infiltration on bi-layered scaffolds of nano- and microfibers.

Electrospinning and characterization of microfiber scaffolds

The electrospinning setup used in this study is a variation on the dual electrode setup [309]. We found that this arrangement caused the convergence of collected fibers into a confined circular space, helping to decrease the necessary time to produce three-dimensional scaffolds greater than 1 mm in thickness. Scaffolds with thicknesses near 1 mm have been considered before for tissue engineering applications as described previously [293, 310]. Using the electrospinning system, conditions for reproducibly fabricating scaffolds with different diameters were investigated. A common solvent used for electrospinning PCL is a 3:1 (by vol) chloroform:methanol mixture [310]; however, we observed that during the course of electrospinning, the Taylor cone became unstable and would occasionally drip, leading to irregular fiber formation. By increasing the chloroform:methanol ratio to 5:1 or higher, a stable Taylor cone was produced, allowing for prolonged electrospinning of microfibers.

Because of the interdependence of the Taylor cone stability and the electrospinning variables (e.g., flow rate, applied voltage, collector distance), this study focused on obtaining the conditions necessary to generate the targeted fiber diameters rather than determining the effect of individual variables on fiber diameter. For example, an increase in collector distance often had to be complemented with an increase in applied voltage in order to keep the Taylor cone stable over the course of electrospinning a three dimensional scaffold. In general, increasing the flow rate and the concentration of PCL required a larger applied electric field and longer collector distance yielding increased fiber diameter (Table 1). As shown in Table 2, by varying the electrospinning solution and processing conditions, scaffolds with fiber diameters ranging from approximately 2 to 10 μm were generated in a reproducible manner. (In this table, the "Targeted fiber diameter" refers to the average fiber diameter of the scaffold, rounded to the nearest integer. For example, the scaffold with an average fiber diameter on top and bottom of 2.12 ± 0.45 μm and 2.34 ± 0.29 μm, respectively is referred to as having a targeted fiber diameter of 2 μm). Addition of the parallel plate to the ring setup increased the uniformity of 2 μm fibers, but was unnecessary for larger fiber diameters. The top sides of these microfiber scaffolds are shown in Figure 3. Statistically significant differences in the fiber diameters on the top and bottom sides of the scaffolds were observed for the scaffolds comprised of 8 and 10 μm fibers, indicating that, it became more difficult to control fiber diameter at larger diameters. Investigation into this phenomenon revealed that the fiber diameters gradually increased for the first five minutes and then reached a plateau (data not shown).

Since pore size and porosity are critical features of a scaffold that influence the behavior of seeded cells, microfiber scaffolds were characterized with respect to these properties. Pore sizes were experimentally determined using mercury porosimetry and varied from approximately 20 to 45 μm for scaffolds comprised of 4 to 10 μm fiber diameters, respectively (Figure 4). The pore size of scaffolds made up 2 of and 3 μm fibers could not be determined because at the maximum pressure (50 psi) of the mercury porosimeter the intrusion volume had not reached a plateau [293, 310]. Using pressures greater than 50 psi would likely result in collapse and compression of the scaffold [293]. Therefore, for electrospun scaffolds comprised of fibers with diameters less than 3 μm, mercury porosimetery may not be a suitable technique for measurement of the pore size.

Porosities of the microfiber scaffolds were measured using three different techniques: mercury porosimetry, liquid intrusion, and gravimetry. It was expected that the liquid intrusion would yield an overestimation of the porosity of the scaffold due to diffusion of the ethanol into the fibers. Conversely, the mercury porosimetry was expected to underestimate the porosity since pores smaller than 4 μm will not be measured (see Methods section). However, there was no statistical difference between the porosities measured by these three techniques (Figure 5). In all methods, the measured porosities were between 84% and 89% regardless of the measurement technique selected.

Comparison of experimentally measured and theoretically predicted pore sizes

In order to estimate the pore size of electrospun scaffolds, a previously developed theoretical model was applied [293]. In this model, an electrospun scaffold was considered to be a collection of randomly placed straight rods. In developing this model, two-dimensional random networks were first considered [228]; the mean pore radius of these two-dimensional networks was computed based on the porosity and mean fiber diameter. To do so, it was assumed that the pore radii of these planes followed a Poisson distribution. The coefficient of variation of the pore radius was taken to be a constant that has been previously calculated for random networks [153, 300, 303]. This approach was extended by considering the three dimensional scaffold as a superposition of n two dimensional layers. Doing so allowed the average pore radius, $\bar{r}$, to be calculated using the following equation:

$$\bar{r} = \int_0^\infty r \frac{n}{\varepsilon} \left(\frac{\Gamma(k,br)}{\Gamma(k)} \right)^{(n\ \varepsilon)-1} \frac{b^k}{\Gamma(k)} r^{k-1} e^{-br} dr$$

where k and b characterize the gamma distribution, Γ, that describes the distribution of pore radii in two dimensions [50, 76], and e is the porosity.

Using the porosity (as measured by averaging the values obtained from the three techniques mentioned above) and fiber diameter measurements obtained from SEM, the predicted pore sizes of the microfiber scaffolds were calculated using the above equation. (Note: the error bars on the theoretical measurements are based on error in the porosity measurements.) These theoretically predicted values were compared with experimentally measured pore sizes obtained via mercury porosimetry (Figure

4). These results demonstrate that increasing the fiber diameter of the scaffolds yielded an increase in the pore size, as previously demonstrated [84]. For all conditions, the predicted pore size was smaller than those measured experimentally using mercury porosimetry. The differences between all theoretically predicted and experimentally measured pore sizes were less than 1.5 fold.

Since the pore sizes of scaffolds made up 2 of and 3 μm fibers could not be accurately measured using mercury porosimetry, they were estimated using the theoretical model. For these scaffolds, the porosity was first measured using liquid intrusion and gravimetry. The average porosity (determined by averaging the measurements), along with fiber diameter sizes obtained via SEM, was input into the theoretical model to estimate the pore size. Pore sizes of 10.5 ± 0.1 of and 14.9 ± 1.0 μm were calculated for the scaffolds comprised of 2 and 3 μm fibers, respectively. These results illustrate the utility of the model: when experimental approaches are not readily available for the characterization of the pore size of electrospun scaffolds, the model can be used to provide an estimate. These estimated values agree well with experimentally measured ones for all conditions tested (4 to 10 μm fibers). Furthermore, all that is required to estimate the pore sizes with the model is a measurement of the porosity and the average fiber diameters of the scaffold.

Fabrication and characterization of multi-layered scaffolds

In this work, we fabricated novel scaffolds to combine the beneficial properties of nanofibers and microfibers. To do so, we employed multilayering electrospinning to create scaffolds that included both nano- and microfiber layers. Multilayering electrospinning was demonstrated by Kidoaki et al. in which layered scaffolds were fabricated by sequentially electrospinning different polymers [138, 253]. Rather than changing the polymers, we applied multilayering to electrospin layers of the same polymer but with different morphologies. Specifically, PCL nanofibers of approximately 600 nm were electrospun onto 5 µm PCL fibers to form a bi-layered scaffold. By exchanging and alternately electrospinning the two polymer solutions and conditions (see Methods for the solution and processing conditions required to produce micro- and nanolayers), a scaffold with bi-modal morphological features was generated.

To characterize these bi-layered scaffolds, we evaluated quantitatively and qualitatively the extent of nanofiber deposition on top of a microfiber layer as a function of the duration of electrospinning time (Figures 6 and 7). Electrospinning for longer periods increased the amount of fiber deposition and, thereby, the thickness of the nanofiber layer. A quantitative analysis showing the percent of nanofiber coverage as a function of electrospinning time (15, 30, 60, and 90 s) is shown in Figure 6. At the shortest nanofiber electrospin time of 15 s, the nanofiber coverage varied from 1-40% with the majority of points examined displaying approximately 20% nanofiber coverage (Figure 7A); at a longer nanofiber electrospin time of 90 s, the coverage varied from 30 to 80% with the majority of points at approximately 60%

nanofiber coverage (Figure 7D);. After 120 s of electrospinning, the nanofiber layer appeared to cover the microfiber layer; the accumulation of the nanofiber layer after 300 s of electrospinning made it difficult to visually discern the microfibers underneath (Figure 7F). To further illustrate the versatility of the system, we electrospun a multilayered scaffold consisting of alternating layers of microfibers and nanofibers. Cross-sectional images of the layered scaffolds indicated that the layers produced by sequential electrospinning were well defined and distinguishable even when the nanofiber layer was thin (Figure 8).

The scaffold design presented herein integrates nanofibers and microfibers (both produced from electrospinning PCL) to form a single scaffold. As we have demonstrated, the thickness and coverage of the nanofiber layers can be controlled by modulating the electrospinning time of the nanofibers. Furthermore, the number, location, and spacing of the nanofiber layers could also be manipulated. Scaffolds containing different densities of nanofiber layers were used as model systems for investigating the cell infiltration into micro- and nanofiber scaffolds. Doing so provides critical information for the design of scaffolds to optimize the nanofiber (ECM scale mimic) and microfiber (allows for cell infiltration) balance.

Cellular Attachment, Spreading, and Infiltration

As a preliminary investigation into the potential application of the layered scaffolds, we evaluated cell attachment on 0, 30, 90, and 300 s scaffolds (Figures 3D, 7B, 7D, and 7F, respectively) at 2 and 24 h post-seeding. For all groups, more cells were

attached at the 2 h time point than at 24 h; there were also significantly more cells attached on the 0 s scaffolds compared to all other groups. After 24 h, however, the number of cells attached on the scaffolds was statistically similar between groups, with approximately 40% attachment (Figure 9).

While cell attachment did not seem to be enhanced by nanofibers, cell spreading appeared to be affected (Figure 10). A distinct visual difference in actin staining could be observed between the 0 s and other groups. At 2 h, cells on the 0 s scaffold appeared round, while cells on 30, 90, and 300 s were more spread. At 24 h, cells on the 0 s scaffold became more spread and some actin filaments could be visualized; in contrast, the number of filaments observed at 24 h was greater on 30, 90, and 300 s scaffolds. Fiber diameter has been shown to affect the phenotypic expression of cells [311]; therefore, it is expected that the extent of spreading will play a role in the proliferation and differentiation of MSCs.

Figure 11 shows the mean infiltration measurements of cells on 0, 30, 90, and 300 s scaffolds along with distribution in infiltration measurements. Culturing the constructs in a flow perfusion bioreactor significantly enhanced the infiltration distance of MSCs by a factor of five. Previous studies have also demonstrated that flow perfusion culture increases the distribution of cells compared to static culture [228]. Flow perfusion culture is beneficial for mitigating mass transport limitations inherent in static culture [266].

Complete infiltration (i.e., cells on both the top and bottom of the scaffold) was only observed for constructs cultured in the bioreactor, illustrating the benefits of flow perfusion culture on the distribution of cells throughout 3D scaffolds (Figure 12). The effect of the nanofiber layer thickness on MSC infiltration is reflected in the infiltration measurements, where the presence of a 300 s nanofiber layer resulted in a significant decrease in infiltration distance compared to the other scaffolds. This result indicates that increasing the thickness of the nanofiber layer can reduce the ability of MSCs to infiltrate through the scaffold porosity for the specific perfusion condition tested herein. Similar observations were made in static culture, in which the presence of a 300 s nanofiber layer also significantly reduced the infiltration distance of cells compared to the other groups within the static culture condition, with maximum infiltration distances of only approximately 200 μm.

Taken together, these results provide insight into the use of nanofibers for tissue engineering applications. The data suggest that the incorporation of a dense nanofiber layer can hinder cell migration, presumably due to the smaller pore sizes. Contrarily, the inclusion of nanofibers influences cell spreading, which can play a role in the proliferation and differentiation of MSCs. As several studies have shown, cells are able to proliferate, differentiate, and maintain their phenotypic expression on nanofiber scaffolds [312]. Further studies are required to elucidate the effect of the inclusion of nanofibers on MSC function (e.g., proliferation, spreading, and differentiation) under conditions of static and flow culture.

Various methods have been undertaken to address the concern of poor cell migration into nanofiber scaffolds. One approach is to introduce micro-voids into the scaffold after spinning. A dual-porosity structure was created using a salt leaching/gas forming method in conjunction with electrospinning. However, the fiber morphology of the scaffolds appeared to be significantly affected by the post-spinning processes . Alternatively, two different polymer solutions can be co-electrospun with one polymer acting as a leaching polymer to form micropores . Zhang et al. reported improved migration when using a PCL/gelatin nanofiber composite scaffold after the gelatin fibers were leached; overall migration was approximately 115 μm in leached scaffolds compared to 50 μm in plain PCL nanofiber scaffolds after one week of static culture. In another strategy, a cellular solution was electrosprayed concomitantly with electrospinning of poly(ester urethane) urea such that cells became interspersed within the scaffold . The setup, however, is considerably more complex than traditional electrospinning systems. Our strategy is to use microfiber scaffolds to generate the larger pore sizes while interspersing nanofiber layers throughout the construct to influence cell function.

Conclusion

The approach taken in this study was to exploit the extensive range of fiber diameters capable of being produced by electrospinning to generate scaffolds with unique properties. We demonstrated the ability to fabricate 3D microfiber scaffolds with controlled fiber diameters up to 10 μm. The average pore size of microfiber scaffolds was dependant on its fiber diameter and ranged from 10 to 45 μm while the

porosities were constant between 84-89%. To capitalize on the properties of both microfibers (i.e., pores large enough for cell migration) and nanofibers (i.e., physical mimicry of native ECM), multi-layered scaffolds were fabricated. MSCs attached well on both single and bi-layered scaffolds but were more spread when nanofibers were present. However, scaffolds with a 300 s nanofiber layer exhibited reduced cellular infiltration under both static and flow culture conditions tested herein. The optimization of the balance of nanofibers and microfibers in these multi-layer structures could have tremendous potential for 3D tissue engineering applications.

Acknowledgements

Table 1. Electrospinning processing conditions for PCL scaffolds.

Targeted Fiber Diameter (μm)	PCL Concentration (wt%)	Solvent Mixture (by vol)	Collector Distance (cm)	Voltage (kV)	Flow Rate (ml/h)	Needle Gauge
0.6	11	1:1*	15	14	0.8	25
2	8	7:1	18.5	27	3.5	22
3	9	6:1	15	19	4.5	18
4	10	7:1	16.5	20	8	18
5	12	5:1	19.5	22	8	18
6	13	5:1	23.5	22.5	8	18
7	14	5:1	28	24	8	16
8	14	5:1	33	27	10	16
10	14	5:1	33	25.5	18	16

* indicates the solvent mixture is chloroform:N,N-dimethylformamide; all other scaffolds were made using chloroform:methanol at the specified ratio (by volume)

Table 2. Average fiber diameters from the top and bottom of microfiber PCL scaffolds fabricated using the conditions described in Table 1. Measurements represent the mean and standard deviations of twenty-five fiber diameters on the top and bottom sides of the scaffolds. A * indicates a statistically significant difference (p < 0.01) between the top and bottom of the scaffolds.

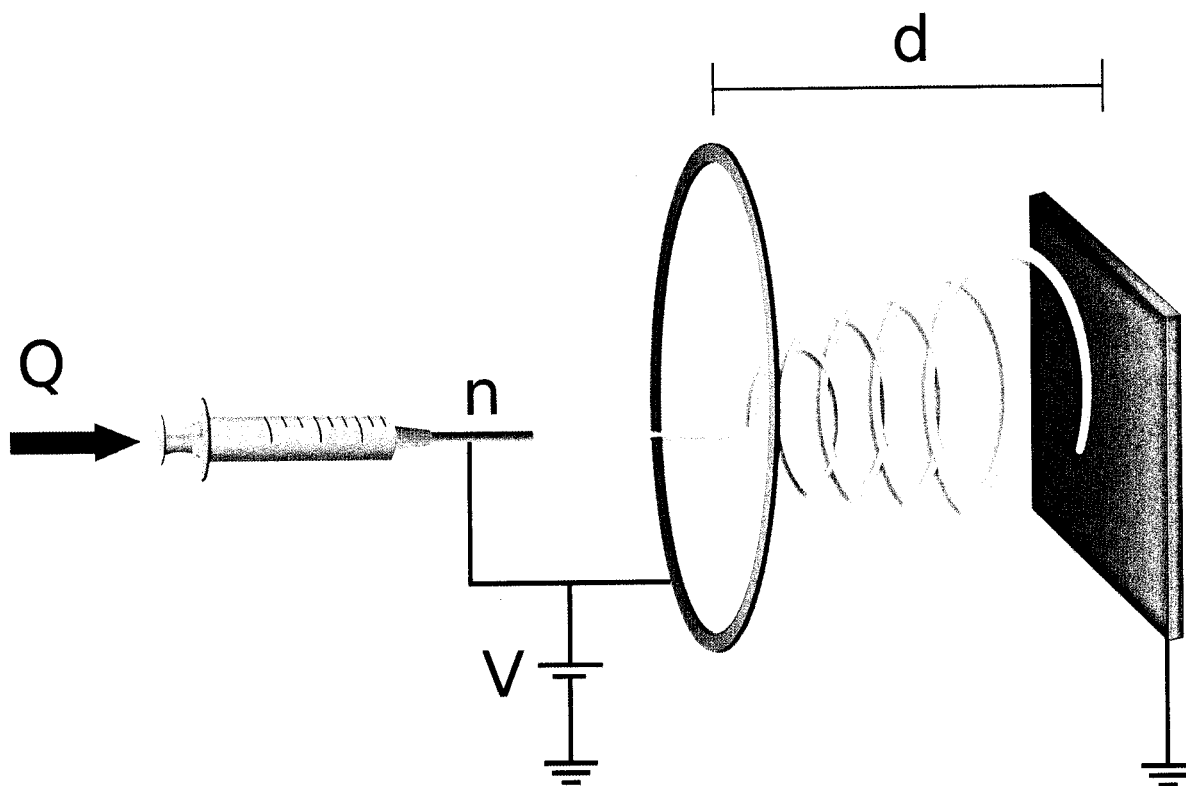| Targeted Fiber Diameter (μm)	Actual Fiber Diameter, Top (μm)	Actual Fiber Diameter, Bottom (μm)
2	2.12 ± 0.45	2.34 ± 0.29
3	3.18 ± 0.35	3.05 ± 0.39
4	4.01 ± 0.49	3.95 ± 0.51
5	4.86 ± 0.56	4.96 ± 0.46
6	6.37 ± 0.55	6.13 ± 0.37
7	6.90 ± 0.84	6.78 ± 0.85
8	7.94 ± 0.37	7.30 ± 0.46*
10	10.8 ± 0.81	9.57 ± 0.72*

Figure 7-1

Schematic representation of the electrospinning setup. The flow rate (Q), distance (d), applied voltage (V), needle gauge (n), and polymer solution properties could all be varied to affect the properties of the resulting fibers.
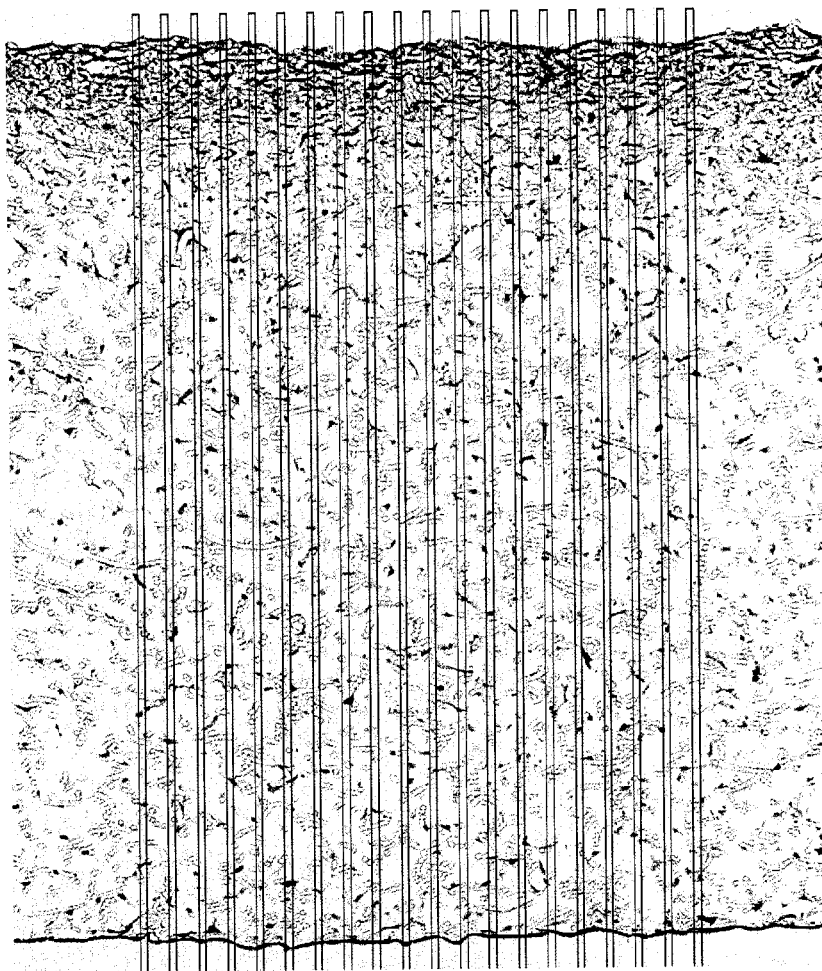
Figure 7-2

Representative light micrograph (10X magnification) of a cross-section of a PCL microfiber scaffold after staining with hematoxylin and eosin and cryosectioning. The grid was overlaid to allow for quantification of infiltration depth. Lines on the grid are separated by 30 μm and are 10 μm wide.

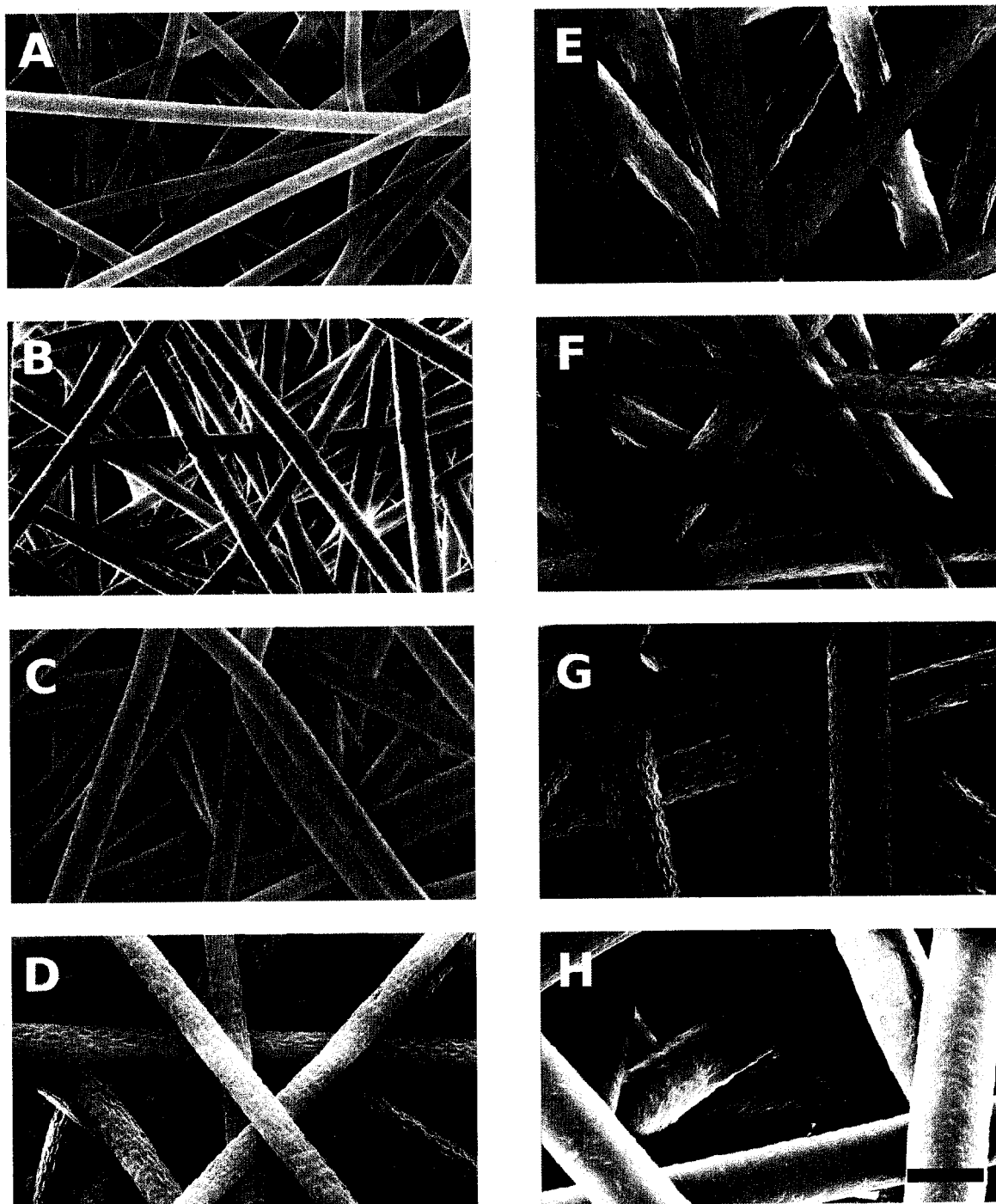**Figure 7-3**

Scanning electron micrographs of electrospun microfibers consisting of (A) 2 µm, (B) 3 µm, (C) 4 µm, (D) 5 µm, (E) 6 µm, (F) 7 µm, (G) 8 µm, and (H) 10 µm fiber diameters. The scale bar shown applies to all images and is equal to 10 µm.
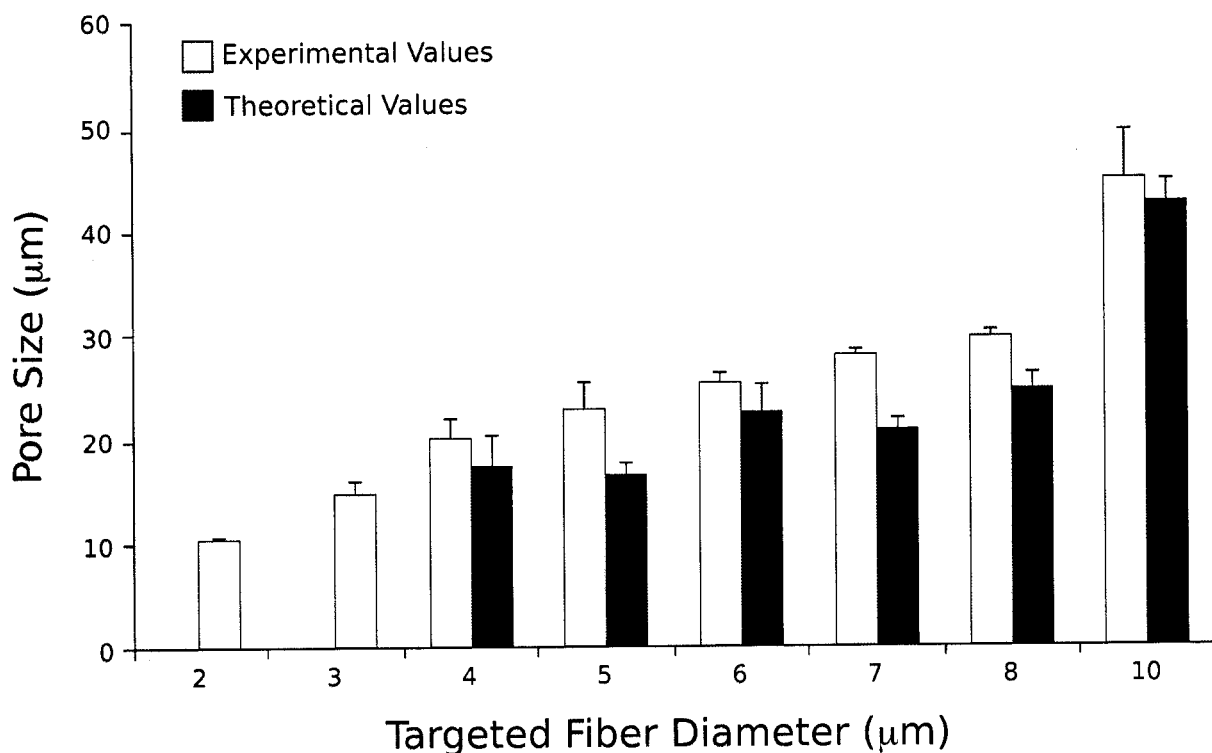
Figure 7-4

The pore size of microfiber scaffolds plotted as a function of fiber diameter. Experimental measurements were performed by mercury porosimetry. Theoretical values were calculated using porosity measurements obtained by averaging measurements from mercury porosimetry, liquid intrusion, and gravimetry. The experimental data represent the average of three samples with the error bars representing the standard deviations. Error bars on the theoretically predicted pore sizes are computed using the standard deviation of the input porosities and fiber diameters.
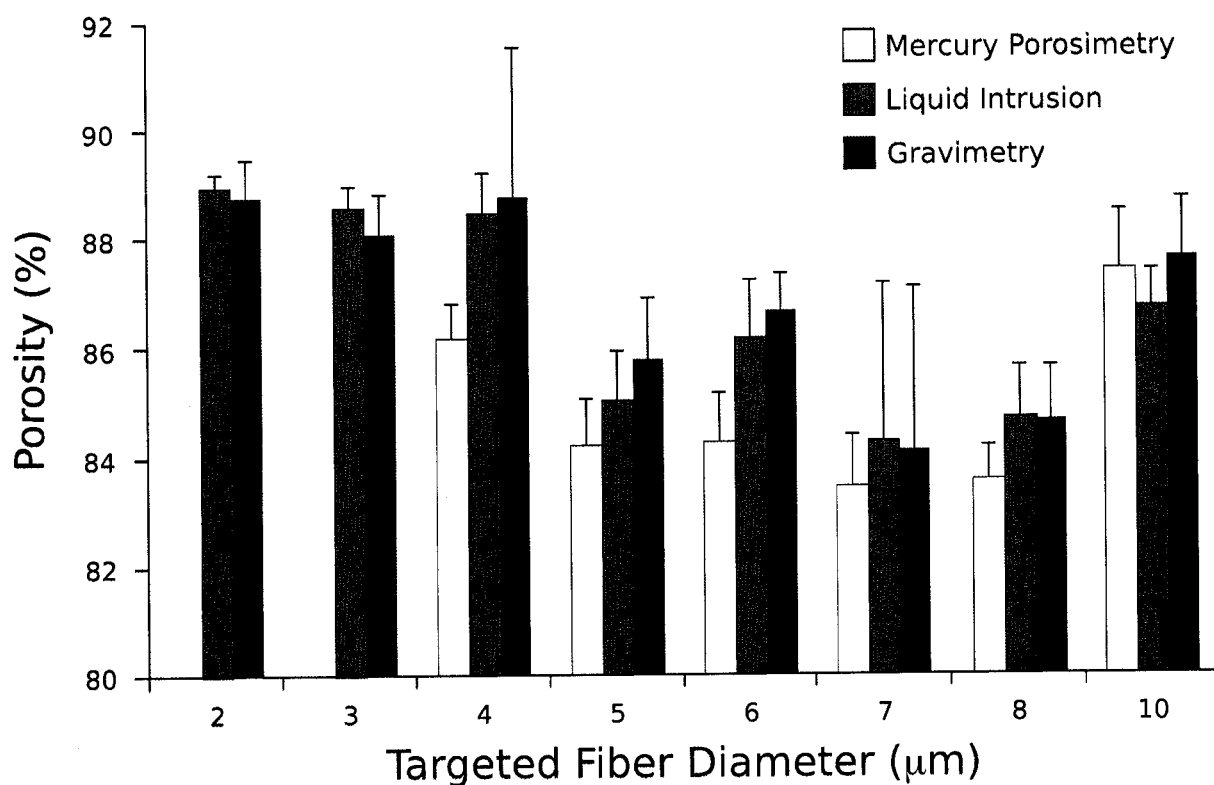
Figure 7-5

Comparison of the porosities of microfiber scaffolds measured using mercury porosimetry, liquid intrusion, and gravimetry. The data represent means of 3 samples with the error bars representing the standard deviations. No significant differences were found between the porosity at each fiber diameter using the three measurement techniques ($p < 0.01$).
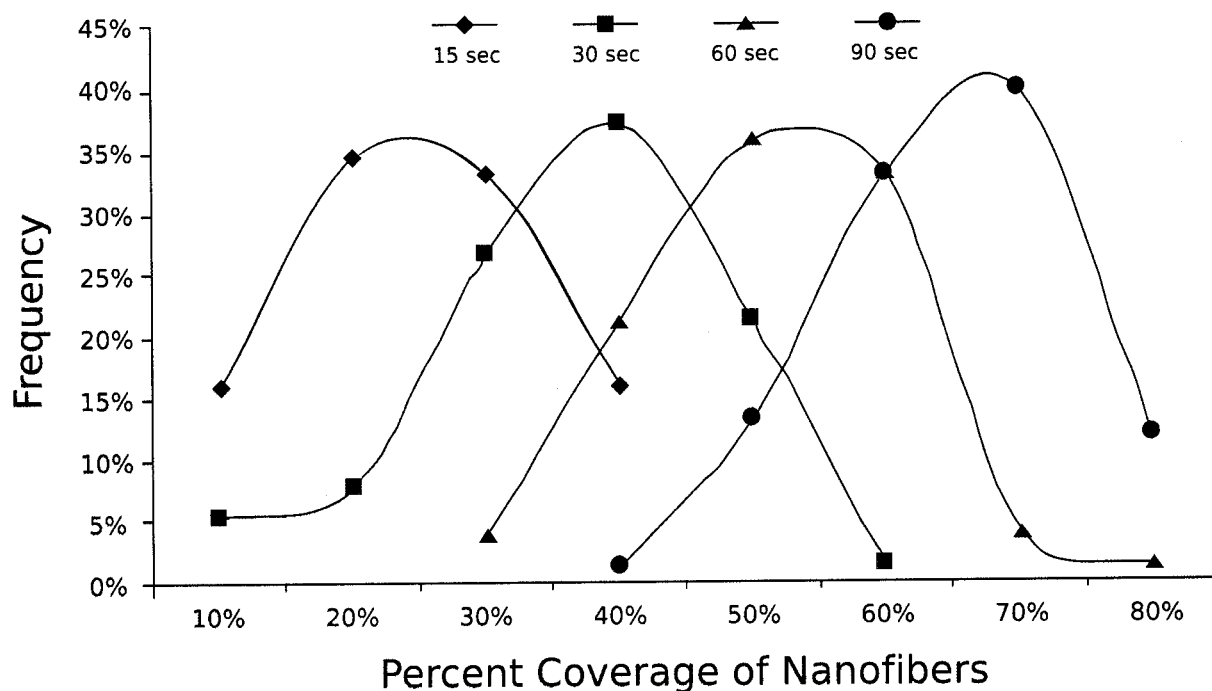
Figure 7-6

Multilayer scaffolds were characterized in terms of the distribution of the coverage of nanofibers on top of an existing microfiber (5 mm fiber diameter) layer. For each layered scaffold condition, 75 randomly selected points were examined; the data represent the frequency of occurrences of a particular coverage of nanofibers. The percent coverage of nanofibers was grouped into 10% bins (e.g., 30% coverage by nanofibers indicates between 21 and 30% coverage).
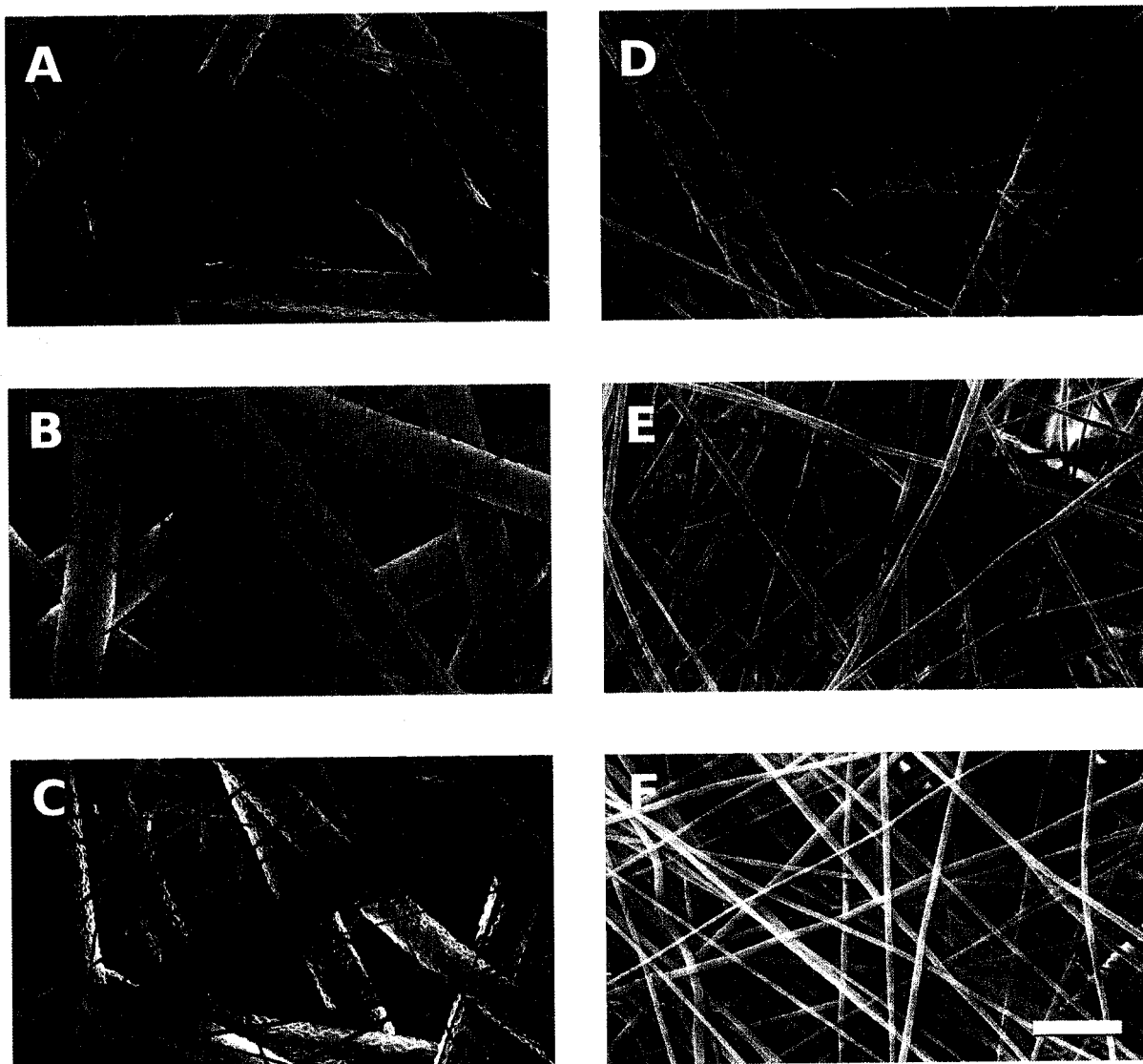
Figure 7-7

Scanning electron micrographs depicting the effect of different periods of nanofiber electrospinning times on the accumulation of nanofibers on top of an existing microfiber layer (5 μm fiber diameter): (A) 15 s electrospin (B) 30 s electrospin (C) 60 s electrospin (D) 90 s electrospin (E) 120 s electrospin and (F) 300 s electrospin. The average fiber diameters are 610 ± 120 nm and 5 μm for the nano- and microfibers, respectively. The scale bar shown applies to all images and is equal to 10 μm.
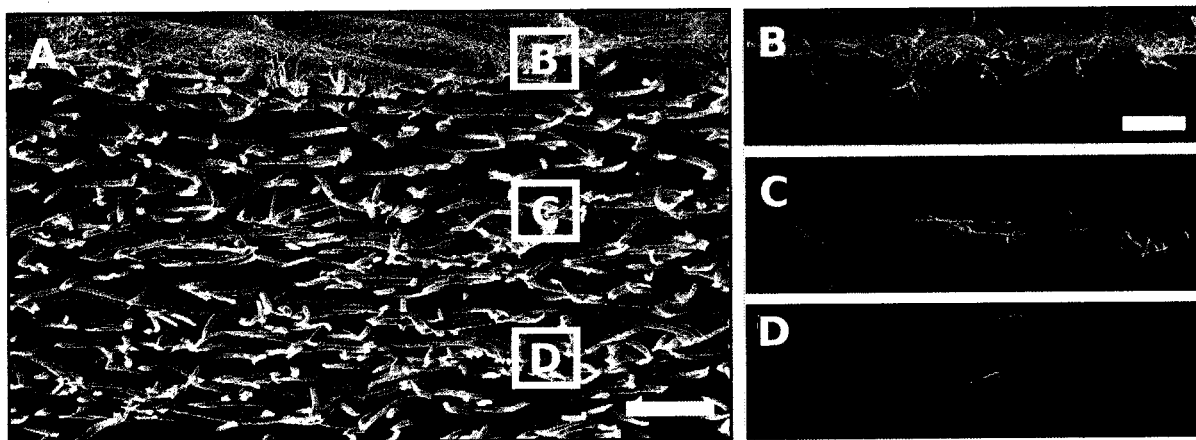
Figure 7-8

Scanning electron micrographs of cross-sections of layered scaffolds generated by sequential electrospinning. (A) Cross-section illustrating (from top to bottom) a nano-micro-nano-micro-nano-microfiber layered scaffold. The white boxes correspond to the nanofiber layers and their respective magnified images shown to the right. (B) Magnification of the nanolayer electrospun for 5 min (C) Magnification of the nanolayer electrospun for 90 sec. (D) Magnification of the nanolayer electrospun for 30 sec. The scale bar shown for A is 100 μm and for B-D is 25 μm. Microfibers are false colored green while nanofibers are false colored yellow to enhance contrast.
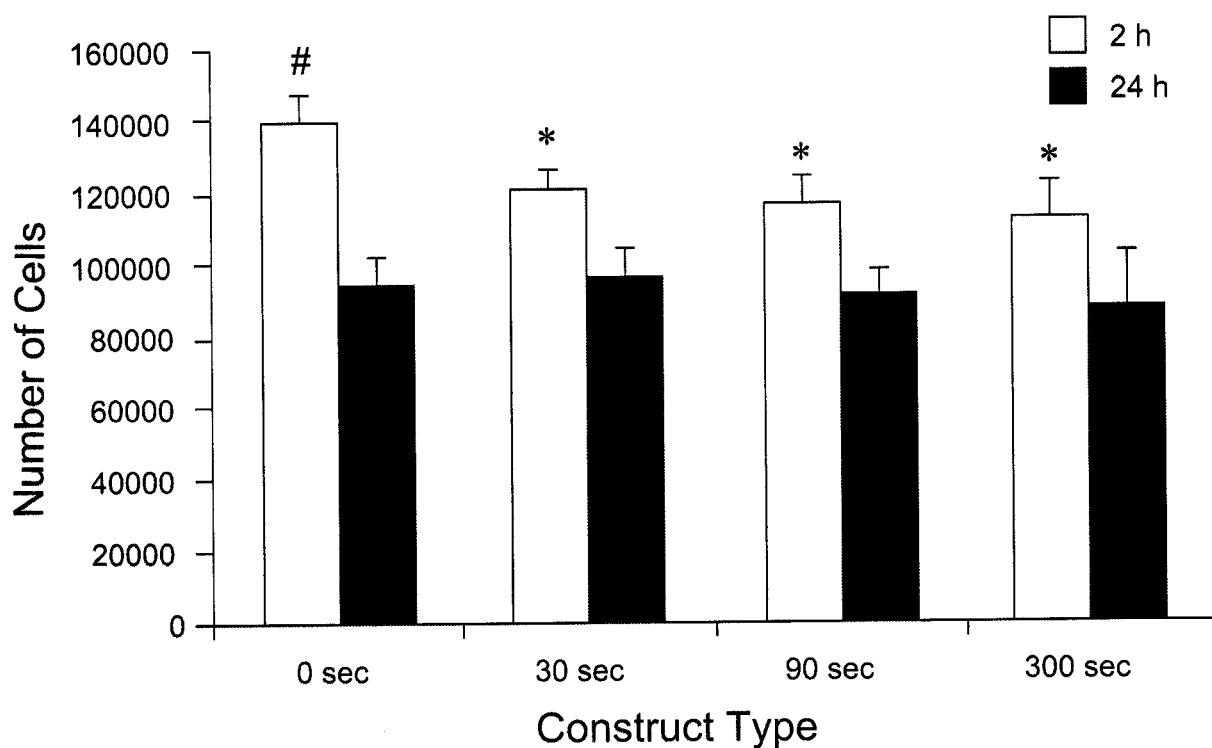
Figure 7-9

Cell attachment on 0, 30, 90, and 300 sec scaffolds at 2 and 24 h post-seeding. The 0, 30, 90, and 300 sec scaffolds are bi-layered scaffolds consisting of a bottom microfiber layer (5 μm) and a top nanofiber layer (600 nm); the numbers correspond to the time used to spin the nanofiber layer. The data represent means of four samples, with error bars representing the standard deviations. A * indicates significance ($p < 0.01$) with respect to the 24 h time point within the group; a # indicates significance ($p < 0.01$) against all groups at both time points.
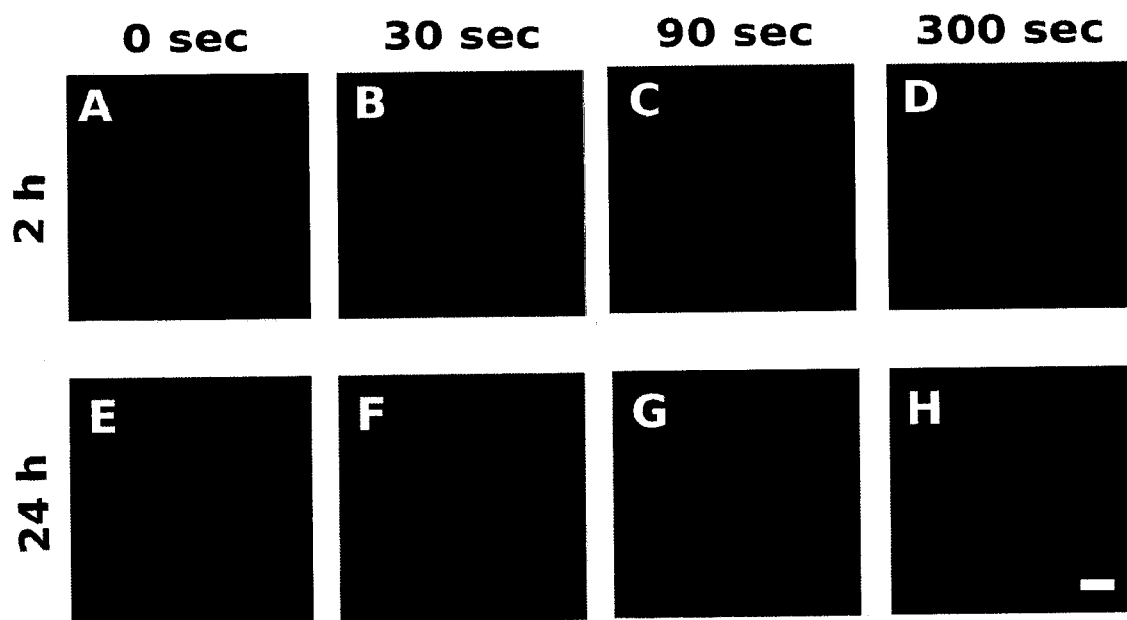
Figure 7-10

Laser scanning confocal microscope images of cells stained for F-actin with rhodamine phallodin at the top surface of 0, 30, 90, and 300 sec scaffolds (A-D and E-H, respectively) at 2 and 24 h (A-D and E-H, respectively). The 0, 30, 90, and 300 sec scaffolds are bi-layered scaffolds consisting of a bottom microfiber layer (5 μm) and a top nanofiber layer (600 nm); the numbers correspond to the time used to spin the nanofiber layer. The scale bar shown is 20 μm and applies to all images.
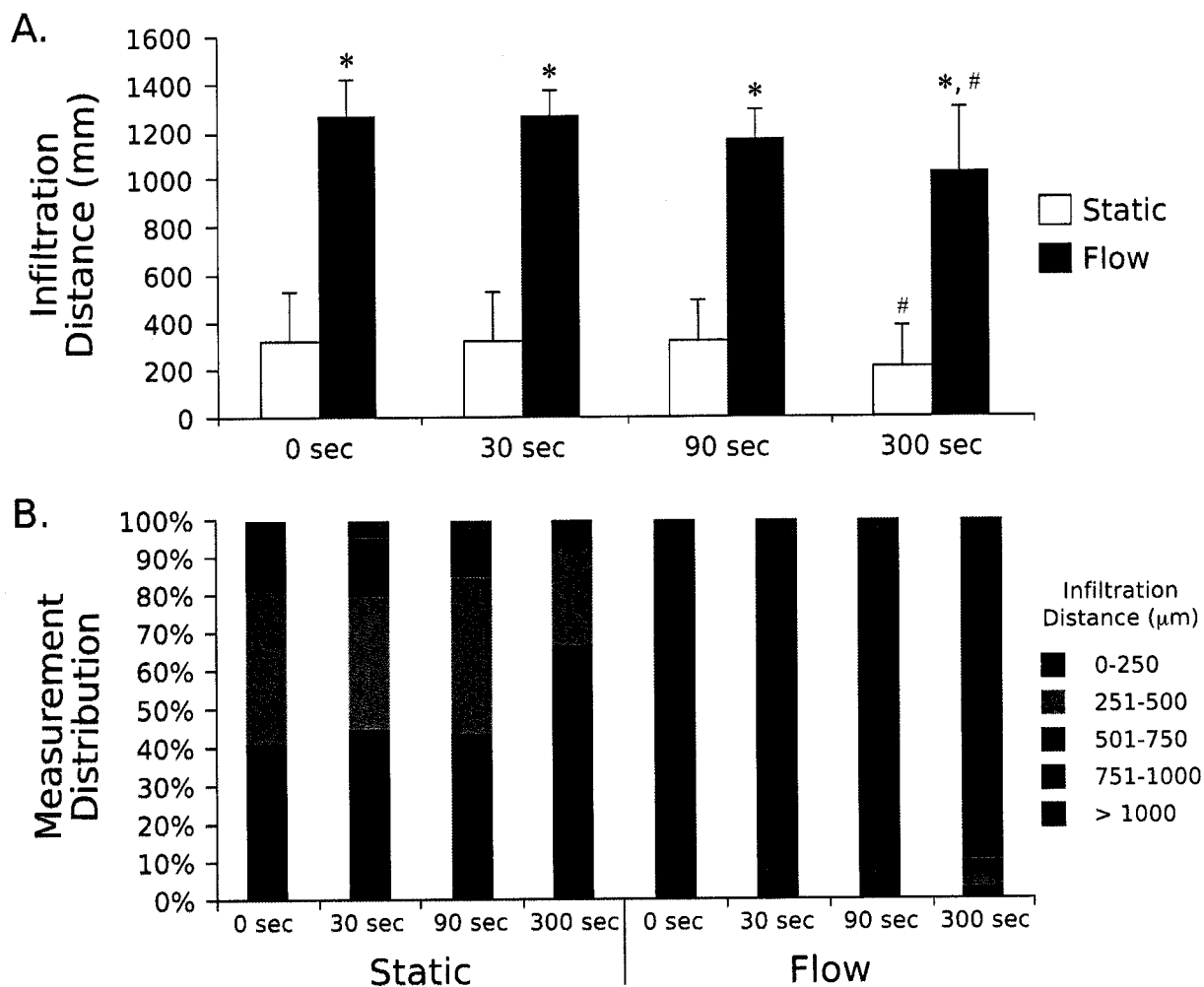
Figure 7-11

(A) Mean infiltration distance traversed by cells on 0, 30, 90, and 300 sec scaffolds under static and flow culture conditions. The 0, 30, 90, and 300 sec scaffolds are bi-layered scaffolds consisting of a bottom microfiber layer (5 μm) and a top nanofiber layer (600 nm); the numbers correspond to the time used to spin the nanofiber layer. The data represent means of four samples, with error bars representing the standard deviations. A * indicates statistical significance between static and flow for each group; a # indicates that for that culture condition, a statistical significance exists between the 300 sec group compared to the other groups (p<0.01). (B) Distribution of the measured infiltration distances separated into bins of 250 μm distances.
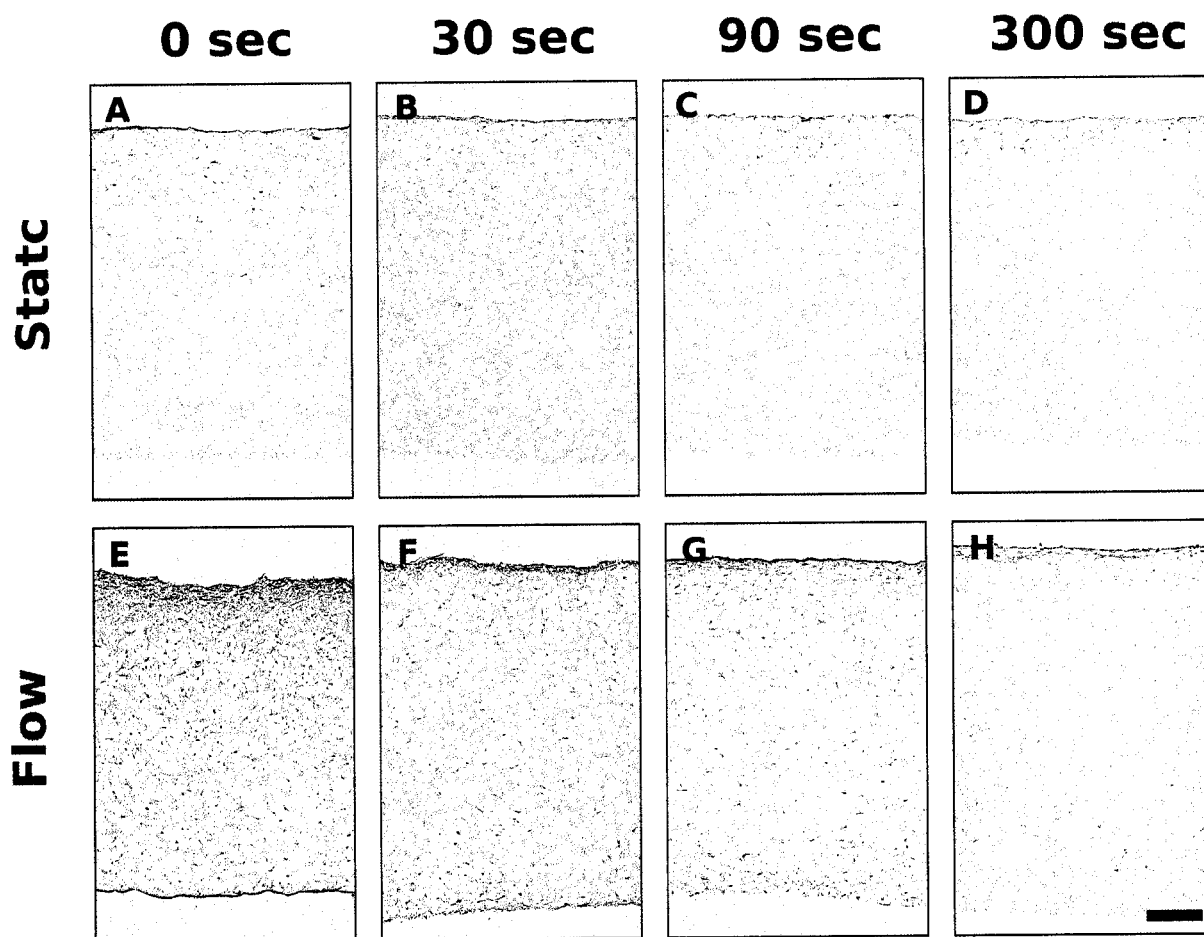
Figure 7-12

Light microscope images (10X) of histological sections stained with hematoxylin and eosin. A-D represents sections from 0, 30, 90, and 300 sec scaffolds, respectively, cultured under static conditions. E-H represents sections from 0, 30, 90, and 300 sec scaffolds, respectively, cultured under flow perfusion conditions. The 0, 30, 90, and 300 sec scaffolds are bi-layered scaffolds consisting of a bottom microfiber layer (5 μm) and a top nanofiber layer (600 nm); the numbers correspond to the time used to spin the nanofiber layer. The scale bar shown is 200 μm and applies to all images shown.

Chapter 8

Conclusions and Future Directions

The overall goal of this research work was to modulate marrow stromal cell (MSC) function and differentiation with the intended aim of creating osteoconductive and osteoinductive tissue engineered constructs capable of promoting bone repair and regeneration in skeletal defects. The specific aims presented in this research allowed for confirmation of the hypothesis that MSC function and differentiation can be modulated using combinations of an *in vitro* generated extracellular matrix, fluid shear stress, scaffold properties, and culture conditions.

Chapter 3 demonstrated that MSCs cultured on non-degradable titanium fiber mesh scaffolds differentiate down an osteoblastic lineage and secrete a bone-like extracellular matrix (ECM) as evidenced by the upregulation in gene expression of bone-specific proteins, growth factors, and ECM molecules. By culturing cells on scaffolds containing this bone-like ECM, gene expression by the MSCs was cogently modulated. Gene expression of osetoblastic markers such as osteopontin and osteocalcin were enhanced and/or prolonged, leading to significant mineralized matrix deposition. Growth factors and ECM molecules were differentially regulated in a manner that contributed to increased MSC osteoblast differentiation.

Chapter 4 elaborated on the idea presented in Chapter 3 by combining the modulation of MSC differentiation using a bone-like ECM with dynamic culture

utilizing a flow perfusion bioreactor. Previous work has shown that fluid shear stresses alone promote MSC osteoblastic differentiation. By combining these two parameters, a synergistic effect between these two factors was observed on mineralized matrix deposition that was attributed to the bioactivity of the ECM. Interestingly, this effect was observed only when the culture medium contained the osteogenic supplement, dexamethasone. The use of a flow perfusion bioreactor also enhances the spatial distribution of cells and matrix, thereby facilitating the production of three-dimensional tissue engineered constructs.

Chapter 5 sought to determine the osteoinductive capacity and angiogenicity of the bone-like ECM in an ectopic site using a rodent model. While no bone formation was observed, there appeared to be increasing angiogenesis with increasing ECM. This study indicated that the requirements for *de novo* bone formation *in vivo* at an ectopic site are difficult to achieve and more studies are required to determine the conditions and parameters necessary for generating an osteoinductive extracellular matrix.

The results of the research work described in these chapters reveal that cell-secreted ECM holds tremendous potential as a tissue engineering strategy to promote bone healing. Furthermore, combining this strategy with a flow perfusion bioreactor generates truly three-dimensional tissue engineering constructs. The lack of induced bone formation in Chapter 5 highlights the challenges of translating from *in vitro* experiments to the *in vivo* setting as the number of controlled variables is

reduced. An investigation as to whether demineralizing the constructs (similar to that of demineralized bone matrices) prior to implantation would increase its osteoinductive potential is an approach that warrants further exploration. Although the ECM alone was not osteoinductive, a strategy that could prove effective is the addition of a cellular component to the ECM prior to implantation. As well, there still remains to determine the efficacy of ECM-constructs in an orthotopic site (i.e., a more clincically relevant location).

A basic analysis of the ECM components and various genes expressed by MSCs was provided in this research, but a more thorough analysis of the cell-ssecreted ECM would aid immensely in the optimization of the strategy presented in this thesis. A proteomic analysis of the ECM as a function of time would reveal the amounts of growth factors and proteins deposited by the cells during the course of culture. This information would greatly assist in developing a strategy that would allow for the controlled production of extracellular matrix constructs prior to implantation. These studies will be performed using electrospun polymer scaffolds, which was the subject of Chapters 7.

The transition to *in vivo* models and ultimately clinical applications provided the impetus for transitioning into using a biodegradable polymer as a scaffold material used to support cell attachment and ECM deposition. Chapter 7 introduced electrospinning, a technique used to create non-woven fiber meshes scaffolds with tunable fiber diameters and pore sizes. Poly(ε-caprolactone) scaffolds were shown

to promote cell attachment and were conducive for MSC osteoblastic differentiation. The versatility of the electrospinning technique was used to fabricate multi-layered scaffolds containing different fiber diameters. Future studies can investigate the effect of nanofibers on MSC differentiation and ECM deposition.

REFERENCES

1. Defranoux, N.A., et al., In silico modeling and simulation of bone biology: a proposal. J Bone Miner Res, 2005. **20**(7): p. 1079-84.

2. Stains, J.P. and R. Civitelli, Cell-cell interactions in regulating osteogenesis and osteoblast function. Birth Defects Res C Embryo Today, 2005. **75**(1): p. 72-80.

3. Sommerfeldt, D.W. and C.T. Rubin, Biology of bone and how it orchestrates the form and function of the skeleton. Eur Spine J, 2001. **10 Suppl 2**: p. S86-95.

4. Robins, S.P. and J.D. Brady, Collagen Cross-Linking and Metabolism. Principles of Bone Biology, ed. J. Bilezikian, L. Raisz, and G. Rodan. Vol. 1. 2002.

5. Robey, P.G., Bone Matrix Proteoglycans and Glycoproteins. Principles of Bone Biology, ed. J. Bilezikian, L. Raisz, and G. Rodan. Vol. 1. 2002.

6. Quarles, L.D., et al., Distinct proliferative and differentiated stages of murine MC3T3-E1 cells in culture: an in vitro model of osteoblast development. J Bone Miner Res, 1992. **7**(6): p. 683-92.

7. Lian, J.B., et al., Regulatory controls for osteoblast growth and differentiation: role of Runx/Cbfa/AML factors. Crit Rev Eukaryot Gene Expr, 2004. **14**(1-2): p. 1-41.

8. Tondreau, T., et al., Bone marrow-derived mesenchymal stem cells already express specific neural proteins before any differentiation. Differentiation, 2004. **72**(7): p. 319-26.

9. Ratajczak, M.Z., et al., Heterogeneous populations of bone marrow stem cells--are we spotting on the same cells from the different angles? Folia Histochem Cytobiol, 2004. **42**(3): p. 139-46.

10. Jorgensen, C., J. Gordeladze, and D. Noel, Tissue engineering through autologous mesenchymal stem cells. Current Opinion in Biotechnology, 2004. **15**: p. 406-410.

11. Filanti, C., et al., The expression of metalloproteinase-2, -9, and -14 and of tissue inhibitors-1 and -2 is developmentally modulated during osteogenesis in vitro, the mature osteoblastic phenotype expressing metalloproteinase-14. J Bone Miner Res, 2000. **15**(11): p. 2154-68.

12. zur Nieden, N.I., G. Kempka, and H.J. Ahr, *In vitro* differentiation of embryonic stem cells into mineralized osteoblasts. Differentiation, 2003. **71**(1): p. 18-27.

13. Kim, Y.J., et al., Bone morphogenetic protein-2-induced alkaline phosphatase expression is stimulated by Dlx5 and repressed by Msx2. J Biol Chem, 2004. **279**(49): p. 50773-80.

14. Owen, T.A., et al., Progressive development of the rat osteoblast phenotype *in vitro*: reciprocal relationships in expression of genes associated with osteoblast proliferation and differentiation during formation of the bone extracellular matrix. J Cell Physiol, 1990. **143**(3): p. 420-30.

15. Lian, J.B., et al., Osteocalcin gene promoter: unlocking the secrets for regulation of osteoblast growth and differentiation. J Cell Biochem Suppl, 1998. **30-31**: p. 62-72.

16. Kojima, H., T. Uede, and T. Uemura, *In vitro* and *in vivo* effects of the overexpression of osteopontin on osteoblast differentiation using a recombinant adenoviral vector. J Biochem (Tokyo), 2004. **136**(3): p. 377-86.

17. Jundt, G., et al., Osteonectin--a differentiation marker of bone cells. Cell Tissue Res, 1987. **248**(2): p. 409-15.

18. Seibel, M.J., et al., Biochemical Markers of Bone Metabolism. Principles of Bone Biology, ed. J. Bilezikian, L. Raisz, and G. Rodan. Vol. 1. 2002.

19. Jager, M., et al., Influence of different culture solutions on osteoblastic differentiation in cord blood and bone marrow derived progenitor cells. Biomed Tech (Berl), 2003. **48**(9): p. 241-4.

20. Worster, A.A., et al., Effect of transforming growth factor beta1 on chondrogenic differentiation of cultured equine mesenchymal stem cells. Am J Vet Res, 2000. **61**(9): p. 1003-10.

21. Peter, S.J., et al., Osteoblastic phenotype of rat marrow stromal cells cultured in the presence of dexamethasone, beta-glycerolphosphate, and L-ascorbic acid. J Cell Biochem, 1998. **71**(1): p. 55-62.

22. Holtorf, H.L., J.A. Jansen, and A.G. Mikos, Flow perfusion culture induces the osteoblastic differentiation of marrow stroma cell-scaffold constructs in the absence of dexamethasone. J Biomed Mater Res A, 2005. **72**(3): p. 326-34.

23. Cheng, S.L., et al., Differentiation of human bone marrow osteogenic stromal cells *in vitro*: induction of the osteoblast phenotype by dexamethasone. Endocrinology, 1994. **134**(1): p. 277-86.

24. Ong, J.L., D.L. Carnes, and A. Sogal, Effect of transforming growth factor-beta on osteoblast cells cultured on 3 different hydroxyapatite surfaces. International Journal of Oral & Maxillofacial Implants, 1999. **14**(2): p. 217-225.

25. Rosen, C.J., Insulin-like growth factor I and bone mineral density: experience from animal models and human observational studies. Best Pract Res Clin Endocrinol Metab, 2004. **18**(3): p. 423-35.

26. Kroese-Deutman, H.C., et al., Bone inductive properties of rhBMP-2 loaded porous calcium phosphate cement implants inserted at an ectopic site in rabbits. Biomaterials, 2005. **26**(10): p. 1131-8.

27. Parikh, S.N., Bone graft substitutes: past, present, future. J Postgrad Med, 2002. **48**(2): p. 142-8.

28. Linkhart, T.A., S. Mohan, and D.J. Baylink, Growth factors for bone growth and repair: IGF, TGF beta and BMP. Bone, 1996. **19**(1 Suppl): p. 1S-12S.

29. Joyce, M.E., et al., Transforming growth factor-beta and the initiation of chondrogenesis and osteogenesis in the rat femur. J Cell Biol, 1990. **110**(6): p. 2195-207.

30. Holland, T.A., Y. Tabata, and A.G. Mikos, *In vitro* release of transforming growth factor-beta 1 from gelatin microparticles encapsulated in biodegradable, injectable oligo(poly(ethylene glycol) fumarate) hydrogels. J Control Release, 2003. **91**(3): p. 299-313.

31. Lu, L., M.J. Yaszemski, and A.G. Mikos, TGF-beta1 release from biodegradable polymer microparticles: its effects on marrow stromal osteoblast function. J Bone Joint Surg Am, 2001. **83-A Suppl** 1(Pt 2): p. S82-91.

32. Centrella, M., et al., Transforming growth factor-beta gene family members and bone. Endocr Rev, 1994. **15**(1): p. 27-39.

33. Talley-Ronsholdt, D.J., E. Lajiness, and K. Nagodawithana, Transforming growth factor-beta inhibition of mineralization by neonatal rat osteoblasts in monolayer and collagen gel culture. *In vitro* Cell Dev Biol Anim, 1995. **31**(4): p. 274-82.

34. Reddi, A.H. and N.S. Cunningham, Recent progress in bone induction by osteogenin and bone morphogenetic proteins: challenges for biomechanical and tissue engineering. J Biomech Eng, 1991. **113**(2): p. 189-90.

35. Yuan, H., et al., Bone morphogenetic protein and ceramic-induced osteogenesis. J Mater Sci Mater Med, 1998. **9**(12): p. 717-21.

36. Zou, X., et al., Stimulation of porcine bone marrow stromal cells by hyaluronan, dexamethasone and rhBMP-2. Biomaterials, 2004. **25**(23): p. 5375-85.

37. Park, Y.J., et al., Immobilization of bone morphogenetic protein-2 onto a nanofibrous chitosan membrane for enhanced guided bone regeneration. Biotechnol Appl Biochem, 2005.

38. Kapur, S., et al., Fluid shear stress synergizes with insulin-like growth factor-I (IGF-I) on osteoblast proliferation through integrin-dependent activation of IGF-I mitogenic signaling pathway. J Biol Chem, 2005. **280**(20): p. 20163-70.

39. Street, J., et al., Vascular endothelial growth factor stimulates bone repair by promoting angiogenesis and bone turnover. Proc Natl Acad Sci U S A, 2002. **99**(15): p. 9656-61.

40. Furumatsu, T., et al., Vascular endothelial growth factor principally acts as the main angiogenic factor in the early stage of human osteoblastogenesis. J Biochem (Tokyo), 2003. **133**(5): p. 633-9.

41. Deckers, M.M., et al., Expression of vascular endothelial growth factors and their receptors during osteoblast differentiation. Endocrinology, 2000. **141**(5): p. 1667-74.

42. Maes, C., et al., Impaired angiogenesis and endochondral bone formation in mice lacking the vascular endothelial growth factor isoforms VEGF164 and VEGF188. Mech Dev, 2002. **111**(1-2): p. 61-73.

43. Cowan, C.M., et al., Bone morphogenetic protein 2 and retinoic acid accelerate *in vivo* bone formation, osteoclast recruitment, and bone turnover. Tissue Eng, 2005. **11**(3-4): p. 645-58.

44. Huffer, W.E., Morphology and biochemistry of bone remodeling: possible control by vitamin D, parathyroid hormone, and other substances. Lab Invest, 1988. **59**(4): p. 418-42.

45. Gabbitas, B. and E. Canalis, Retinoic acid regulates the expression of insulin-like growth factors I and II in osteoblasts. J Cell Physiol, 1997. **172**(2): p. 253-64.

46. Leboy, P.S., et al., Dexamethasone induction of osteoblast mRNAs in rat marrow stromal cell cultures. J Cell Physiol, 1991. **146**(3): p. 370-8.

47. Rickard, D.J., I. Kazhdan, and P.S. Leboy, Importance of 1,25-dihydroxyvitamin D3 and the nonadherent cells of marrow for osteoblast differentiation from rat marrow stromal cells. Bone, 1995. **16**(6): p. 671-8.

48. Kroll, M.H., Parathyroid hormone temporal effects on bone formation and resorption. Bull Math Biol, 2000. **62**(1): p. 163-88.

49. Wake, M.C., P.K. Gupta, and A.G. Mikos, Fabrication of pliable biodegradable polymer foams to engineer soft tissues. Cell Transplant, 1996. **5**(4): p. 465-73.

50. Gomes, M.E., et al., Effect of flow perfusion on the osteogenic differentiation of bone marrow stromal cells cultured on starch-based three-dimensional scaffolds. J Biomed Mater Res A, 2003. **67**(1): p. 87-95.

51. Ma, Z., et al., Potential of nanofiber matrix as tissue-engineering scaffolds. Tissue Eng, 2005. **11**(1-2): p. 101-9.

52. Hutmacher, D.W., et al., Mechanical properties and cell cultural response of polycaprolactone scaffolds designed and fabricated via fused deposition modeling. J Biomed Mater Res, 2001. **55**(2): p. 203-16.

53. Williams, J.M., et al., Bone tissue engineering using polycaprolactone scaffolds fabricated via selective laser sintering. Biomaterials, 2005. **26**(23): p. 4817-27.

54. LeGeros, R.Z., Properties of osteoconductive biomaterials: calcium phosphates. Clin Orthop Relat Res, 2002(395): p. 81-98.

55. de Ruijter, J.E., et al., Analysis of integrin expression in U2OS cells cultured on various calcium phosphate ceramic substrates. Tissue Eng, 2001. **7**(3): p. 279-89.

56. Rodrigues, C.V., et al., Characterization of a bovine collagen-hydroxyapatite composite scaffold for bone tissue engineering. Biomaterials, 2003. **24**(27): p. 4987-97.

57. Sharma, B. and J.H. Elisseeff, Engineering structurally organized cartilage and bone tissues. Ann Biomed Eng, 2004. **32**(1): p. 148-59.

58. Liu, X. and P.X. Ma, Polymeric scaffolds for bone tissue engineering. Ann Biomed Eng, 2004. **32**(3): p. 477-86.

59. Andriano, K.P., Y. Tabata, and J. Heller, *In vitro* and *in vivo* comparison of bulk and surface hydrolysis in absorbable polymer scaffolds for tissue engineering. J Biomed Mater Res, 1999. **48**(5): p. 602-612.

60. Daniels, A.U., et al., Evaluation of absorbable poly(ortho esters) for use in surgical implants. J Appl Biomater, 1994. **5**(1): p. 51-64.

61. Rohner, D., et al., *In vivo* efficacy of bone-marrow-coated polycaprolactone scaffolds for the reconstruction of orbital defects in the pig. J Biomed Mater Res B Appl Biomater, 2003. **66**(2): p. 574-80.

62. Payne, R.G., et al., Development of an injectable, in situ crosslinkable, degradable polymeric carrier for osteogenic cell populations. Part 3. Proliferation and differentiation of encapsulated marrow stromal osteoblasts cultured on crosslinking poly(propylene fumarate). Biomaterials, 2002. **23**(22): p. 4381-7.

63. Fisher, J.P., et al., Synthesis and properties of photocross-linked poly(propylene fumarate) scaffolds. J Biomater Sci Polym Ed, 2001. **12**(6): p. 673-87.

64. Fisher, J.P., et al., Soft and hard tissue response to photocrosslinked poly(propylene fumarate) scaffolds in a rabbit model. J Biomed Mater Res, 2002. **59**(3): p. 547-56.

65. Peter, S.J., et al., Marrow stromal osteoblast function on a poly(propylene fumarate)/beta-tricalcium phosphate biodegradable orthopaedic composite. Biomaterials, 2000. **21**(12): p. 1207-13.

66. Williamson, M.R. and A.G. Coombes, Gravity spinning of polycaprolactone fibres for applications in tissue engineering. Biomaterials, 2004. **25**(3): p. 459-65.

67. Mo, X.M., et al., Electrospun P(LLA-CL) nanofiber: a biomimetic extracellular matrix for smooth muscle cell and endothelial cell proliferation. Biomaterials, 2004. **25**(10): p. 1883-90.

68. Buchko, C.J., et al., Processing and microstructural characterization of porous biocompatible protein polymer thin films. Polymer, 1999. **40**: p. 7397-7407.

69. Doshi, J. and D.H. Reneker, Electrospinning process and applications of electrospun fibers. Journal of Electrostatics, 1995. **35**(2-3): p. 151-160.

70. Venugopal, J. and S. Ramakrishna, Applications of polymer nanofibers in biomedicine and biotechnology. Appl Biochem Biotechnol, 2005. **125**(3): p. 147-58.

71. Fridrikh, S.V., et al., Controlling the fiber diameter during electrospinning. Phys Rev Lett, 2003. **90**(14): p. 144502.

72. Lim, T.C., et al., Recent advances in tissue engineering applications of electrospun nanofibers. Materials Technology, 2004. **19**(1): p. 20-27.

73. Zeng, J., et al., Biodegradable electrospun fibers for drug delivery. J Control Release, 2003. **92**(3): p. 227-31.

74. Lee, C.H., et al., Nanofiber alignment and direction of mechanical strain affect the ECM production of human ACL fibroblast. Biomaterials, 2005. **26**(11): p. 1261-70.

75. Li, D. and Y.N. Xia, Electrospinning of nanofibers: Reinventing the wheel? Advanced Materials, 2004. **16**(14): p. 1151-1170.

76. Sikavitsas, V.I., et al., Flow perfusion enhances the calcified matrix deposition of marrow stromal cells in biodegradable nonwoven fiber mesh scaffolds. Ann Biomed Eng, 2005. **33**(1): p. 63-70.

77. Yu, X., et al., Bioreactor-based bone tissue engineering: the influence of dynamic flow on osteoblast phenotypic expression and matrix mineralization. Proc Natl Acad Sci U S A, 2004. **101**(31): p. 11203-8.

78. Cartmell, S.H., et al., Effects of medium perfusion rate on cell-seeded three-dimensional bone constructs *in vitro*. Tissue Eng, 2003. **9**(6): p. 1197-203.

79. Botchwey, E.A., et al., Tissue engineered bone: measurement of nutrient transport in three-dimensional matrices. J Biomed Mater Res A, 2003. **67**(1): p. 357-67.

80. Sikavitsas, V.I., G.N. Bancroft, and A.G. Mikos, Formation of three-dimensional cell/polymer constructs for bone tissue engineering in a spinner flask and a rotating wall vessel bioreactor. J Biomed Mater Res, 2002. **62**(1): p. 136-48.

81. Freed, L.E., et al., Chondrogenesis in a cell-polymer-bioreactor system. Exp Cell Res, 1998. **240**(1): p. 58-65.

82. Saini, S. and T.M. Wick, Concentric cylinder bioreactor for production of tissue engineered cartilage: effect of seeding density and hydrodynamic loading on construct development. Biotechnol Prog, 2003. **19**(2): p. 510-21.

83. Bancroft, G.N., V.I. Sikavitsas, and A.G. Mikos, Design of a flow perfusion bioreactor system for bone tissue-engineering applications. Tissue Eng, 2003. **9**(3): p. 549-54.

84. Goldstein, A.S., et al., Effect of convection on osteoblastic cell growth and function in biodegradable polymer foam scaffolds. Biomaterials, 2001. **22**(11): p. 1279-88.

85. Glowacki, J., S. Mizuno, and J.S. Greenberger, Perfusion enhances functions of bone marrow stromal cells in three-dimensional culture. Cell Transplant, 1998. **7**(3): p. 319-26.

86. Bujia, J., et al., Engineering of cartilage tissue using bioresorbable polymer fleeces and perfusion culture. Acta Otolaryngol, 1995. **115**(2): p. 307-10.

87. Yoshimoto, H., et al., A biodegradable nanofiber scaffold by electrospinning and its potential for bone tissue engineering. Biomaterials, 2003. **24**(12): p. 2077-82.

88. Owan, I., et al., Mechanotransduction in bone: osteoblasts are more responsive to fluid forces than mechanical strain. Am J Physiol, 1997. **273**(3 Pt 1): p. C810-5.

89. Buckwalter, J.A., et al., Bone Biology .1. Structure, Blood-Supply, Cells, Matrix, and Mineralization. Journal of Bone and Joint Surgery-American Volume, 1995. **77A**(8): p. 1256-1275.

90. Norvell, S.M., et al., Fluid shear stress induces beta-catenin signaling in osteoblasts. Calcif Tissue Int, 2004. **75**(5): p. 396-404.

91. Bancroft, G.N., et al., Fluid flow increases mineralized matrix deposition in 3D perfusion culture of marrow stromal osteloblasts in a dose-dependent manner. Proceedings of the National Academy of Sciences of the United States of America, 2002. **99**(20): p. 12600-12605.

92. Johnson, D.L., T.N. McAllister, and J.A. Frangos, Fluid flow stimulates rapid and continuous release of nitric oxide in osteoblasts. Am J Physiol, 1996. **271**(1 Pt 1): p. E205-8.

93. Bakker, A.D., et al., The production of nitric oxide and prostaglandin E-2 by primary bone cells is shear stress dependent. Journal of Biomechanics, 2001. **34**(5): p. 671-677.

94. You, J., et al., Osteopontin gene regulation by oscillatory fluid flow via intracellular calcium mobilization and activation of mitogen-activated protein kinase in MC3T3-E1 osteoblasts. J Biol Chem, 2001. **276**(16): p. 13365-71.

95. Botchwey, E.A., et al., Quantitative analysis of three-dimensional fluid flow in rotating bioreactors for tissue engineering. J Biomed Mater Res A, 2004. **69**(2): p. 205-15.

96. Sikavitsas, V.I., et al., Mineralized matrix deposition by marrow stromal osteoblasts in 3D perfusion culture increases with increasing fluid shear forces. Proc Natl Acad Sci U S A, 2003. **100**(25): p. 14683-8.

97. Caplan, A.I. and J.E. Dennis, Mesenchymal stem cells as trophic mediators. J Cell Biochem, 2006. **98**(5): p. 1076-84.

98. Xu, M., et al., Differentiation of bone marrow stromal cells into the cardiac phenotype requires intercellular communication with myocytes. Circulation, 2004. **110**(17): p. 2658-65.

99. Wang, P.P., et al., Expression of hepatocyte-like phenotypes in bone marrow stromal cells after HGF induction. Biochem Biophys Res Commun, 2004. **320**(3): p. 712-6.

100. Caddick, J., et al., Phenotypic and functional characteristics of mesenchymal stem cells differentiated along a Schwann cell lineage. Glia, 2006. **54**(8): p. 840-9.

101. Nagaya, N., et al., Transplantation of mesenchymal stem cells improves cardiac function in a rat model of dilated cardiomyopathy. Circulation, 2005. **112**(8): p. 1128-35.

102. Castano-Izquierdo, H., et al., Pre-culture period of mesenchymal stem cells in osteogenic media influences their *in vivo* bone forming potential. J Biomed Mater Res A, 2007. **82**(1): p. 129-38.

103. Oliveira, J.M., et al., Novel hydroxyapatite/chitosan bilayered scaffold for osteochondral tissue-engineering applications: Scaffold design and its performance when seeded with goat bone marrow stromal cells. Biomaterials, 2006. **27**(36): p. 6123-37.

104. Chen, G., et al., The use of a novel PLGA fiber/collagen composite web as a scaffold for engineering of articular cartilage tissue with adjustable thickness. J Biomed Mater Res A, 2003. **67**(4): p. 1170-80.

105. Richardson, T.P., et al., Polymeric system for dual growth factor delivery. Nat Biotechnol, 2001. **19**(11): p. 1029-34.

106. Bashkin, P., et al., Basic fibroblast growth factor binds to subendothelial extracellular matrix and is released by heparitinase and heparin-like molecules. Biochemistry, 1989. **28**(4): p. 1737-43.

107. Schonherr, E. and H.J. Hausser, Extracellular matrix and cytokines: a functional unit. Dev Immunol, 2000. **7**(2-4): p. 89-101.

108. Datta, N., et al., Effect of bone extracellular matrix synthesized *in vitro* on the osteoblastic differentiation of marrow stromal cells. Biomaterials, 2005. **26**(9): p. 971-977.

109. Datta, N., et al., *In vitro* generated extracellular matrix and fluid shear stress synergistically enhance 3D osteoblastic differentiation. Proc Natl Acad Sci U S A, 2006. **103**(8): p. 2488-93.

110. Gomes, M.E., et al., *In vitro* localization of bone growth factors in constructs of biodegradable scaffolds seeded with marrow stromal cells and cultured in a flow perfusion bioreactor. Tissue Eng, 2006. **12**(1): p. 177-88.

111. Livak, K.J. and T.D. Schmittgen, Analysis of relative gene expression data using real-time quantitative PCR and the 2(-Delta Delta C(T)) Method. Methods, 2001. **25**(4): p. 402-8.

112. Fogel, P., et al., Inferential, robust non-negative matrix factorization analysis of microarray data. Bioinformatics, 2007. **23**(1): p. 44-9.

113. Monticone, M., et al., Gene expression profile of human bone marrow stromal cells determined by restriction fragment differential display analysis. J Cell Biochem, 2004. **92**(4): p. 733-44.

114. Frasor, J., et al., Profiling of estrogen up- and down-regulated gene expression in human breast cancer cells: insights into gene networks and pathways underlying estrogenic control of proliferation and cell phenotype. Endocrinology, 2003. **144**(10): p. 4562-74.

115. Marvanova, M., M. Lakso, and G. Wong, Identification of genes regulated by memantine and MK-801 in adult rat brain by cDNA microarray analysis. Neuropsychopharmacol, 2004. **29**(6): p. 1070-9.

116. Choi, J.Y., et al., Expression patterns of bone-related proteins during osteoblastic differentiation in MC3T3-E1 cells. J Cell Biochem, 1996. **61**(4): p. 609-18.

117. Hoshi, K., et al., The primary calcification in bones follows removal of decorin and fusion of collagen fibrils. J Bone Miner Res, 1999. **14**(2): p. 273-80.

118. Argiro, L., et al., Mepe, the gene encoding a tumor-secreted protein in oncogenic hypophosphatemic osteomalacia, is expressed in bone. Genomics, 2001. **74**(3): p. 342-51.

119. Franz-Odendaal, T.A., B.K. Hall, and P.E. Witten, Buried alive: how osteoblasts become osteocytes. Dev Dyn, 2006. **235**(1): p. 176-90.

120. Kondo, H., et al., Temporal changes of mRNA expression of matrix proteins and parathyroid hormone and parathyroid hormone-related protein (PTH/PTHrP) receptor in bone development. J Bone Miner Res, 1997. **12**(12): p. 2089-97.

121. Ninomiya, K., et al., Osteoclastic activity induces osteomodulin expression in osteoblasts. Biochem Biophys Res Commun, 2007. **362**(2): p. 460-6.

122. Sommarin, Y., et al., Osteoadherin, a cell-binding keratan sulfate proteoglycan in bone, belongs to the family of leucine-rich repeat proteins of the extracellular matrix. J Biol Chem, 1998. **273**(27): p. 16723-9.

123. Aubin, J.E., et al., Osteoblast and chondroblast differentiation. Bone, 1995. **17**(2 Suppl): p. 77S-83S.

124. Franceschi, R.T., The developmental control of osteoblast-specific gene expression: role of specific transcription factors and the extracellular matrix environment. Crit Rev Oral Biol Med, 1999. **10**(1): p. 40-57.

125. Mauney, J.R., et al., Osteogenic differentiation of human bone marrow stromal cells on partially demineralized bone scaffolds *in vitro*. Tissue Eng, 2004. **10**(1-2): p. 81-92.

126. Lieberman, J.R., A. Daluiski, and T.A. Einhorn, The role of growth factors in the repair of bone. Biology and clinical applications. J Bone Joint Surg Am, 2002. **84-A**(6): p. 1032-44.

127. Lind, M., Growth factors: possible new clinical tools. A review. Acta Orthop Scand, 1996. **67**(4): p. 407-17.

128. Huang, Z., et al., The Sequential Expression Profiles of Growth Factors from Osteroprogenitors to Osteoblasts *In vitro*. Tissue Eng, 2007.

129. Bi, Y., et al., Extracellular matrix proteoglycans control the fate of bone marrow stromal cells. J Biol Chem, 2005.

130. Schiavi, S.C., Bone talk. Nat Genet, 2006. **38**(11): p. 1230-1.

131. Narayanan, K., et al., Differentiation of embryonic mesenchymal cells to odontoblast-like cells by overexpression of dentin matrix protein 1. Proc Natl Acad Sci U S A, 2001. **98**(8): p. 4516-21.

132. Rosso, F., et al., Smart materials as scaffolds for tissue engineering. J Cell Physiol, 2005. **203**(3): p. 465-70.

133. Hedbom, E. and D. Heinegard, Binding of fibromodulin and decorin to separate sites on fibrillar collagens. J Biol Chem, 1993. **268**(36): p. 27307-12.

134. Matsuura, T., et al., Differential gene expression of collagen-binding small leucin-rich proteoglycans and lysyl hydroxylases, during mineralization by MC3T3-E1 cells cultured on titanium implant material. Eur J Oral Sci, 2005. **113**: p. 225-231.

135. Matheson, S., H. Larjava, and L. Hakkinen, Distinctive localization and function for lumican, fibromodulin and decorin to regulate collagen fibril organization in periodontal tissues. J Periodontal Res, 2005. **40**(4): p. 312-24.

136. Salgado, A.J., O.P. Coutinho, and R.L. Reis, Bone tissue engineering: state of the art and future trends. Macromol Biosci, 2004. **4**(8): p. 743-65.

137. Hatano, H., et al., Extracorporeal irradiated autogenous osteochondral graft: A HISTOLOGICAL STUDY. J Bone Joint Surg Br, 2005. **87**(7): p. 1006-11.

138. Fodor, W.L., Tissue engineering and cell based therapies, from the bench to the clinic: the potential to replace, repair and regenerate. Reprod Biol Endocrinol, 2003. **1**(1): p. 102.

139. Kofron, M.D., X. Li, and C.T. Laurencin, Protein- and gene-based tissue engineering in bone repair. Curr Opin Biotechnol, 2004. **15**(5): p. 399-405.

140. Li, W.J., et al., Multilineage differentiation of human mesenchymal stem cells in a three-dimensional nanofibrous scaffold. Biomaterials, 2005. **26**(25): p. 5158-66.

141. Burg, K.J., S. Porter, and J.F. Kellam, Biomaterial developments for bone tissue engineering. Biomaterials, 2000. **21**(23): p. 2347-59.

142. Hofmann, A., et al., Bioengineered human bone tissue using autogenous osteoblasts cultured on different biomatrices. J Biomed Mater Res A, 2003. **67**(1): p. 191-9.

143. Knabe, C., et al., Evaluation of calcium phosphates and experimental calcium phosphate bone cements using osteogenic cultures. J Biomed Mater Res, 2000. **52**(3): p. 498-508.

144. Vehof, J.W., et al., Bone formation in CaP-coated and noncoated titanium fiber mesh. J Biomed Mater Res A, 2003. **64**(3): p. 417-26.

145. Mistry, A.S. and A.G. Mikos, Tissue engineering strategies for bone regeneration. Adv Biochem Eng Biotechnol, 2005. **94**: p. 1-22.

146. Shin, H., et al., Osteogenic differentiation of rat bone marrow stromal cells cultured on Arg-Gly-Asp modified hydrogels without dexamethasone and beta-glycerol phosphate. Biomaterials, 2005. **26**(17): p. 3645-54.

147. Tanaka, S.M., et al., Osteoblast responses one hour after load-induced fluid flow in a three-dimensional porous matrix. Calcif Tissue Int, 2005. **76**(4): p. 261-71.

148. You, J., et al., Substrate deformation levels associated with routine physical activity are less stimulatory to bone cells relative to loading-induced oscillatory fluid flow. J Biomech Eng, 2000. **122**(4): p. 387-93.

149. van den Dolder, J., et al., Flow perfusion culture of marrow stromal osteoblasts in titanium fiber mesh. J Biomed Mater Res A, 2003. **64**(2): p. 235-41.

150. Cukierman, E., et al., Taking cell-matrix adhesions to the third dimension. Science, 2001. **294**(5547): p. 1708-12.

151. Endres, M., et al., Osteogenic induction of human bone marrow-derived mesenchymal progenitor cells in novel synthetic polymer-hydrogel matrices. Tissue Eng, 2003. **9**(4): p. 689-702.

152. Riminucci, M. and P. Bianco, Building bone tissue: matrices and scaffolds in physiology and biotechnology. Braz J Med Biol Res, 2003. **36**(8): p. 1027-36.

153. Service, R.F., Tissue engineers build new bone. Science, 2000. **289**(5484): p. 1498-500.

154. Medalie, D.A., et al., Differences in dermal analogs influence subsequent pigmentation, epidermal differentiation, basement membrane, and rete ridge formation of transplanted composite skin grafts. Transplantation, 1997. **64**(3): p. 454-465.

155. Holtorf, H.L., et al., Scaffold mesh size affects the osteoblastic differentiation of seeded marrow stromal cells cultured in a flow perfusion bioreactor. J Biomed Mater Res A, 2005. **74**(2): p. 171-80.

156. Park, H., et al., Delivery of TGF-beta1 and chondrocytes via injectable, biodegradable hydrogels for cartilage tissue engineering applications. Biomaterials, 2005. **26**(34): p. 7095-103.

157. Grande-Allen, K.J., et al., Glycosaminoglycan profiles of myxomatous mitral leaflets and chordae parallel the severity of mechanical alterations. J Am Coll Cardiol, 2003. **42**(2): p. 271-7.

158. Vunjak-Novakovic, G., et al., Bioreactor cultivation conditions modulate the composition and mechanical properties of tissue-engineered cartilage. J Orthop Res, 1999. **17**(1): p. 130-8.

159. Lian, J.B. and G.S. Stein, Concepts of osteoblast growth and differentiation: basis for modulation of bone cell development and tissue formation. Crit Rev Oral Biol Med, 1992. **3**(3): p. 269-305.

160. Keller, J.C., et al., *In vitro* attachment of osteoblast-like cells to osteoceramic materials. Dent Mater, 1997. **13**(1): p. 62-8.

161. Dennis, J.E., et al., Osteogenesis in marrow-derived mesenchymal cell porous ceramic composites transplanted subcutaneously: effect of fibronectin and laminin on cell retention and rate of osteogenic expression. Cell Transplant, 1992. **1**(1): p. 23-32.

162. Laffargue, P., et al., Adsorption and release of insulin-like growth factor-I on porous tricalcium phosphate implant. J Biomed Mater Res, 2000. **49**(3): p. 415-21.

163. Yuan, H., et al., A comparison of the osteoinductive potential of two calcium phosphate ceramics implanted intramuscularly in goats. J Mater Sci Mater Med, 2002. **13**(12): p. 1271-5.

164. El-Amin, S.F., et al., Extracellular matrix production by human osteoblasts cultured on biodegradable polymers applicable for tissue engineering. Biomaterials, 2003. **24**(7): p. 1213-21.

165. Mardas, N., et al., Denaturation of demineralized bone matrix significantly reduces bone formation by guided tissue regeneration. Clin Oral Implants Res, 2003. **14**(6): p. 804-11.

166. Wildemann, B., et al., Quantification, localization, and expression of IGF-I and TGF-beta1 during growth factor-stimulated fracture healing. Calcif Tissue Int, 2004. **74**(4): p. 388-97.

167. Dinopoulos, H.T. and P.V. Giannoudis, Safety and efficacy of use of demineralised bone matrix in orthopaedic and trauma surgery. Expert Opin Drug Saf, 2006. **5**(6): p. 847-66.

168. Rosso, F., et al., From cell-ECM interactions to tissue engineering. J Cell Physiol, 2004. **199**(2): p. 174-80.

169. Schreiweis, M.A., et al., A proteomic analysis of adult rat bone reveals the presence of cartilage/chondrocyte markers. J Cell Biochem, 2007.

170. Li, J., Y.P. Zhang, and R.S. Kirsner, Angiogenesis in wound repair: angiogenic growth factors and the extracellular matrix. Microsc Res Tech, 2003. 60(1): p. 107-14.

171. Iwata, H., et al., Demineralized bone matrix and native bone morphogenetic protein in orthopaedic surgery. Clin Orthop Relat Res, 2002(395): p. 99-109.

172. Meijer, G.J., et al., Cell-Based Bone Tissue Engineering. PLoS Med, 2007. 4(2): p. e9.

173. Canalis, E., T. McCarthy, and M. Centrella, Growth factors and the regulation of bone remodeling. J Clin Invest, 1988. 81(2): p. 277-81.

174. Maniatopoulos, C., J. Sodek, and A.H. Melcher, Bone formation in vitro by stromal cells obtained from bone marrow of young adult rats. Cell Tissue Res, 1988. 254(2): p. 317-30.

175. ASTM, W., New standard guide for the assessment of bone inductive materials, ASTM International.

176. Jansen, J.A., et al., Semi-quantitative and qualitative histologic analysis method for the evaluation of implant biocompatibility. J Invest Surg, 1994. 7(2): p. 123-34.

177. Kaminski, E.J., M.W. Shenk, and R.J. Oglesby, Presence of adipose fat as a criterion of implant compatibility. J Biomed Mater Res, 1977. 11(6): p. 871-81.

178. Habibovic, P., et al., Osteoinduction by biomaterials--physicochemical and structural influences. J Biomed Mater Res A, 2006. 77(4): p. 747-62.

179. Pietrzak, W.S., The hydration characteristics of demineralized and nondemineralized allograft bone: Scientific perspectives on graft function. J Craniofac Surg, 2006. 17(1): p. 120-30.

180. Sampath, T.K. and A.H. Reddi, Distribution of bone inductive proteins in mineralized and demineralized extracellular matrix. Biochem Biophys Res Commun, 1984. 119(3): p. 949-54.

181. Kream, B.E. and B.P. Lukert, Clinical and basic aspects of glucocorticoid action in bone, ed. J. Bilezikian, L. Raisz, and G. Rodan. Vol. 1. 2002.

182. Tiedeman, J.J., et al., Treatment of nonunion by percutaneous injection of bone marrow and demineralized bone matrix. An experimental study in dogs. Clin Orthop Relat Res, 1991(268): p. 294-302.

183. Shih, H.N., et al., Restoration of bone defect and enhancement of bone ingrowth using partially demineralized bone matrix and marrow stromal cells. J Orthop Res, 2005. **23**(6): p. 1293-9.

184. Tiedeman, J.J., et al., The role of a composite, demineralized bone matrix and bone marrow in the treatment of osseous defects. Orthopedics, 1995. **18**(12): p. 1153-8.

185. Subbiah, T., et al., Electrospinning of nanofibers. J. Appl. Polym. Sci., 2005. **96**(2): p. 557-569.

186. Huang, Z.M., et al., A review on polymer nanofibers by electrospinning and their applications in nanocomposites. Composites Science and Technology, 2003. **63**(15): p. 2223-2253.

187. Frenot, A. and I.S. Chronakis, Polymer nanofibers assembled by electrospinning. Current Opinion in Colloid & Interface Science, 2003. **8**(1): p. 64-75.

188. Reneker, D.H. and I. Chun, Nanometre diameter fibres of polymer, produced by electrospinning. Nanotechnology, 1996. **7**(3): p. 216-223.

189. Ki, C.S., et al., Characterization of gelatin nanofiber prepared from gelatin-formic acid solution. Polymer, 2005. **46**(14): p. 5094-5102.

190. Geng, X.Y., O.H. Kwon, and J.H. Jang, Electrospinning of chitosan dissolved in concentrated acetic acid solution. Biomaterials, 2005. **26**(27): p. 5427-5432.

191. Jiang, H.L., et al., Optimization and characterization of dextran membranes prepared by electrospinning. Biomacromolecules, 2004. **5**(2): p. 326-333.

192. Huang, L., et al., Engineered collagen-PEO nanofibers and fabrics. J Biomater Sci Polym Ed 2001. **12**(9): p. 979-993.

193. Matthews, J.A., et al., Electrospinning of collagen nanofibers. Biomacromolecules, 2002. **3**(2): p. 232-238.

194. Shin, Y.M., et al., Electrospinning: A whipping fluid jet generates submicron polymer fibers. Appl Phys Lett, 2001. **78**(8): p. 1149-1151.

195. Shin, Y.M., et al., Experimental characterization of electrospinning: the electrically forced jet and instabilities. Polymer, 2001. **42**(25): p. 9955-9967.

196. Hohman, M.M., et al., Electrospinning and electrically forced jets. I. Stability theory. Phys Fluids, 2001. **13**(8): p. 2201-2220.

197. Hohman, M.M., et al., Electrospinning and electrically forced jets. II. Applications. Phys Fluids, 2001. **13**(8): p. 2221-2236.

198. Zong, X.H., et al., Structure and process relationship of electrospun bioabsorbable nanofiber membranes. Polymer, 2002. **43**(16): p. 4403-4412.

199. Kim, H.S., et al., Morphological characterization of electrospun nano-fibrous membranes of biodegradable poly(L-lactide) and poly(lactide-co-glycolide). Macromol Symp, 2005. **224**: p. 145-154.

200. Deitzel, J.M., et al., The effect of processing variables on the morphology of electrospun nanofibers and textiles. Polymer, 2001. **42**(1): p. 261-272.

201. Son, W.K., et al., The effects of solution properties and polyelectrolyte on electrospinning of ultrafine poly(ethylene oxide) fibers. Polymer, 2004. **45**(9): p. 2959-2966.

202. Fong, H., I. Chun, and D.H. Reneker, Beaded nanofibers formed during electrospinning. Polymer, 1999. **40**(16): p. 4585-4592.

203. Koski, A., K. Yim, and S. Shivkumar, Effect of molecular weight on fibrous PVA produced by electrospinning. Mater Lett, 2004. **58**(3-4): p. 493-497.

204. Zhang, C.X., et al., Study on morphology of electrospun poly(vinyl alcohol) mats. Eur Polym J, 2005. **41**(3): p. 423-432.

205. Lee, J.S., et al., Role of molecular weight of atactic poly(vinyl alcohol) (PVA) in the structure and properties of PVA nanofabric prepared by electrospinning. J Appl Polym Sci, 2004. **93**(4): p. 1638-1646.

206. Ding, B., et al., Preparation and characterization of a nanoscale poly(vinyl alcohol) fiber aggregate produced by an electrospinning method. J Polym Sci B Polym Phys, 2002. **40**(13): p. 1261-1268.

207. Gupta, P., et al., Electrospinning of linear homopolymers of poly(methyl methacrylate): exploring relationships between fiber formation, viscosity, molecular weight and concentration in a good solvent. Polymer, 2005. **46**(13): p. 4799-4810.

208. Jarusuwannapoom, T., et al., Effect of solvents on electro-spinnability of polystyrene solutions and morphological appearance of resulting electrospun polystyrene fibers. Eur Polym J, 2005. **41**(3): p. 409-421.

209. Jun, Z., et al., Poly-L-lactide nanofibers by electrospinning - Influence of solution viscosity and electrical conductivity on fiber diameter and fiber morphology. E-Polymers, 2003: p. -.

210. Demir, M.M., et al., Electrospinning of polyurethane fibers. Polymer, 2002. **43**(11): p. 3303-3309.

211. Duan, B., et al., Electrospinning of chitosan solutions in acetic acid with poly(ethylene oxide). J Biomater Sci Polym Ed, 2004. **15**(6): p. 797-811.

212. McKee, M.G., et al., Correlations of solution rheology with electrospun fiber formation of linear and branched polyesters. Macromolecules, 2004. **37**(5): p. 1760-1767.

213. Liu, H.Q. and Y.L. Hsieh, Ultrafine fibrous cellulose membranes from electrospinning of cellulose acetate. J Polym Sci B Polym Phys, 2002. **40**(18): p. 2119-2129.

214. Ryu, Y.J., et al., Transport properties of electrospun nylon 6 nonwoven mats. Eur Polym J, 2003. **39**(9): p. 1883-1889.

215. Zuo, W.W., et al., Experimental study on relationship between jet instability and formation of beaded fibers during electrospinning. Polym Eng Sci, 2005. **45**(5): p. 704-709.

216. Mit-uppatham, C., M. Nithitanakul, and P. Supaphol, Ultrafine electrospun polyamide-6 fibers: Effect of solution conditions on morphology and average fiber diameter. Macromol Chem Phys, 2004. **205**(17): p. 2327-2338.

217. Lin, T., et al., The charge effect of cationic surfactants on the elimination of fibre beads in the electrospinning of polystyrene. Nanotechnology, 2004. **15**(9): p. 1375-1381.

218. Chen, H. and Y.L. Hsieh, Ultrafine hydrogel fibers with dual temperature- and pH-responsive swelling behaviors. J Polym Sci A: Polym Chem, 2004. **42**(24): p. 6331-6339.

219. Liu, J. and S. Kumar, Microscopic polymer cups by electrospinning. Polymer, 2005. **46**(10): p. 3211-3214.

220. Wannatong, L., A. Sirivat, and P. Supaphol, Effects of solvents on electrospun polymeric fibers: preliminary study on polystyrene. Polym Int, 2004. **53**(11): p. 1851-1859.

221. Yuan, X.Y., et al., Morphology of ultrafine polysulfone fibers prepared by electrospinning. Polym Int, 2004. **53**(11): p. 1704-1710.

222. Buchko, C.J., et al., Processing and microstructural characterization of porous biocompatible protein polymer thin films. Polymer, 1999. **40**(26): p. 7397-7407.

223. Zhao, Z.Z., et al., Preparation and properties of electrospun poly(vinylidene fluoride) membranes. J Appl Polym Sci, 2005. **97**(2): p. 466-474.

224. Li, D., et al., Nanofibers of conjugated polymers prepared by electrospinning with a two-capillary spinneret. Adv Mater, 2004. **16**(22): p. 2062.

225. Theron, S.A., et al., Multiple jets in electrospinning: experiment and modeling. Polymer, 2005. **46**(9): p. 2889-2899.

226. Ding, B., et al., Fabrication of blend biodegradable nanofibrous nonwoven mats via multi-jet electrospinning. Polymer, 2004. **45**(6): p. 1895-1902.

227. Kidoaki, S., I.K. Kwon, and T. Matsuda, Mesoscopic spatial designs of nano- and microfiber meshes for tissue-engineering matrix and scaffold based on newly devised multilayering and mixing electrospinning techniques. Biomaterials, 2005. **26**(1): p. 37-46.

228. Kenawy, E.R., et al., Electrospinning of poly(ethylene-co-vinyl alcohol) fibers. Biomaterials, 2003. **24**(6): p. 907-913.

229. Fridrikh, S.V., et al., Controlling the fiber diameter during electrospinning. Phys Rev Lett, 2003. **90**(14): p. -.

230. Dalton, P.D., D. Klee, and M. Moller, Electrospinning with dual collection rings. Polymer, 2005. **46**(3): p. 611-614.

231. Deitzel, J.M., et al., Controlled deposition of electrospun poly(ethylene oxide) fibers. Polymer, 2001. **42**(19): p. 8163-8170.

232. Chew, S.Y., et al., Sustained release of proteins from electrospun biodegradable fibers. Biomacromolecules, 2005. **6**(4): p. 2017-2024.

233. Katta, P., et al., Continuous electrospinning of aligned polymer nanofibers onto a wire drum collector. Nano Lett, 2004. **4**(11): p. 2215-2218.

234. Sundaray, B., et al., Electrospinning of continuous aligned polymer fibers. Appl Phys Lett, 2004. **84**(7): p. 1222-1224.

235. Theron, A., E. Zussman, and A.L. Yarin, Electrostatic field-assisted alignment of electrospun nanofibres. Nanotechnology, 2001. **12**(3): p. 384-390.

236. Casper, C.L., et al., Controlling surface morphology of electrospun polystyrene fibers: Effect of humidity and molecular weight in the electrospinning process. Macromolecules, 2004. **37**(2): p. 573-578.

237. Langer, R. and J.P. Vacanti, Tissue engineering. Science, 1993. **260**(5110): p. 920-6.

238. Xu, C., et al., Electrospun nanofiber fabrication as synthetic extracellular matrix and its potential for vascular tissue engineering. Tissue Eng, 2004. **10**(7-8): p. 1160-8.

239. Behonick, D.J. and Z. Werb, A bit of give and take: the relationship between the extracellular matrix and the developing chondrocyte. Mech Dev, 2003. **120**(11): p. 1327-36.

240. Franceschi, R.T. and B.S. Iyer, Relationship between collagen synthesis and expression of the osteoblast phenotype in MC3T3-E1 cells. J Bone Miner Res, 1992. **7**(2): p. 235-46.

241. Lan, C.W., F.F. Wang, and Y.J. Wang, Osteogenic enrichment of bone-marrow stromal cells with the use of flow chamber and type I collagen-coated surface. J Biomed Mater Res A, 2003. **66**(1): p. 38-46.

242. Li, W.J., et al., Electrospun nanofibrous structure: a novel scaffold for tissue engineering. J Biomed Mater Res, 2002. **60**(4): p. 613-21.

243. Smith, L.A. and P.X. Ma, Nano-fibrous scaffolds for tissue engineering. Colloids Surf B Biointerfaces, 2004. **39**(3): p. 125-31.

244. Hutmacher, D.W., Scaffolds in tissue engineering bone and cartilage. Biomaterials, 2000. **21**(24): p. 2529-43.

245. Flemming, R.G., et al., Effects of synthetic micro- and nano-structured surfaces on cell behavior. Biomaterials, 1999. **20**(6): p. 573-88.

246. Price, R.L., et al., Osteoblast function on nanophase alumina materials: Influence of chemistry, phase, and topography. J Biomed Mater Res A, 2003. **67**(4): p. 1284-93.

247. Ma, Z.W., et al., Potential of nanofiber matrix as tissue-engineering scaffolds. Tissue Engineering, 2005. **11**(1-2): p. 101-109.

248. Teixeira, A.I., et al., Epithelial contact guidance on well-defined micro- and nanostructured substrates. J Cell Sci, 2003. **116**(Pt 10): p. 1881-92.

249. Yang, F., et al., Fabrication of nano-structured porous PLLA scaffold intended for nerve tissue engineering. Biomaterials, 2004. **25**(10): p. 1891-900.

250. Elias, K.L., R.L. Price, and T.J. Webster, Enhanced functions of osteoblasts on nanometer diameter carbon fibers. Biomaterials, 2002. **23**(15): p. 3279-87.

251. Li, W.J., et al., Biological response of chondrocytes cultured in three-dimensional nanofibrous poly(epsilon-caprolactone) scaffolds. J Biomed Mater Res A, 2003. **67**(4): p. 1105-14.

252. Kwon, I.K., S. Kidoaki, and T. Matsuda, Electrospun nano- to microfiber fabrics made of biodegradable copolyesters: structural characteristics, mechanical properties and cell adhesion potential. Biomaterials, 2005. **26**(18): p. 3929-39.

253. Schindler, M., et al., A synthetic nanofibrillar matrix promotes *in vivo*-like organization and morphogenesis for cells in culture. Biomaterials, 2005. **26**(28): p. 5624-31.

254. Tuan, R.S., G. Boland, and R. Tuli, Adult mesenchymal stem cells and cell-based tissue engineering. Arthritis Res Ther, 2003. **5**(1): p. 32-45.

255. Li, W.J., et al., A three-dimensional nanofibrous scaffold for cartilage tissue engineering using human mesenchymal stem cells. Biomaterials, 2005. **26**(6): p. 599-609.

256. Yoshimoto, H., et al., A biodegradable nanofiber scaffold by electrospinning and its potential for bone tissue engineering. Biomaterials, 2003. **24**(12): p. 2077-2082.

257. Shin, M., H. Yoshimoto, and J.P. Vacanti, *In vivo* bone tissue engineering using mesenchymal stem cells on a novel electrospun nanofibrous scaffold. Tissue Eng, 2004. **10**(1-2): p. 33-41.

258. Xu, C.Y., et al., Aligned biodegradable nanofibrous structure: a potential scaffold for blood vessel engineering. Biomaterials, 2004. **25**(5): p. 877-86.

259. Zong, X., et al., Electrospun fine-textured scaffolds for heart tissue constructs. Biomaterials, 2005. **26**(26): p. 5330-8.

260. Shin, M., et al., Contractile cardiac grafts using a novel nanofibrous mesh. Biomaterials, 2004. **25**(17): p. 3717-23.

261. Almany, L. and D. Seliktar, Biosynthetic hydrogel scaffolds made from fibrinogen and polyethylene glycol for 3D cell cultures. Biomaterials, 2005. **26**(15): p. 2467-77.

262. Wayne, J.S., et al., *In vivo* response of polylactic Acid-alginate scaffolds and bone marrow-derived cells for cartilage tissue engineering. Tissue Eng, 2005. **11**(5-6): p. 953-63.

263. Yoo, H.S., et al., Hyaluronic acid modified biodegradable scaffolds for cartilage tissue engineering. Biomaterials, 2005. **26**(14): p. 1925-33.

264. Pavlov, M.P., et al., Fibers and 3D mesh scaffolds from biodegradable starch-based blends: production and characterization. Macromol Biosci, 2004. **4**(8): p. 776-84.

265. Zhang, Y., et al., Electrospinning of gelatin fibers and gelatin/PCL composite fibrous scaffolds. J Biomed Mater Res B Appl Biomater, 2005. **72**(1): p. 156-65.

266. Boland, E.D., et al., Electrospinning collagen and elastin: preliminary vascular tissue engineering. Front Biosci, 2004. **9**: p. 1422-32.

267. Venugopal, J. and S. Ramakrishna, Biocompatible nanofiber matrices for the engineering of a dermal substitute for skin regeneration. Tissue Eng, 2005. **11**(5-6): p. 847-54.

268. Berglund, J.D., R.M. Nerem, and A. Sambanis, Incorporation of intact elastin scaffolds in tissue-engineered collagen-based vascular grafts. Tissue Eng, 2004. **10**(9-10): p. 1526-35.

269. Huang, L., et al., Generation of synthetic elastin-mimetic small diameter fibers and fiber networks. Macromolecules, 2000. **33**(8): p. 2989-2997.

270. Wnek, G.E., et al., Electrospinning of nanofiber fibrinogen structures. Nano Letters, 2003. **3**(2): p. 213-216.

271. Katti, D.S., et al., Bioresorbable nanofiber-based systems for wound healing and drug delivery: optimization of fabrication parameters. J Biomed Mater Res, 2004. **70B**(2): p. 286-96.

272. Peretti, G.M., et al., A biomechanical analysis of an engineered cell-scaffold implant for cartilage repair. Ann Plast Surg, 2001. **46**(5): p. 533-7.

273. Fang, X. and D.H. Reneker, DNA fibers by electrospinning. Journal of Macromolecular Science-Physics, 1997. **B36**(2): p. 169-173.

274. Jin, H.J., et al., Electrospinning Bombyx mori silk with poly(ethylene oxide). Biomacromolecules, 2002. **3**(6): p. 1233-9.

275. Jin, H.J., et al., Human bone marrow stromal cell responses on electrospun silk fibroin mats. Biomaterials, 2004. **25**(6): p. 1039-47.

276. Boland, E.D., et al., Utilizing acid pretreatment and electrospinning to improve biocompatibility of poly(glycolic acid) for tissue engineering. J Biomed Mater Res B Appl Biomater, 2004. **71**(1): p. 144-52.

277. Bhattarai, S.R., et al., Novel biodegradable electrospun membrane: scaffold for tissue engineering. Biomaterials, 2004. **25**(13): p. 2595-602.

278. Dror, Y., et al., Carbon nanotubes embedded in oriented polymer nanofibers by electrospinning. Langmuir, 2003. **19**(17): p. 7012-7020.

279. Ge, J.J., et al., Assembly of well-aligned multiwalled carbon nanotubes in confined polyacrylonitrile environments: Electrospun composite nanofiber sheets. Journal of the American Chemical Society, 2004. **126**(48): p. 15754-15761.

280. Hou, H.Q., et al., Electrospun polyacrylonitrile nanofibers containing a high concentration of well-aligned multiwall carbon nanotubes. Chemistry of Materials, 2005. **17**(5): p. 967-973.

281. Bentz, H., J.A. Schroeder, and T.D. Estridge, Improved local delivery of TGF-beta2 by binding to injectable fibrillar collagen via difunctional polyethylene glycol. J Biomed Mater Res, 1998. **39**(4): p. 539-48.

282. Chua, K.N., et al., Stable immobilization of rat hepatocyte spheroids on galactosylated nanofiber scaffold. Biomaterials, 2005. **26**(15): p. 2537-47.

283. Casper, C.L., et al., Functionalizing electrospun fibers with biologically relevant macromolecules. Biomacromolecules, 2005. **6**(4): p. 1998-2007.

284. Gombotz, W.R. and D.K. Pettit, Biodegradable polymers for protein and peptide drug delivery. Bioconjug Chem, 1995. **6**(4): p. 332-51.

285. Verreck, G., et al., Incorporation of drugs in an amorphous state into electrospun nanofibers composed of a water-insoluble, nonbiodegradable polymer. Journal of Controlled Release, 2003. **92**(3): p. 349-60.

286. Kenawy, E.R., et al., Release of tetracycline hydrochloride from electrospun poly(ethylene-co-vinylacetate), poly(lactic acid), and a blend. Journal of Controlled Release, 2002. **81**(1-2): p. 57-64.

287. Thanou, M. and R. Duncan, Polymer-protein and polymer-drug conjugates in cancer therapy. Curr Opin Investig Drugs, 2003. **4**(6): p. 701-9.

288. Jiang, H., et al., Preparation and characterization of ibuprofen-loaded poly(lactide-co-glycolide)/poly(ethylene glycol)-g-chitosan electrospun membranes. J Biomater Sci Polym Ed, 2004. **15**(3): p. 279-96.

289. Luu, Y.K., et al., Development of a nanostructured DNA delivery scaffold via electrospinning of PLGA and PLA-PEG block copolymers. Journal of Controlled Release, 2003. **89**(2): p. 341-353.

290. Luu, Y.K., et al., Development of a nanostructured DNA delivery scaffold via electrospinning of PLGA and PLA-PEG block copolymers. J Control Release, 2003. **89**(2): p. 341-53.

291. Pham, Q.P., U. Sharma, and A.G. Mikos, Electrospinning of polymeric nanofibers for tissue engineering applications: a review. Tissue Eng, 2006. **12**(5): p. 1197-211.

292. Eichhorn, S.J. and W.W. Sampson, Statistical geometry of pores and statistics of porous nanofibrous assemblies. Journal of the Royal Society Interface, 2005. **2**(4): p. 309-318.

293. Goldstein, A.S., et al., Effect of osteoblastic culture conditions on the structure of poly(DL-lactic-co-glycolic acid) foam scaffolds. Tissue Eng, 1999. **5**(5): p. 421-34.

294. Karageorgiou, V. and D. Kaplan, Porosity of 3D biomaterial scaffolds and osteogenesis. Biomaterials, 2005. **26**(27): p. 5474-91.

295. Yang, S.F., et al., The design of scaffolds for use in tissue engineering. Part 1. Traditional factors. Tissue Engineering, 2001. **7**(6): p. 679-689.

296. Woodfield, T.B., et al., Polymer scaffolds fabricated with pore-size gradients as a model for studying the zonal organization within tissue-engineered cartilage constructs. Tissue Eng, 2005. **11**(9-10): p. 1297-311.

297. Schwarz, K. and M. Epple, Hierarchically structured polyglycolide - a biomaterial mimicking natural bone. Macromolecular Rapid Communications, 1998. **19**(12): p. 613-617.

298. Min, B.M., et al., Electrospinning of silk fibroin nanofibers and its effect on the adhesion and spreading of normal human keratinocytes and fibroblasts *in vitro*. Biomaterials, 2004. **25**(7-8): p. 1289-97.

299. Badami, A.S., et al., Effect of fiber diameter on spreading, proliferation, and differentiation of osteoblastic cells on electrospun poly(lactic acid) substrates. Biomaterials, 2005.

300. Matthews, J.A., et al., Electrospinning of collagen nanofibers. Biomacromolecules, 2002. **3**(2): p. 232-8.

301. Tuzlakoglu, K., et al., Nano- and micro-fiber combined scaffolds: a new architecture for bone tissue engineering. J Mater Sci Mater Med, 2005. **16**(12): p. 1099-104.

302. Takahashi, Y. and Y. Tabata, Effect of the fiber diameter and porosity of non-woven PET fabrics on the osteogenic differentiation of mesenchymal stem cells. J Biomater Sci Polym Ed, 2004. **15**(1): p. 41-57.

303. Grant, P.V., et al., Physical Characterization of a Polycaprolactone Tissue Scaffold. 2005, National Physical Laboratory.

304. Hu, Y., et al., Fabrication of poly(alpha-hydroxy acid) foam scaffolds using multiple solvent systems. J Biomed Mater Res, 2002. **59**(3): p. 563-72.

305. Holy, C.E. and R. Yakubovich, Processing cell-seeded polyester scaffolds for histology. J Biomed Mater Res, 2000. **50**(2): p. 276-9.

306. Jaeger, R., et al., Electrospinning of ultra-thin polymer fibers. Macromol Symp. 1998. **127**: p. 141.

307. Mikos, A.G., et al., Preparation and Characterization of Poly(L-Lactic Acid) Foams. Polymer, 1994. **35**(5): p. 1068-1077.

308. Ho, S.T. and D.W. Hutmacher, A comparison of micro CT with other techniques used in the characterization of scaffolds. Biomaterials, 2006. **27**(8): p. 1362-1376.

309. Sampson, W.W., A multiplanar model for the pore radius distribution in isotropic near-planar stochastic fibre networks. Journal of Materials Science, 2003. **38**(8): p. 1617-1622.

310. Lee, Y.H., et al., Electrospun dual-porosity structure and biodegradation morphology of Montmorillonite reinforced PLLA nanocomposite scaffolds. Biomaterials, 2005. **26**(16): p. 3165-72.

311. Stankus, J.J., et al., Microintegrating smooth muscle cells into a biodegradable, elastomeric fiber matrix. Biomaterials, 2005.